Doctoral Dissertations   Graduate School

8-2021

Thermochemical and Continuum Modeling to Understand the Chemical Composition of PWR Fuel CRUD

Jason T. Rizk

jrizk@vols.utk.edu

Follow this and additional works at: https://trace.tennessee.edu/utk_graddiss

Part of the Nuclear Engineering Commons, and the Thermodynamics Commons

To the Graduate Council:

I am submitting herewith a dissertation written by Jason T. Rizk entitled "Thermochemical and Continuum Modeling to Understand the Chemical Composition of PWR Fuel CRUD." I have examined the final electronic copy of this dissertation for form and content and recommend that it be accepted in partial fulfillment of the requirements for the degree of Doctor of Philosophy, with a major in Nuclear Engineering.

Brian David Wirth, Major Professor

We have read this dissertation and recommend its acceptance:

Brian David Wirth, Ivan Maldonado, William John Weber, Steven John Zinkle, Anders David Andersson, Benjamin Collins

Accepted for the Council:

Dixie L. Thompson

Vice Provost and Dean of the Graduate School

(Original signatures are on file with official student records.)

Thermochemical and Continuum Modeling to Understand the Chemical Composition of PWR Fuel CRUD

A Dissertation Presented for the

Doctor of Philosophy

Degree

The University of Tennessee, Knoxville

Jason T. Rizk

August 2021

ACKNOWLEDGEMENTS

ABSTRACT

Computational modeling of Chalk River Undesirable Deposits (CRUD) allows for the prediction of associated phenomena that impact nuclear power plant performance, reliability, and safety. It also provides insight into the physical mechanisms by which CRUD forms and affects plant performance. A major concern in pressurized water reactors (PWRs) is Axial Offset Anomaly (AOA) which is caused by CRUD's proficiency at trapping boron within the reactor core. The ability to predict AOA and other phenomena requires a detailed explanation of the chemical composition of CRUD. By pairing computational models that can simulate the structure and species trapping with detailed thermochemical models, the compounds that makeup CRUD are determined. Among these thermodynamically predicted compounds is Ni_2FeBO_5, a mineral named bonaccordite, the formation of which provides a boron retention mechanism. Accordingly, bonaccordite has been found in CRUD samples from fuel linked to very extreme AOA. In this dissertation, thermochemical models are detailed for PWR primary loop chemistry up to the saturation temperature and are implemented using CALPHAD modeling. Likely solid precipitation reactions are identified, and those reactions are incorporated into the multiphysics continuum modeling code MAMBA. An assessment of the kinetic rates of the reactions are determined by Bayesian calibration of the MAMBA model using observational data from CRUD samples. The modeling is able to demonstrate the composition of CRUD scrapes obtained from plant data. This model contributes to the understanding of CRUD formation and composition and allows for the prediction of phenomena such as AOA.

Keywords: CRUD, boric acid, CALPHAD, bonaccordite, Bayesian calibration

TABLE OF CONTENTS

LIST OF TABLES

LIST OF FIGURES

CHAPTER 1. INTRODUCTION

Chalk River Undesirable Deposits (CRUD) occur in commercial reactors as a result of corrosion products in the primary-loop coolant collecting on the outer surface of the fuel rods. These deposits can greatly limit the performance, reliability, and safety of reactor operation. In pressurized-water-reactors (PWRs), subcooled nucleate boiling enhances reactor performance by facilitating the heat transfer from the fuel rods to the primary coolant. However, subcooled nucleate boiling contributes to CRUD formation, which impedes heat transfer as the deposit becomes thicker. Formation is initiated by the precipitation of nanoscale particulates [1] in the region of greatest temperature where subcooled nucleate boiling prevails, which is along the upper portion of the core. CRUD formation is also facilitated by the retrograde solubility of several of the compounds involved [2, 3]. CRUD is often porous and can quickly become thick enough to sustain internal boiling, causing any aqueous species to become supersaturated within the deposit and eventually precipitate. This supersaturation and precipitation lead to changes in the local chemistry and microstructure of the CRUD for which modeling efforts should account.

The major elements present in PWR primary coolant that find their way into CRUD are Ni and Fe from steam generator tubes and other piping surfaces, B from the boric acid (H_3BO_3) added to the coolant as a reactivity control mechanism, Li from the LiOH added to adjust the pH. Zr from the oxidation of the metal fuel cladding also contributes to CRUD. The Ni and Fe exist in the coolant as either solid nanoscale particulates [4, 5], particularly nickel metal and nickel ferrite ($NiFe_2O_4$), or as aqueous ionic species.

MAMBA (MPO Advanced Model for Boron Analysis) was developed as part of the CASL (Consortium for Advanced Simulation of Light-water reactors) suite of software aimed at modeling phenomena such as Axial Offset Anomaly (AOA) [6, 7]. MAMBA predicts CRUD thickness, internal local chemistry including boron concentration, porosity, internal boiling, and heat flux. This dissertation makes advancements in the solid thermodynamic and chemistry models in MAMBA to obtain a better understanding, and hence better ability to predict, the fundamental causes of AOA.

1.1 Background/Existing Literature

1.1.1 Basics of CRUD Formation and Structure

Corrosion products that originate along the surfaces of the primary loop such as the nickel-chromium-alloy steam generator tubes, pumps, piping and other metal surfaces enter the coolant as either nanoscale particulates or dissolved aqueous species [8-11]. In a pressurized water reactor (PWR), these corrosion products are preferentially deposited in the upper spans of the reactor core due the presence of sub-cooled nucleate boiling in the highest-temperature region of the primary loop. The deposits are often quite porous, which causes coolant to become trapped within them. This trapped coolant rises in temperature and eventually boils, exiting the CRUD as vapor through the boiling chimneys that form in the deposit. While the trapped water escapes as steam, the trapped soluble species supersaturate within the CRUD and eventually precipitate, filling the pores with solid phases.

The dominant microstructural feature of CRUD is the existence of the boiling chimneys [12]. The size, shape, and number density of these chimneys all affect how coolant flows through and exits CRUD, affecting the local temperature and chemistry. Figure 1.1 shows a scanning electron microscopy (SEM) image showing chimneys that are about 10 μm in diameter.

1.1.2 Problems Associated with CRUD

There are several fuel performance concerns associated with CRUD formation. If CRUD is thin and porous, then it enhances sub-cooled nucleate boiling that increases the efficiency of heat transfer from the fuel to the coolant, but if CRUD is thick and has low porosity, then it inhibits heat transfer and leads to elevated fuel cladding temperatures [13]. The combination of these elevated temperatures, the concentration of corrosive species trapped within the CRUD, and the presence of steam lead to heightened zirconium oxidation kinetics known as CRUD-induced localized corrosion (CILC). CILC leads to a significant consumption of the cladding, which can then become penetrated leading to a fuel rod leak.

Another concern is the increase in the primary loop radiation field. Neutron activation of the Co, Ni, Fe, and Cr trapped in the CRUD (e.g. $^{58}Ni(n,p)^{58}Co$, $^{59}Co(n,\gamma)^{60}Co$) cause it to be radioactive [14]. The CRUD can then release from the fuel rods into the coolant, travel, and deposit throughout the entire primary loop.
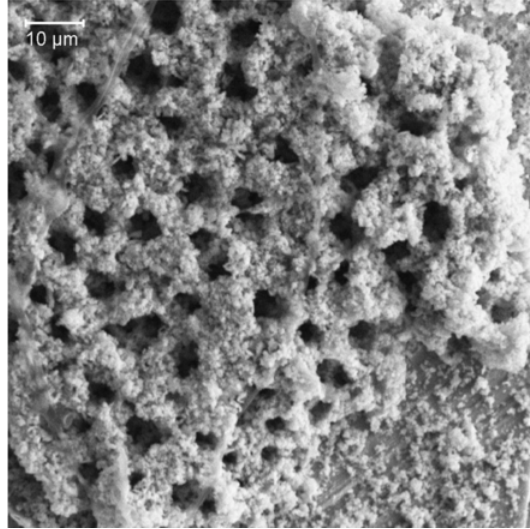
Figure 1.1: SEM image of a CRUD flake from Vogtle-2 Cycle 8 showing characteristic boiling chimneys (Reproduced from [12])

The most significant fuel performance concern associated with CRUD is Axial Offset Anomaly (AOA), also known as CRUD-Induced Power Shifts (CIPS) [14]. Among the trapped aqueous species are boric acid $B(OH)_3$ and lithium hydroxide LiOH, which are added to control reactivity and moderate coolant pH, respectively. The boric acid and boron-containing solid precipitates that accumulate in the CRUD are strong neutron absorbers and depress both the local neutron flux and the local power output in the upper spans of the core. To maintain the same total power, the bottom half of the core must increase its power output, which can often lead to axial power oscillations that result from non-steady state fission products that are strong neutron absorbers (e.g. Xe-135), and in many cases the reactor power must be downrated [14]. The axial offset of a reactor is defined as the difference between the power in the top and in the bottom halves of the core divided by the total core power, given in percent. Accurate modeling predictions of the axial offset can help prevent unexpected power plant downrating and unplanned outages that would result in economic loss.

1.1.3 Deposition Mechanisms

CRUD deposits by two mechanisms that correspond with the two types of species within PWR coolant. The first type of species exists as solid nanoscale particulates which are either octahedral-shaped nickel ferrite ($NiFe_2O_4$) or rod-shaped nickel metal (Ni) [5]. The nickel ferrite particulates form elsewhere in the primary circuit, such along the surfaces of the steam generator tubes. Erosion of the oxide layers or metal surfaces of the steam generators release these particles which end up depositing in the core. While larger particulates are removed by system filters installed for the plant's primary coolant, a high-duty core efficiently traps the smaller particulates by means of subcooled nucleate boiling. These particulates exist in low concentrations (~ppb); their deposition, however, is the primary mechanism for CRUD growth [1, 14]. These particulates attach at the surface of the fuel rod or CRUD layer, growing the deposit thickness and creating a porous skeleton in which coolant is trapped.

The second type of species within PWR coolant exists in the aqueous phase. Boric acid is added to PWR coolant in order to control reactivity, and LiOH is added to balance the pH. The concentrations of these additives are high at the beginning of the reactor cycle, ~1200 ppm and ~2 ppm respectively, and decrease as burnup increases to eventually equal zero by the end of the

cycle. Other important aqueous species are the Ni and Fe ions dissolved in the coolant in ~ppb concentrations due to the corrosion of the primary loop surfaces. Minor elements due to additives or corrosion are Zn, Cr, Mn, and C. When coolant containing these aqueous species becomes trapped within the CRUD and then boils, the aqueous species become saturated within the CRUD pores. These species precipitate into solids such as $Li_2B_4O_7$ and $NiFe_2O_4$, which fill in the CRUD porosity. If the precipitates contain B, then they can cause AOA [14].

1.1.4 CRUD Sampling and Characterization

CRUD samples are obtained from used fuel while it is being moved during a refueling outage or is in spent fuel storage pools. CRUD can be obtained by ultrasonic cleaning, scrubbing with filter paper, or most commonly by scraping [5, 15, 16]. CRUD obtained by scrubbing with filter paper is defined as "soft," and CRUD tenaciously attached to the fuel rod that requires scraping to obtain is defined as "hard" [15]. CRUD is scraped uniformly from the bottom to the top of a spent fuel rod by a tool shaped to remove the deposit from over 120 degrees of the circumference of the rod [16]. These scrapes are typically 30 cm long along the axis of the rod. When the scraping is performed, much of the CRUD becomes dislodged, forming a suspension in the spent fuel pool water, which is then vacuumed and collected by a filter. The resulting filter "cake" is washed with deionized water before characterization to remove any soluble species still trapped within the CRUD [17]. During the scraping process, whole "flakes" sometimes break off of the rod surface, maintaining the rod's curvature and preserving their thickness.

CRUD consists of many different crystalline particles in a complex arrangement. In thick CRUD that leads to AOA, the deposit tends to have a layered structure in the radial direction of the fuel rod [18]. Near the cladding, there tends to be more octahedrally shaped particles, and near the coolant there tends to be more needle-shaped particles [15], although the inner layer may also contain needle-shaped particles [17].

CRUD consists mostly of Ni, Fe, and Cr oxides, which are the principal elements in steel and Inconel alloys used in the primary loop. CRUD traps significant amounts of B, Li, and Zn, which are coolant additives in PWRs. Zr is always incorporated in CRUD, and results from corrosion of the cladding. Other elements that may be present include Mn, Co, Sn, C, and Si [5, 15, 18].

Micrographs of typical CRUD samples taken from a Korean plant are shown in Figure 1.2, as reproduced from [15]. The octahedral crystal particles have a Fe/Ni ratio of ~2, which indicates they are nickel ferrite ($NiFe_2O_4$). Due to the large size of these particles, it can be deduced that they grew to that size within the CRUD rather than being formed elsewhere in the primary loop and deposited on the fuel rods. Zr was observed to replace the Ni cations in $NiFe_2O_4$. The needle-like particles are rich in Ni and are more concentrated in the outer layer of the CRUD, suggesting the deposition of Ni at the surface. ZrO_2 fragments that are broken off the oxide layer of the cladding are contained in the samples. Round Si-rich particles are found as well. Si is an impurity that likely is introduced from chemical additives, the spent fuel pool storage racks, and the filter materials. Hard CRUD contains a greater Fe/Ni ratio than soft CRUD. In addition, hard CRUD typically contains more Zn, particularly in the inner cladding-side layer [15, 18].

1.1.5 WALT Loop Experiment

The Westinghouse Advanced Loop Tester (WALT) was an experiment to simulate CRUD and measure the effective thermal conductivity under various conditions [13]. This test loop simulates PWR coolant conditions with the addition of large concentrations of CRUD-forming soluble and particulate species. This loop has demonstrated the rapid growth of CRUD-like deposits on a heated rod, and the rod surface temperature was measured over a variety of CRUD thicknesses and heat flux values. The simulated CRUD consisted mostly of $NiFe_2O_4$ and NiO, with porosity that ranged from 34% to 77% [13].

Figure 1.3 depicts four regimes of the heat transfer associated with CRUD, as determined by the coolant flow through the boiling chimneys and the surrounding porous medium. Under low heat flux, the chimneys are flooded with liquid coolant, giving the lowest effective thermal conductivity measured of 0.78 $Wm^{-1}K^{-1}$. At larger heat flux conditions, the mixture regime occurs where liquid coolant flows through the surrounding porous medium, then boils and exits as vapor through the chimneys. This boiling produces micro-convection and results in greatly enhanced effective thermal conductivity measured to average 6.1 $Wm^{-1}K^{-1}$. In the mixture regime, thin CRUD (< 15 μm) actually increases heat transfer when compared to a bare rod due to the increased subcooled boiling. Thicker CRUD (> 40 μm), however, inhibits heat transfer under the mixture regime. Under high heat flux conditions, lower regions of the CRUD may
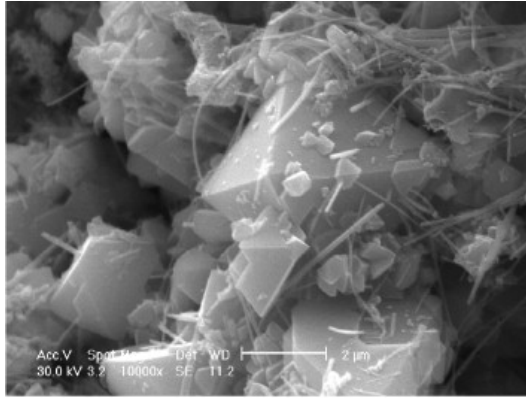
Element	Cr	Mn	Fe	Ni	Zr	Total
At %	0.72	1.95	46.07	25.91	25.35	100
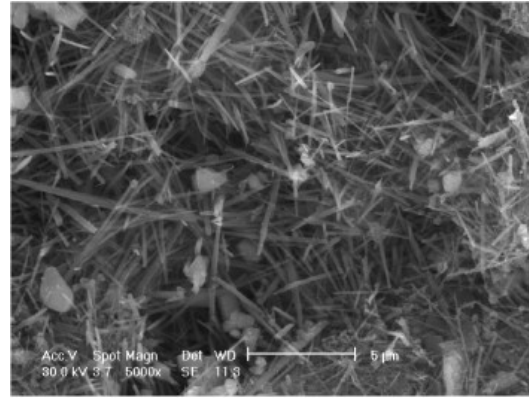
Element	Si	Cr	Mn	Fe	Ni	Zr	Total
At %	2.76	2.48	3.76	33.54	53.55	3.91	100

Figure 1.2: SEM photos and chemical composition of an octahedral crystal (left) and needle-like structures (right) in CRUD scrape samples (Reproduced from [15])
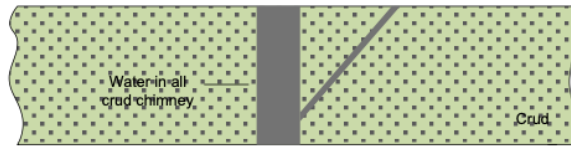
(a) Flooding model: Liquid flooding in crud chimney or pores
(lower power operating conditions)
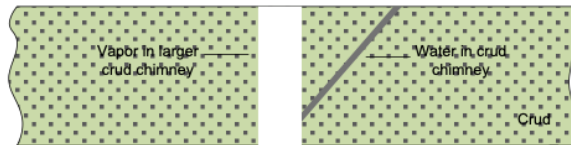
(b) Mixture model: Vapor and liquid mixed in crud chimney or
pores (normal high power operating conditions)
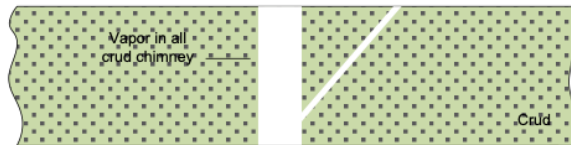
(c) Dryout model: Crud dryout gradually from the bottom to the
top of crud layer (higher power operating conditions)
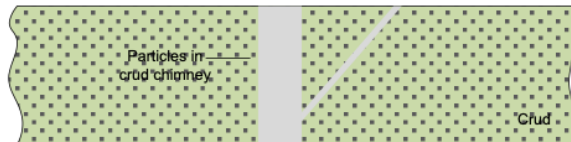
(d) Particle model: Crud pores filled or partially filled with solid
particles

Figure 1.3: Four regime model of heat transfer mechanisms within CRUD
(Reproduced from [13])

contain only vapor in the dryout regime, where the effective thermal conductivity decreases to about 2.0 $Wm^{-1}K^{-1}$. Lastly, if the subcooled boiling is sustained for enough time to concentrate soluble species leading to precipitation, the pores and chimneys are filled giving a solid scale with a measured effective thermal conductivity of 1.18 $Wm^{-1}K^{-1}$.

1.1.6 Lithium Borate Solid Phases

Lithium metaborate ($LiBO_4$) and/or lithium tetraborate ($Li_2B_4O_7$) are believed to be present in CRUD during reactor operation [12]. Precipitation of these compounds is believed to trap boron within the CRUD, and as such, can produce AOA. However, lithium borates have never been directly observed in reactor fuel CRUD samples. Lithium borates would likely dissolve during shutdown for several reasons, which would limit the ability to detect these phases in CRUD samples. Lithium and boron coolant concentrations are greatest at the beginning of the cycle and decrease throughout the cycle as burnup increases, reaching their lowest concentration just before shutdown. Lithium borates exhibit retrograde solubility, making them more likely to dissolve at lower temperatures. Also, and perhaps most importantly, it is believed that boiling is required to sustain lithium borate precipitation by concentrating aqueous boron and lithium within the CRUD. Consequently, the drop in heat flux due to shutdown could result in the dissolution of lithium borates.

Measurement of Li and B coolant levels increase sharply during shutdown or during power drops, and then return to original concentrations when the power is restored. Figure 1.4 shows the soluble concentration of B and Li in the coolant and the power history from the Palo Verde plant over the period of about 10 days around the time of shutdown [14]. As shown in Figure 1.4, shutdown is indicated by the sudden drop in power from 100 % to 0 %. In the time period immediately after, lithium and boron concentrations increase, reaching their maximum values within two days. As power is subsequently increased, the Li and B concentrations in the coolant correspondingly increase. This observation, termed "hideout" [14], is indicative of Li and B containing solid phases in the CRUD that re-dissolve in the coolant at shutdown when temperature drops and boiling no longer occurs.

While the Li hideout behavior can be explained by precipitation and dissolution of lithium borates, the B hideout can only partially be explained by the presence of these compounds. The Li coolant concentrations shown in Figure 1.4 fluctuate by less than 1.0 ppm

9
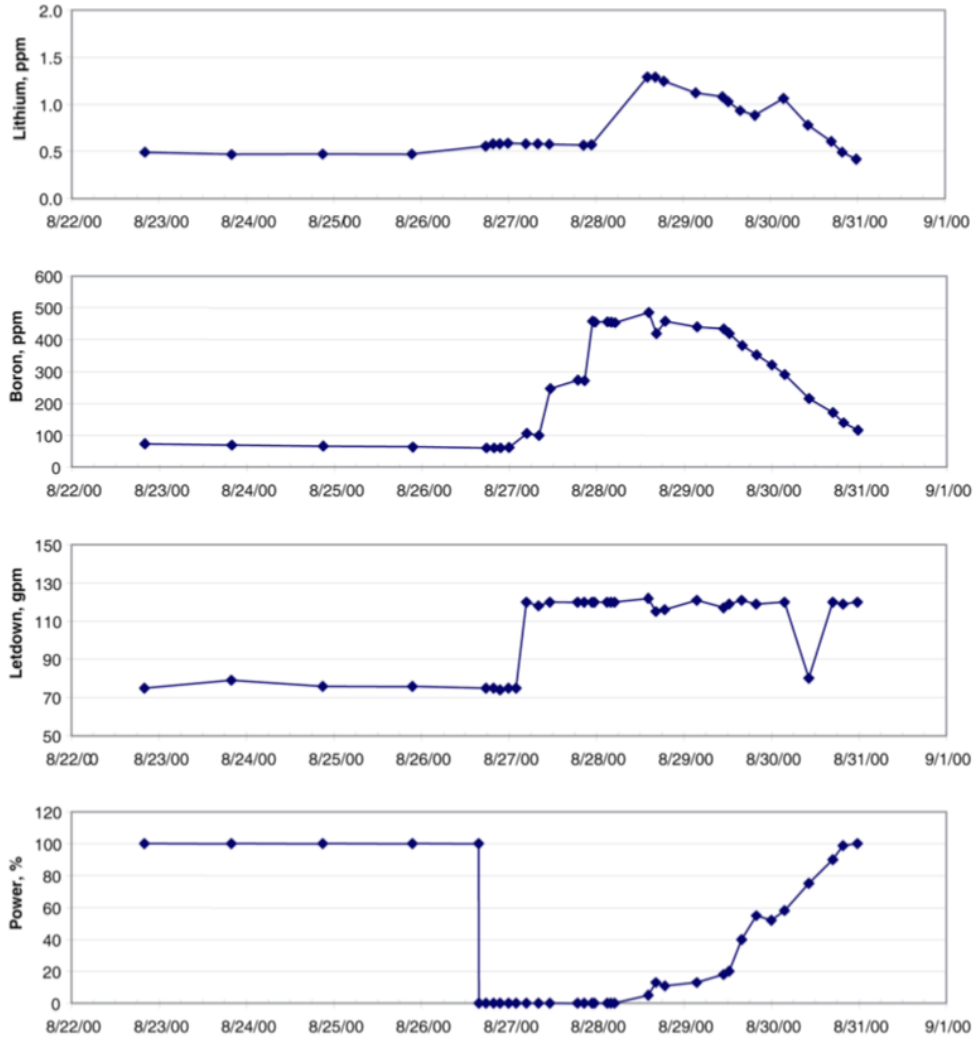
Figure 1.4: Reactor Coolant System (RCS) Lithium Return and Hideout Behavior Exhibited During End-of-Cycle at Palo Verde Unit 2 Cycle 9 (Reproduced from [14])

during the full power fluctuations, while the B coolant concentration increases by more than 400 ppm. Therefore, a mass balance of Li vs B release hints that neither lithium metaborate ($LiBO_2$) nor lithium tetraborate ($Li_2B_4O_7$) precipitation alone can fully explain this observation, suggesting the possibility of a separate CRUD hideout phase that contains boron but with little to no lithium.

Experiments have been performed with the goal to observe lithium borates. A test loop was constructed to identify the root cause for AOA with the goal to maintain all the compounds incorporated within a synthesized CRUD that exhibit retrograde solubility [19]. PWR coolant conditions were simulated in a small pressure vessel, and a resistance-heated Zr wire was used as a surface for CRUD formation. After growing CRUD to a desired thickness, the coolant was rapidly flushed out of the pressure vessel using a blowdown tank, isolating the CRUD from the coolant. The temperature of the sample was maintained at a constant value. The synthesized sample was then characterized. The thickness of the deposit was found to range from 25 to 100 μm thick. The B concentration was found to be 9.87 to 12.1 at%. The Li/B ratio was 0.112 ± 0.026, for which neither $LiBO_4$ nor $Li_2B_4O_7$ can solely account. This experimental result reinforces the conclusion that phase(s) other than lithium borates must exist to account for boron retention.

1.1.7 Comparison of CRUD from AOA and non-AOA Cycles

CRUD samples from 12 different plant cycles that either did, or did not, experience AOA have been analyzed previously [18, 20], as indicated in Figure 1.5. CRUD thickness and dissolved metal ion concentrations were measured, and crystalline phase identification was performed.

CRUD flakes obtained from nuclear reactors that experienced AOA tends to be thicker, with flake thicknesses greater than 35 μm [9]. The Ni/Fe ratio increases with thickness in AOA CRUD and decreases in thickness in non-AOA CRUD. AOA CRUD contains many needle-like phases, while non-AOA CRUD contains few needles. Nickel ferrite ($NiFe_2O_4$) is present, and NiO is possible, in both kinds of CRUD. Ni metal tends to only exist in low amounts in AOA CRUD, although it is likely that any Ni metal present oxidizes during shutdown and fuel storage, altering these results. The residence time of the CRUD in the core, measured by the [54]Mn/Fe ratio, tends to be less than 100 days for non-AOA CRUD and 100-250 days for AOA CRUD

	Ni Ferrite	NiO	Ni	Ni₂FeBO₅	Needles Ni/Fe>2	ZrO₂	FeOOH	NiFeCrZnO "Zinc Crud"	Carbon
Diablo 1R11	**3**	**3**	**2**			2		3	3?
Summer R12	**3**	**3**			2	**3**	**3**		
Vogtle 2 R8	**3**					**3**	**1**		
Byron 1 R10	**3**	**3**	**3**			1			
Vogtle 1 R10	**3**					**3**			
Vogtle 2 R9	**3**				2	**3**			**1**
Callaway R10	**3**	?		**2**	2	3	**1**		
Seabrook R5	**3**	**3**		?	3	**3**			
Callaway R9	**3**	**3**		**3**	3	**3**			

Key   3= Major Phase 2= Minor Phase 1=Trace Phase
Bolded when determined by XRD or Mössbauer   Not bolded when implied by SEM/EDS

Figure 1.5: Phase compositions of samples from various plant cycles
(Reproduced from [18])

[21]. Figure 1.5 lists the qualitative phase compositions from 9 plant cycles, in increasing magnitude of experienced AOA, with Callaway Cycle 9 experiencing the most significant AOA [18].

AOA CRUD exhibits a layered structure that non-AOA CRUD does not, as shown in Figure 1.6. Near the cladding, the CRUD tends to have large concentrations of either Ni_2FeBO_5 or $Ni_xFe_{3-x}O_4$, where x ranges from 0.05 to 1. The middle layer of an AOA CRUD flake is made up a porous monoclinic ZrO_2 layer, yet the lower cladding-side layer contains little Zr. This occurs because, during operation, the cladding-side layer has a slightly elevated pH similar to that of the coolant due to a high Li concentration and the buffering effect of lithium borate precipitates if present [22]. ZrO_2 tends to be more soluble in this high pH and diffuses through the lower layer [9]. The porous middle layer contains soluble boric acid that is highly concentrated due to boiling. Boric acid lowers the pH and causes ZrO_2 to precipitate. The outer-most coolant-side layer consists of loose particles with a high Ni concentration [21, 22].

1.1.8 Characterization of CRUD from Seabrook Cycle 5

Seabrook Cycle 5 occurred from December 10, 1995 to May 10, 1997. The maximum AOA experienced was -3.3%, and an analyzed CRUD scrape from this plant cycle had a thickness of 72 μm. X-ray diffraction (XRD) confirmed the presence of nickel ferrite and zirconia but could neither confirm nor exclude the presence of nickel oxide or bonaccordite. Bonaccordite is suspected to have been present due to the boron content observed by inductively coupled plasma optical emission spectrometry (ICP-OES) [5]. In addition, the crystals near the inner diameter have a Ni/Fe ratio of roughly 2, corresponding to bonaccordite (Ni_2FeBO_5). It was noted that for characterization performed with X-ray diffraction (XRD), bonaccordite lines are obscured by the background signal, making this phase difficult to definitively identify. The overall Ni/Fe and B/Ni weight ratios of the primary sample are 1.71 and 0.0639 respectively, measured by ICP-OES [5].

1.1.9 Characterization of CRUD from Callaway Cycle 9

Callaway Cycle 9 occurred from November 13, 1996, to April 9, 1998. Around June 1997, the AOA reached a record level of -14% [17], the greatest magnitude ever observed at any
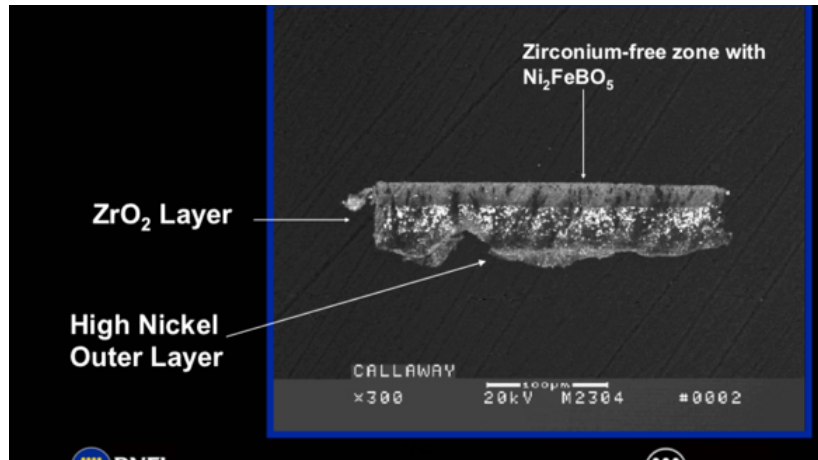
Figure 1.6: SEM showing the layering of an AOA CRUD flake from Callaway Cycle 9 (Reproduced from [21])

nuclear power plant. Consequently, the reactor power had to be derated to 70%. Cycles 10 and 11 also observed notable AOA [5, 17].

CRUD scrapes obtained from cycle 9 had a very large maximum thickness of 100 μm. Using Mössbauer spectroscopy, XRD, and other analysis techniques, the CRUD was found to contain about 50% Ni–Fe oxyborate (Ni_2FeBO_5), also known by the mineral name bonaccordite. Bonaccordite has the same crystal structure as ludwigite (Mg_2FeBO_5) and takes the shape of micron-scale needles. Figure 1.7 shows the needle-shaped bonaccordite particles, as well as octahedral-shaped nickel ferrite (trevorite), zirconia, and nickel oxide particles. It is hypothesized that the greater local Li concentrations and the subsequent raising of the pH make bonaccordite formation more favorable [17]. Isotopic abundance of the B in the needle-shaped crystals decreased from 19.9% ^{10}B to 10.2% ^{10}B, indicating the B had been trapped for at least 40 effective full-power days in the core. Bonaccordite phase formation is a possible mechanism, in addition to lithium borate formation for boron retention in the CRUD and differs from lithium borate in that its solubility is extremely low.

The double peaks in the Mössbauer spectra from the Calloway cycle 9 CRUD scrapes are shown in Figure 1.8 and are consistent with bonaccordite. The spectra were fit using library spectra of Ni_2FeBO_5, $NiFe_2O_4$, and α-FeOOH and treating the relative concentrations of each as adjustable parameters. Reference samples of Ni_2FeBO_5 and $NiFe_2O_4$ were synthesized and their Mössbauer spectra were matched to that of the CRUD scrapes [17]. It was noted that the Ni_2FeBO_5 crystals are highly insoluble [4], indicating that Ni_2FeBO_5 formation is likely not responsible for the B hideout and release behavior often observed in reactor coolant chemistry measurements [12].

The XRD patterns of both filter cake and flakes were obtained as well. The CRUD cake was found to be 40 wt% Ni_2FeBO_5, 30 wt% m-ZrO_2, 15 wt% NiO, and 15 wt % $NiFe_2O_4$. The CRUD flakes were found to be 50 wt% Ni_2FeBO_5, 30 wt% m-ZrO_2, 10 wt% NiO, and 10 wt % $NiFe_2O_4$. No Ni metal nor tetragonal ZrO_2 were observed. These results are fairly consistent with the Mössbauer spectroscopy results [17].

The boron content of CRUD samples has been observed to match the stoichiometry of Ni_2FeBO_5. Possible bonaccordite particles have also been observed on non-AOA fuel rods and on autoclave-corroded Alloy 600 material exposed to PWR primary coolant conditions [23].
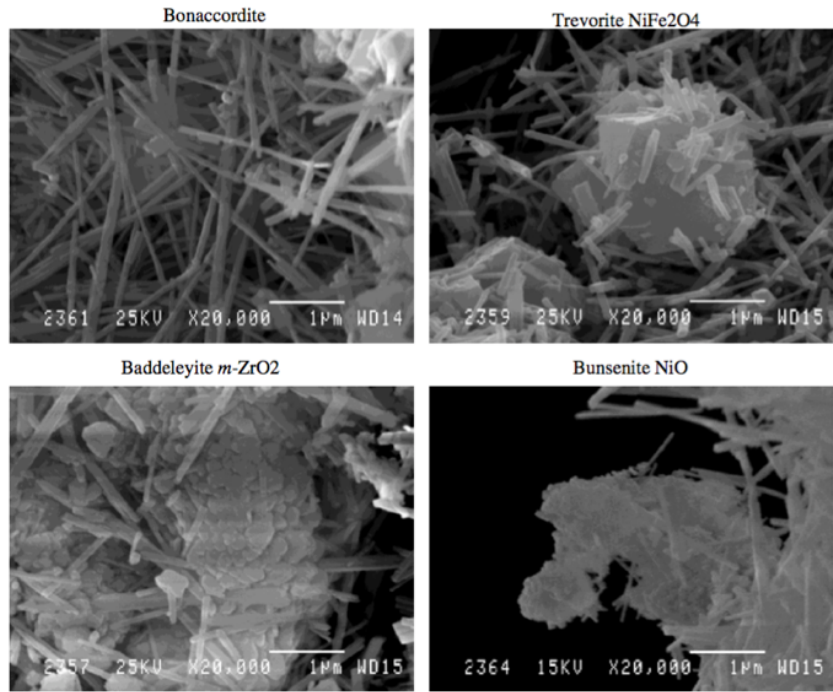
Figure 1.7: SEM micrographs of CRUD scrapes. The microstructural details of various CRUD constituents are visible. (Reproduced from [17])
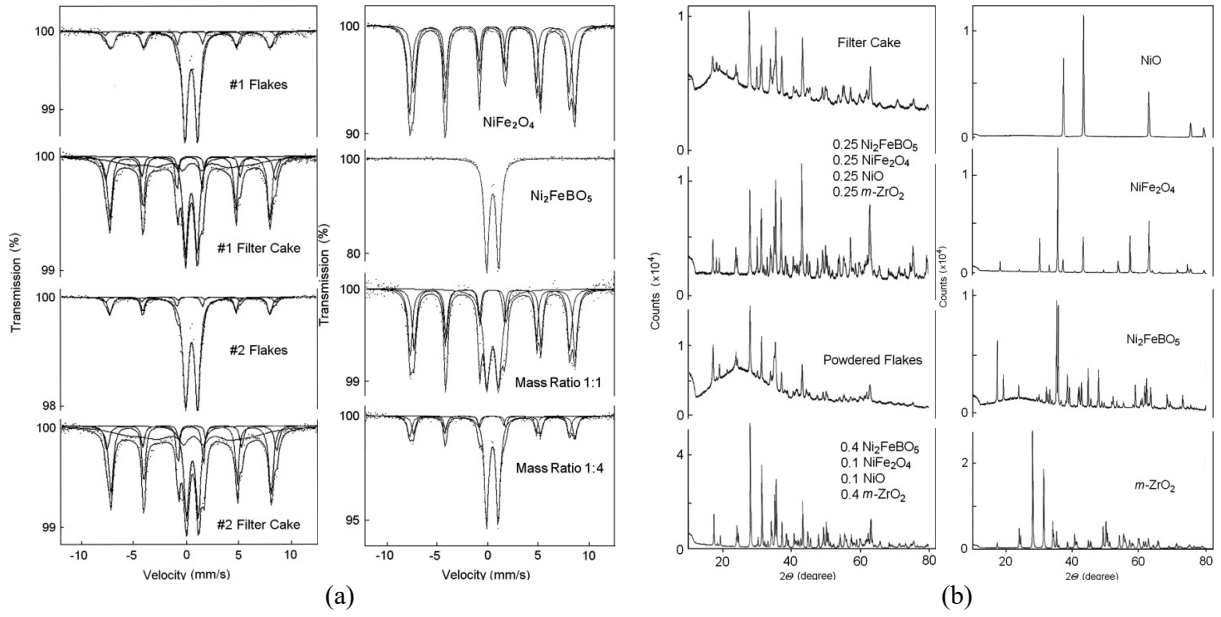
Figure 1.8: (a) ^{57}Fe Mössbauer transmission spectra of CRUD samples (left) and synthesized samples (right)   (b) X-ray power diffraction patterns of two fuel CRUD samples and their matching synthetic samples (left), and of individual reference specimens (right) (Reproduced from [17])

1.1.10 Characterization of CRUD from Callaway Cycle 10

Callaway Cycle 10 experienced AOA early in the cycle, likely due to highly crudded fuel rods that were reused from Cycle 9. The AOA reached -7% and slowly declined as the cycle continued. The CRUD samples analyzed from Cycle 10 exhibited the same needle-like bonaccordite crystals as Cycle 9, but were lower in concentration, making up 19-27 wt.% of the samples. Nickle ferrite was a more dominant phase making up 64-69 wt.% measured by ^{57}Fe Mössbauer transmission spectroscopy [5]. While Seabrook Cycle 5 and Callaway Cycle 9 CRUD exhibited a Zr-rich region in the center of the flake, the Zr-rich layer of Callaway Cycle 10 CRUD was close to the cladding.

1.1.11 Previous CRUD Models

The Electrical Power Research Institute (EPRI) developed and maintains the **B**oron-Induced **O**ffset **A**nomaly (BOA) explicit calculation code which is used by the industry as a screening tool for cycle designs to assess AOA risk [12, 14]. BOA performs a mass balance across the primary loop, keeping track of the release and deposition of corrosion products from various surfaces [8]. BOA also has models for the thermal hydraulics, transport, chemistry, and boron uptake within CRUD [9], upon which many of models in MAMBA are based [3].

EPRI also maintains a thermochemistry library use in CRUD modeling contained in the MULTEQ (MULTiple EQuilibrium) computer model. MULTEQ calculates high-temperature aqueous chemistry and can predict the precipitation of many solid CRUD-forming species [12, 22]. Boric acid aqueous chemistry data up to 200 ºC [24] is amended by statistical thermodynamic calculations to consider mixed solvent solution properties [3]. Temperature-dependent equilibrium constant correlations follow the form of Equation 1.1 where A, B, and C are constants, which may not extrapolate well to the saturation temperature if fit to lower temperature data.

$$\log K = A/T + B + C \log T \tag{1.1}$$

1.2 Motivation

CRUD poses a challenging problem for the nuclear industry. Problems such as AOA are directly dependent on the chemical makeup of deposits, but the chemical makeup is not well-understood. Measurements of CRUD are costly and challenging, and little data exists. Analysis

of samples from spent fuel pools does not truly represent CRUD during operation due to chemical changes that occur throughout the length of the fuel cycle and after shutdown. Therefore, computational modeling can provide an effective alternative to building an understanding of CRUD formation and characteristics. Still, CRUD modeling efforts have not successfully been able to fully simulate the solid chemical composition to a degree that accounts for the observed composition of samples [17]. Notably, bonaccordite (Ni_2FeBO_5) has been a missing phase in the previous models but is clearly observed in CRUD samples. Moreover, bonaccordite formation provides a significant boron retention mechanism that has been observed yet not predicted by modeling efforts. Lithium borates also pose an issue in that they are likely to precipitate, contributing to AOA, but have not been observed from samples or by experiment. By advancing the solid chemistry models in MAMBA, the chemical makeup of CRUD can be better explained.

1.3 Dissertation Research Objective

By combining detailed thermodynamic modeling with continuum modeling, this dissertation better explains the chemical composition of CRUD, both at the end and throughout the fuel lifetime. First, thermodynamic modeling was used to predict the aqueous chemistry and a set of potential precipitation reactions within CRUD. Then, continuum modeling combined with Bayesian estimation determined the kinetic rates of precipitation reactions in order to explain the characterizations of CRUD samples from two nuclear power plants where AOA occurred. This dissertation furthers the ability of computational methods to describe and predict CRUD formation and composition throughout a reactor fuel cycle, which provides a new and more comprehensive understanding of the mechanisms by which CRUD causes issues such as AOA and CIPS.

CHAPTER 2. METHODOLOGY

2.1 Thermochemistry

2.1.1 Helgeson-Kirkham-Flowers (HKF) Formalism

The Helgeson-Kirkham-Flowers (HKF) model provides a basis to predict thermodynamic properties of aqueous solutions at a broad range of temperatures and pressures. The complete revised Helgeson-Kirkham-Flowers (HKF) formalism [25, 26] gives the partial molal thermodynamic properties such as Gibbs of formation, entropy, heat capacity, and volume for individual aqueous species at elevated temperature and pressure. It combines non-electrostatic and electrostatic contributions. The non-electrostatic contribution considers hydrogen bonding effects important at low temperatures. The electrostatic contribution uses the Born equation to consider long-range ion-solvent polarization important at high temperatures [25, 26].

Important for equilibrium calculations, the standard partial molar Gibbs of formation is expressed by

$$\Delta \bar{G}^0 = \Delta \bar{G}^0_{f,P_r,T_r} - \bar{S}^0_{P_r,T_r}(T - T_r) + a_1(P - P_r) + a_2 \ln\left(\frac{\Psi+P}{\Psi+P_r}\right) + \left(\frac{1}{T-\Theta}\right)\left(a_3(P - P_r) + \right.$$

$$a_4 \ln\left(\frac{\Psi+P}{\Psi+P_r}\right)\right) - c_1 \left(T\ln\left(\frac{T}{T_r}\right) - T + T_r\right) - c_2\left(\left(\left(\frac{1}{T-\Theta}\right) - \left(\frac{1}{T_r-\Theta}\right)\right) - \frac{T}{\Theta^2}\ln\left(\frac{T_r(T-\Theta)}{T(T_r-\Theta)}\right)\right) +$$

$$\omega\left(\frac{1}{\epsilon} - 1\right) - \omega_{P_r,T_r}\left(\frac{1}{\epsilon_{P_r,T_r}} - 1 - Y_{P_r,T_r}(T - T_r)\right) \tag{2.1}$$

where T is temperature in Kelvin. P is pressure in bars. P_r = 1 bar is the reference pressure. T_r = 298.15 K (25 °C) is the reference temperature. Ψ = 2600 bar is the solvent pressure parameter. Θ = 228 K (-45.15 °C) is the solvent temperature parameter. There are nine parameters that are unique to each individual species. $\Delta \bar{G}^0_{f,P_r,T_r}$ and $\bar{S}^0_{P_r,T_r}$ are the Gibbs of formation and entropy respectively at the reference temperature and pressure. The parameters a_1, a_2, a_3, a_4 are integration constants for volume, and c_1, c_2 are integration constants for heat capacity. ω is the Born coefficient. ϵ is the dielectric constant of water, and $Y = \frac{1}{\epsilon}\left(\frac{\partial \ln \epsilon}{\partial T}\right)_P$.

2.1.2 Pitzer Equations

Given the HKF model calculates the standard Gibbs energy of formation for individual species, the Pitzer equations calculate the excess Gibbs energy of an aqueous solution due to nonideality. The Pitzer equations account for the electrostatic interactions between ions and the solvent [27]. In these equations, the Debye-Hückel expression accounts for interactions of ions dissolved in water at infinite dissolution [28], and a virial expansion accounts for short-range interactions between the dissolved species at higher concentrations. Considering only binary interactions is sufficient for most purposes. By considering only the interactions between cations and anions to be significant, the excess Gibbs energy for mixed electrolytes simplifies to the Equation 2.2. Terms describing interactions of like-charged ions and of neutral solutes are omitted. A thorough description of the Pitzer equations is described by Pitzer and Kenneth [27].

$$\frac{G^{ex}}{w_w RT} = f(I) + 2 \sum_c \sum_a m_c m_a [B_{ca} + (\sum_c m_c z_c) C_{ca}] \tag{2.2}$$

The first term is the Debye-Huckel term given by the following equation.

$$f(I) = - \left(\frac{4 I A_\phi}{b}\right) \ln\left(1 + b I^{1/2}\right) \tag{2.3}$$

The Debye-Huckel parameter is given by

$$A_\phi = \left(\frac{1}{3}\right) \left(\frac{2\pi N_o \rho_w}{1000}\right)^{\frac{1}{2}} \left(\frac{e^2}{\epsilon k T}\right)^{\frac{3}{2}} \tag{2.4}$$

where N_o is Avogadro's number, ρ_w is the density of water, e is the electronic charge, k is the Boltzmann's constant, and ϵ is the dielectric constant. The constant b is 1.2 (kg·mol⁻¹)¹ᐟ²

The following equations give the parameters for a cation M and an anion X.

$$B_{MX} = \beta_{MX}^{(0)} + \beta_{MX}^{(1)} g\left(\alpha_1 I^{\frac{1}{2}}\right) + \beta_{MX}^{(2)} g\left(\alpha_2 I^{\frac{1}{2}}\right) \tag{2.5}$$

$$g(x) = 2[1 - (1 + x)\exp(-x)]/x^2 \tag{2.6}$$

$$C_{MX} = \frac{C^\phi}{2|z_M z_X|^{1/2}} \tag{2.7}$$

If one or both of the ions are singularly charged, $\alpha_1 = 2.0$ (kg·mol⁻¹)¹ᐟ² and $\alpha_2 = 0$ (kg·mol⁻¹)¹ᐟ², eliminating the need for $\beta_{MX}^{(2)}$. The following equations give the activity coefficients for mixed electrolytes.

$$\ln \gamma_M = z_M^2 F + \sum_a m_a (2 B_{Ma} + Z C_{Ma}) + z_M \sum_c \sum_a m_c m_a C_{ca} \tag{2.8}$$

$$\ln \gamma_X = z_X^2 F + \sum_c m_c (2 B_{cX} + Z C_{cX}) + |z_X| \sum_c \sum_a m_c m_a C_{ca} \tag{2.9}$$

$$F = f^\gamma + \sum_c \sum_a m_c m_a B'_{ca} \tag{2.10}$$

$$f^{\gamma} = -A_{\phi}\left[\frac{I^{\frac{1}{2}}}{1+bI^{\frac{1}{2}}} + \left(\frac{2}{b}\right)\ln\left(1+bI^{\frac{1}{2}}\right)\right] \tag{2.11}$$

$$B'_{MX} = \left[\beta^{(1)}_{MX} g'\left(\alpha_1 I^{\frac{1}{2}}\right) + \beta^{(2)}_{MX} g'\left(\alpha_2 I^{\frac{1}{2}}\right)\right]/I \tag{2.12}$$

$$g'(x) = -2\left[1 - \left(1 + x + \frac{x^2}{2}\right)\exp(-x)\right]/x^2 \tag{2.13}$$

$$Z = \sum_i m_i |z_i| \tag{2.14}$$

2.1.3 Estimating Thermodynamic Properties for Unknown Solids

The thermodynamic properties of compounds of interest such as bonaccordite (Ni_2FeBO_5) have not been measured experimentally and must therefore be estimated using computational approaches. Density functional theory (DFT) calculations available from the literature [29-31] estimated the enthalpy of formation for compounds such as bonaccordite. Heat capacity can be estimated using the Neumann-Kopp Additivity Rule, and entropy can be estimated using the Latimer approach [32]. Using these thermophysical properties, the Gibbs energy of formation can be calculated and applied in thermodynamic calculations. In the case of defected crystals, the compound energy formalism [33] is used to model the solution phases with sublattices.

2.1.4 CALPHAD

The CALPHAD (Computer Coupling of Phase Diagrams and Thermochemistry) approach is applied to modeling the internal chemistry of the CRUD. A global minimization of the Gibbs free energy is performed in this method to calculate the conditions of a system at equilibrium. The method facilitates the rapid evaluation of model parameters, especially in multicomponent systems [33, 34].

2.2 MAMBA Code

MAMBA is a finite code that simulates the growth, structure, chemistry, and thermal transport of CRUD [3, 6, 7, 35]. As part of the VERA suite of codes, MAMBA is coupled to other codes to simulate AOA and CILC [36-40]. MAMBA provides CRUD thickness and boron content including [10]B depletion to a neutronics code to allow for power calculations. MAMBA in return requires power output from the cladding surface, coolant boundary temperatures, the coolant chemical composition affected by corrosion along all surfaces in the primary loop, and

the coolant turbulent kinetic energy (TKE) calculated by a thermal hydraulics code. The coolant chemistry includes boric acid, lithium, hydrogen, particulate nickel/iron corrosion products, and soluble nickel/iron corrosion products. This information allows MAMBA to calculate surface deposition. This chemistry can be user-defined, or with recent additions can be calculated by source term models, which account for the release and deposition of corrosion products throughout the primary loop [41]. The TKE at the CRUD-coolant interface allows MAMBA to calculate erosion and release of the CRUD that is prevalent near the cladding spacer grids. This TKE is either calculated by a thermal hydraulics code or is user-defined. The main components in MAMBA are equilibrium chemistry, the growth kinetics, heat and mass transfer, and the internal chemistry and precipitation. [42]

2.2.1 Nodal Structure

Coolant, species precipitation and CRUD growth, and heat transport each primarily occurs in the radial dimension in CRUD. MAMBA therefore solves the one-dimensional transport problem and extends to three-dimensions by solving additional problems along the axial and azimuthal dimensions. [42]

MAMBA has three node types, as shown in Figure 2.1. The boundary node located at the CRUD-coolant interface is where growth by particulate deposition is considered. Particulates from the coolant decrease the porosity as they fill this node until the node becomes 30% filled. It is then converted into an internal node, and a new boundary node is activated.

The internal nodes are where the boiling, transport, and precipitation models are active. Internal boiling of the coolant acts a heat sink and increases the local soluble species concentrations. Diffusion of these species back towards the coolant interface is considered. As the species become supersaturated, precipitation of various solids is considered, which decreases the porosity. If a node becomes 99% filled, these models are deactivated, and only the heat transfer across the solid node is considered.

23

Cladding

Inactive node

Boundary node

Internal node

Filled node
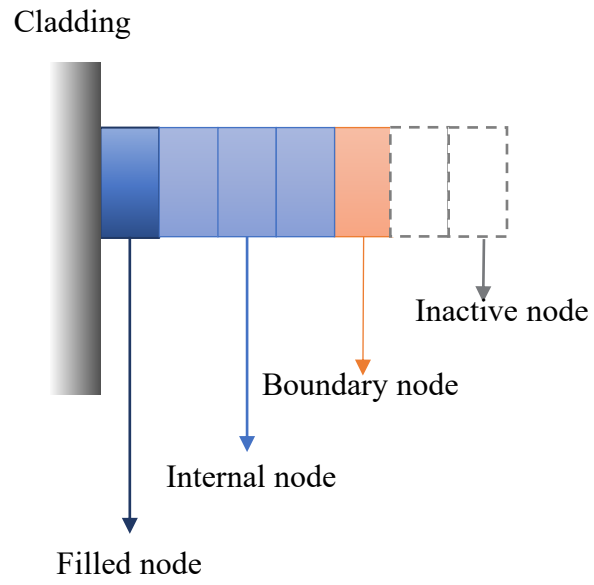
Figure 2.1: Depiction of the nodal structure in MAMBA [42]

2.2.2 Heat and Mass Transfer

Boiling occurs along chimney walls, acting as a heat sink. Heat and mass flow from the surrounding porous medium to the chimney in the so-called wick boiling model. The macroscale volumetric heat sink due to boiling is taken as an average heat flux through chimney walls. This volumetric heat sink due to sub-nucleate boiling at the chimney walls is given by

$$\dot{Q}_{snb}(T) = 2\pi R_{ch} N_{ch} h_{cw}(T - T_{sat}) \tag{2.15}$$

where h_{cw} is the heat transfer coefficient at the chimney wall. T_{sat} is the saturation temperature. R_{ch} is the characteristic radius of a chimney, and N_{ch} is the number density of active chimneys per unit area. MAMBA uses this heat flux to solve the one-dimensional heat conduction equation in cylindrical coordinates. The effective thermal conductivity of the CRUD is defined based on experimental data from the WALT loop experiment [13, 42].

Coolant mass leaves each internal node due to steam generation. Both liquid and steam exit through the boiling chimneys based on the chimney vapor fraction f_v. MAMBA computes the liquid flux along the radial dimension by conservation of mass. The total radial liquid flux rate due to boiling is given by

$$\frac{d\dot{\phi}_T^{(l)}}{dr} = \frac{\dot{Q}_{snb}}{f_v H_{fg}} \tag{2.16}$$

where H_{fg} is the enthalpy of vaporization.

Soluble species travel along with the liquid flux through the porous CRUD. As coolant leaves as vapor, these species are left behind, becoming more concentrated. The greater concentrations near the cladding allow for diffusion of these species back towards the coolant interface. In addition, some amount of these species leaves through the boiling chimneys in the entrained liquid. In the case of boric acid and dissolved hydrogen, species can enter the vapor phase and exit with the steam. The equation for the transport of the i-th species is

$$\frac{d}{dr}\left[\left(D\frac{dc_i}{dr}\right)\right] - \frac{\dot{\phi}_T^{(l)}}{\rho_w}\frac{dc_i}{dr} + c_i^v \frac{\dot{Q}_{snb}}{H_{fg}} + c_i \frac{\dot{Q}_{snb}}{H_{fg}}\left(\frac{1-f_v}{f_v}\right) = 0 \tag{2.17}$$

where D is the diffusivity. c_i is the concentration of the i-th species. c_i^v is the species concentration in the vapor phase. ρ_w is the density of the coolant. [42]

2.2.3 Growing Thickness

The deposition of nickel ferrite and nickel metal particulates from the coolant onto the CRUD surface is the mechanism by which CRUD thickness increases. The kinetic equation for the concentration either nickel ferrite or nickel metal at the boundary node is

$$\frac{dc_i}{dt} = \left(k_i + k_{i,boil}q_s\right)c_{i,cool} - c_{i,erosion} \tag{2.18}$$

where k is the Arrhenius non-boiling deposition rate ($k = A\exp(-E/RT)$)

k_{boil} is the boiling deposition rate (cm^3 J^{-1})

q_s is the subnucleate boiling heat flux at the CRUD surface (W cm^{-2})

c_{cool} is the particulate concentration in the coolant

$c_{erosion}$ is the decrease in the growth rate due to erosion

Typical calculations performed in MAMBA consider only nickel ferrite deposition at the surface, neglecting nickel metal deposition as an unnecessary complication for many tasks [42]. However, the work presented here accounts for Ni metal deposition due to necessity.

2.2.4 Thermochemistry in MAMBA

MAMBA determines the equilibrium aqueous chemistry in the coolant and throughout the CRUD, which informs the internal reaction calculations. The thermodynamic stability of a solid is expressed by the equilibrium concentrations of cations required to precipitate the solid, which informs the precipitation reaction rate.

MAMBA solves for the aqueous thermochemistry in two parts. Since Ni and Fe exist in very low concentrations comparatively, the B-Li-H_2O system is solved independently to determine B and Li speciation and pH of the solution. Using this pH and the amount of dissolved hydrogen, MAMBA solves for the Ni and Fe speciation separately. Many of the equilibrium constant formulations utilized in MAMBA are adopted from BOA/MULTEQ. Standard Debeye-Huckel-type activity coefficients for aqueous ions are employed, which are valid for sufficiently low concentrations. Boric acid chemistry is adapted using correlations by Mesmer et al. [24]. The aqueous nickel and iron chemistry is given by the Reactions 2.19-2.24.

$$Ni^{2+} + H_2O \leftrightarrow NiOH^+ + H^+ \tag{2.19}$$

$$NiOH^+ + H_2O \leftrightarrow Ni(OH)_2 + H^+ \tag{2.20}$$

$$Ni(OH)_2 + OH^- \leftrightarrow Ni(OH)_3^- \tag{2.21}$$

$$Fe^{2+} + H_2O \leftrightarrow FeOH^+ + H^+ \tag{2.22}$$

$$FeOH^+ + H_2O \leftrightarrow Fe(OH)_2 + H^+ \tag{2.23}$$

$$Fe(OH)_2 + OH^- \leftrightarrow Fe(OH)_3^- \tag{2.24}$$

The solid precipitates considered in MAMBA include $NiFe_2O_4$, Ni, NiO, Fe_3O_4, and Ni_2FeBO_5, and $Li_2B_4O_7$. The only dissolution of a solid considered is that of $Li_2B_4O_7$. Solid precipitation reactions are given by reactions 2.25-2.30. In addition, MAMBA can consider the conversion of a solid phase to another compound by means of reaction with aqueous species, represented by reactions 2.31-2.32.

$$2Fe^{2+} + Ni^{2+}6 + 4H_2O \rightarrow NiFe_2O_4(s) + 6H^+ + H_2(g) \tag{2.25}$$

$$Ni^{2+} + H_2(g) \rightarrow Ni(s) + 2H^+ \tag{2.26}$$

$$Ni^{2+} + H_2O \rightarrow NiO(s) + 2H^+ \tag{2.27}$$

$$3Fe^{2+} + 4H_2O \rightarrow Fe_3O_4(s) + 6H^+ + H_2(g) \tag{2.28}$$

$$Fe^{2+} + 2Ni^{2+} + B(OH)_3 + 2H_2O \rightarrow Ni_2FeBO_5(s) + 6H^+ + 0.5H_2(g) \tag{2.29}$$

$$2Li^+ + 4B(OH)_3 \leftrightarrow Li_2B_4O_7(s) + 5H_2O + 2H^+ \tag{2.30}$$

$$Ni(s) + 2Fe^{2+} + 4H_2O \leftrightarrow NiFe_2O_4(s) + 4H^+ + 2H_2(g) \tag{2.31}$$

$$NiFe_2O_4(s) + Ni^{2+} + B(OH)_3 + 0.5H_2(g) \leftrightarrow Ni_2FeBO_5(s) + Fe^{2+} + 2H_2O \tag{2.32}$$
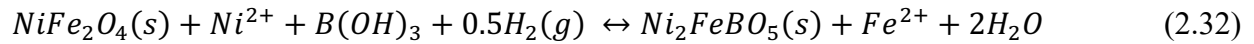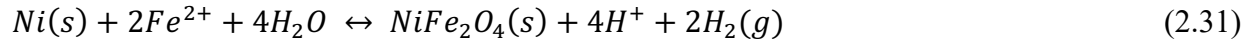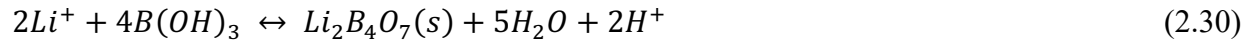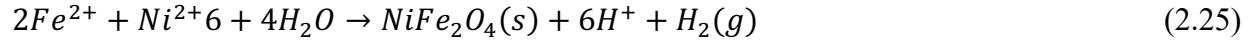
2.2.5 Internal Precipitation Reactions

As the soluble species concentrations increase within the CRUD, precipitation of solids becomes more favorable. MAMBA calculates the precipitation of these solids and the associated decrease in porosity due to precipitation. The kinetic rate of precipitation is considered to be proportional to the degree of supersaturation of metal cations, given as the difference in the local concentration and the thermodynamic equilibrium concentration. An Arrhenius kinetic rate parameter is used as the proportionality constant.

In the case of lithium tetraborate, as soon as precipitation is favorable the remaining porosity of node is filled immediately because of the large concentration of Li and B species, and the observed quickness with which precipitation and dissolution appear to occur based on coolant concentration measurements at reactor shutdown [14].

2.3 Bayesian Estimation

Bayesian calibration is a statistical method which computes the most probable value of uncertain parameters $\boldsymbol{\theta}$ in a model [43]. It is able to account for both uncertainty in observational measurements and deficiencies in the model. Prior probability distributions $f_\Theta(\boldsymbol{\theta})$ of the parameters are updated with each serial computation of the model by comparing to experimental data d. A likelihood function $\mathcal{L}(\boldsymbol{\theta}; \boldsymbol{d})$ describes how well the experimental data supports each parameter value. The posterior probability density function, $f_{\Theta|\mathrm{D}}(\boldsymbol{\theta}|\boldsymbol{d})$, is calculated using Bayes Theorem given information from the data for each parameter, as defined by Equation 2.33. The experimental data probability function $f_D(\boldsymbol{d})$ acts as a normalizing term, such that:

$$f_{\Theta|\mathrm{D}}(\boldsymbol{\theta}|\boldsymbol{d}) = \frac{f_\Theta(\boldsymbol{\theta}) \, \mathcal{L}(\boldsymbol{\theta};\boldsymbol{d})}{f_D(\boldsymbol{d})} \tag{2.33}$$

The best fit parameter values are taken by *maximum a posteriori* estimate (MAP), which is the set uncertain parameter values that result in the maximum value of the posterior probability density function [44]. In practice, the MAP is calculated by taking the minimum of the negative logarithm of the posterior [45].

A Gaussian likelihood function of the differences between model evaluations and the data is used, described by Equations 2.34 and 2.35. The error is modeled as additive and mutually independent of the search parameter [44], meaning each data value d_i is assumed to relate to the simulation value $q_i(\boldsymbol{\theta})$ by the addition of an error value ϵ_i that comprises both the measurement error and modeling error. A residual vector $\boldsymbol{r}$ sums the differences between the simulation values and the observational data, for all i up to n, and Σ_d is the covariance matrix of the Gaussian data uncertainties [45] as:

$$d_i = q_i(\boldsymbol{\theta}) + \epsilon_i \tag{2.34}$$

$$\mathcal{L}(\boldsymbol{\theta}; \boldsymbol{d}) = \frac{1}{\sqrt{(2\pi)^n |\Sigma_d|}} \exp\left(-\frac{1}{2} \boldsymbol{r}^T \Sigma_d^{-1} \boldsymbol{r}\right) \tag{2.35}$$

The Markov Chain Monte Carlo (MCMC) method [44] estimates parameter densities around a current state of parameters from the previous set of sample evaluations, then samples from the density to select the next state of parameter values. A combined delayed rejection and adaptive Metropolis-Hasting algorithm is used [45], which generates a candidate chain state from a multivariate Gaussian distribution with a proposal covariance based on the previous set of

sample evaluations, then decides based on an acceptance probability whether or not to move to the next chain state based on the reversibility of the move [46].

The Bayesian calibration is performed using the Dakota code developed at Sandia National Laboratory [45]. Dakota runs a predefined number of samples of the MAMBA model, generating proposed model parameters and analyzing the residuals to update the covariance matrix each time. The initial prior distributions of the search parameters have been assumed to be flat distributions over a range of reasonable values.

2.4 Summary of Methods

The MAMBA code simulates CRUD growth, structure, temperature, species transport, internal aqueous chemistry, and solid composition. Using CALPHAD modeling, the equilibrium concentrations and stable precipitates can be predicted at a range of conditions to obtain phase diagrams. Thermochemistry models are employed in MAMBA to predict which precipitation reactions are favorable. Then a Bayesian calibration is performed to identify the kinetic rates of the favorable reactions that best match observations from a CRUD sample. Lastly, the calibrated reaction rates are applied to separate CRUD samples from different plant cycles to evaluate the predictive power of the models and calibration results.

CHAPTER 3. BORON AND LITHIUM THERMOCHEMISTRY IN PWRS

3.1 Introduction

Boric acid ($B(OH)_3$) is the principal additive in pressurized water nuclear reactor (PWR) primary loop coolant to control reactivity through neutron adsorption [14]. Lithium hydroxide (LiOH) is added in conjunction with boric acid to maintain a pH of roughly 7.0 [47], which is alkaline at reactor coolant temperatures. When concentrations of these species become elevated due to trapping in CRUD, lithium borate solids are suspected to precipitate [9, 14], which due to the high neutron absorption cross sections of lithium and boron produce local neutron flux and power suppression. Boron trapping within the core leads to undesirable local depression and fluctuation of the reactor fission power, referred to as CRUD-Induced Power Shifts (CIPS), or Axial-Offset Anomaly (AOA) [9, 14].

Experimental data for PWR primary loop aqueous thermochemistry is largely available up to 300 °C [24, 48, 49]; however, temperatures in CRUD that sustains internal boiling reach the saturation temperature of 345 °C. The Helgeson-Kirkham-Flowers (HKF) model [25, 26] provides an appropriate extrapolation strategy to predict the thermochemistry under PWR CRUD conditions. A comprehensive database of boric acid chemistry is developed using the HKF framework, allowing for CALPHAD (CALculation of PHAse Diagrams) [33, 34] calculations at PWR CRUD conditions to predict the stability of the solid lithium borate precipitates likely to contribute to AOA.

3.2 Boric Acid Chemistry Speciation

Boric acid $B(OH)_3$ is a weak Lewis acid with the first ionization reaction associated with forming the borate anion:

$$B(OH)_3 + OH^- \leftrightarrows B(OH)_4^- \tag{3.1}$$

Mesmer, Baes, and Sweeton [24] performed potentiometric titrations of boric acid solution under hydrothermal conditions up to 300°C for low boron concentrations less than 0.020 mol·kg^{-1} and up to 200 °C for high boron concentrations reaching 0.597 mol·kg^{-1}. Two schemes were presented to fit their data [24] . The polyborates $B_2(OH)_7^-$ and $B_3(OH)_{10}^-$ are assumed to form in both schemes. Either $B_4(OH)_{14}^{2-}$ or $B_5(OH)_{18}^{3-}$ can be assumed to form to fit the data. The optimal formulas for these polyborates reported by many researchers [50-53] are $B_2O(OH)_5^-$,

$B_3O_3(OH)_4^-$, and $B_4O_5(OH)_2^{2-}$ or $B_5O_6(OH)_6^{3-}$, which all match the borate number and charge of the ions reported by Mesmer et al. [24].

The divalent tetraborate ion $B_4O_5(OH)_4^{2-}$ in the first scheme proposed by Mesmer et al. [24] has been observed in $Na_2B_4O_7$ or $K_2B_4O_7$ solutions through Raman spectroscopy performed by Y. Zhou et al. [52] and L. Applegarth et al. [53]. Zhou et al. [52] and Applegarth et al. [53] both observed $B_3O_3(OH)_4^-$, which was noted by Mesmer et al. [24] as being common to all satisfactory fitting schemes. Other notable polyborates suggested by Zhou et al. [52] include $B_3O_5(OH)_4^{2-}$ forming from $B_3O_3(OH)_4^-$ at high pH levels, and $B_5O_6(OH)_4^-$ in highly concentrated solutions. Applegarth et al. [53] possibly observed evidence of $B_2O(OH)_5^-$ that they report with caution. Applegarth et al. [53] also confirmed the main pentaborate species is $B_5O_6(OH)_4^-$ as opposed to $B_5O_6(OH)_6^{3-}$, which is inconsistent with the second scheme proposed by Mesmer et al. [24]. The polyborate species $B_3O_3(OH)_4^-$, $B_4O_5(OH)_4^{2-}$, and $B_5O_6(OH)_4^-$ have also been observed by Raman spectroscopy studies performed by Sasidharanpillai et al. [54] under hydrothermal conditions.

Palmer et al. [48] reinterpreted the results of Mesmer et al. [24] using the updated polyborate chemical formulae, providing equilibrium constants for Reactions 3.1-3.4 considered valid up to 200 °C.

$$2B(OH)_3 + OH^- \leftrightarrows B_2O(OH)_5^- + H_2O \tag{3.2}$$

$$3B(OH)_3 + OH^- \leftrightarrows B_3O_3(OH)_4^- + 3H_2O \tag{3.3}$$

$$4B(OH)_3 + 2OH^- \leftrightarrows B_4O_5(OH)_4^{2-} + 5H_2O \tag{3.4}$$

Sasidharanpillai et al. [54] report alternatively the original diborate species formula reaction (3.5) proposed by Mesmer et al. [24].

$$2B(OH)_3 + OH^- \leftrightarrows B_2(OH)_7^- \tag{3.5}$$

Wang et al. [55] provide an extensive thermodynamic description boric acid and metal borate systems using the HKF formalism and Pitzer equations. Several studies recently have reported discrepancies in speciation from spectroscopic experimental studies calculated values using this thermodynamic model [54, 56]. Instead of considering the typical orthoboric acid ($B(OH)_3$) as the only neutral aqueous species, the model by Wang et al. [55] assumes the formation of aqueous metaborate (BO(OH)) in conjunction with:

$$B(OH)_3 \leftrightarrows BO(OH) + H_2O \tag{3.6}$$

Contrary to the assumption made by Wang et al. [55], the Raman results by Arcis et al. [56] showed that metaborate (BO(OH)) does not exist in significant concentrations under relevant hydrothermal conditions. In addition, Wang et al. [55] consider $B_5O_6(OH)_6^{3-}$ to form in conjunction with $B_4O_5(OH)_4^{2-}$ formation, instead of as an alternative scheme as originally proposed by Mesmer et al. [24].

Wang et al. [55] provide HKF parameters for the associated lithium/sodium and borate ion pair, shown in reactions:

$$Li^+ + B(OH)_4^- \leftrightarrows LiB(OH)_4^0 \ (aq) \tag{3.7}$$

$$Na^+ + B(OH)_4^- \leftrightarrows NaB(OH)_4^0 \ (aq) \tag{3.8}$$

The contribution of ion pairs can instead be determined through means of an appropriate activity model [54] such as the Pitzer equations.

3.3 Calculation Methods

Reactions 3.1-3.4 are selected to describe boric acid hydrolysis and are denoted by xy where x is the boron number and y is the charge. The HKF formalism is utilized to calculate the standard partial molal Gibbs free energy of formation of each species, and equilibrium constants for the reactions are calculated from the change in the Gibbs free energy of formation, as:

$$K = \exp\left(\frac{-\Delta_r \bar{G}^0}{RT}\right) \tag{3.9}$$

The required HKF parameters for most species are available from the SUPCRT database [57-60]. Unavailable or deficient parameters are optimized in this study to match the best available data.

The thermodynamic properties of water are provided by the revised IAPWS 1995 formulation [61]. The formulation for the dielectric constant of water from Johnson and Norton [58] is utilized for consistency with the SUPCRT92 software [57].

The Pitzer equations provide a means of modeling the changes in activity of the borate anions ($B(OH)_4^-$, $B_2(OH)_7^-$, $B_3O_3(OH)_4^-$, $B_4O_5(OH)_4^-$) due to the presence of cations such as Li^+.

The CALPHAD software FactSage [34] is utilized to perform equilibrium calculations over a broad range of possible concentrations within CRUD to obtain a phase diagram of solid precipitates. The primary precipitates of interest are lithium metaborate ($LiBO_2$) and lithium tetraborate ($Li_2B_4O_7$) which are modeled as pure compounds.

3.4 Optimized HKF Parameters for K_w

Estimated K_w values often deviate at high temperatures based on the specific formulation. These deviations can result in differences in K_w values up to 0.4336 at the saturation temperature in a PWR when using the Marshall and Franck [62] formulation and the SUPCRT92 database [57]. IAPWS [63] recommends the formulation by Bandura and Lvov [64] as the most accurate. Using this formulation, the c_1, c_2, and ω_r HKF parameters for OH$^-$ are fit using a nonlinear least squares regression over a temperature range from the triple point temperature, $T_t = 0.01$ °C, to the critical temperature $T_c = 374$ °C, and over a density range from 0.1-1.2 g·cm^{-3} weighted to improve agreement to K_w at PWR pressure and temperatures. The properties $\Delta G^0_{f,T_r,P_r}, \Delta H^0_{f,T_r,P_r}, S^0_{T_r,P_r}$ and the volume constants a_1, a_2, a_3, a_4 are maintained from the SUPCRT92 database [57]. The resultant parameters, which are reported in Table 3.1, provide improved agreement between the resultant K_w and that of Bandura and Lvov [64] under PWR conditions. Figure 3.1 shows the difference between the HKF-calculated K_w and that of Bandura and Lvov [64] using the SUPCRT92 database [57] and the parameters in Table 3.1. The values using SUPCRT92 [57] and those from Table 3.1 both agree well with Bandura and Lvov [64] at 25 °C and low pressures, but both overestimate K_w at 25 °C as pressure increases. At 155 bar, the K_w values calculated using SUPCRT92 [57] show a large difference in Figure 3.1, especially at high temperatures, while the corresponding values from this work show improved agreement with the Bandura and Lvov [64] values at 155 bar and high temperatures. The values from this work only offer improved agreement for pressures up to 200 bar.

3.5 Optimized Borate Ion (B(OH)$_4^-$) HKF Parameters

HKF parameters for B(OH)$_3$ were first reported by Shock & Helgeson (1989) [60]. These parameters were subsequently updated by G.S. Pokrovski et al. (1995) [65], who fit the parameters to standard partial molar heat capacity (C_p^0) and volume (V^0) measurements by Hnedkovsky et al. [67]. G.S. Pokrovski et al. [65] report a greater value for S^0 than reported by Shock and Helgeson [60], however the $\Delta_f G^0$ or $\Delta_f H^0$ values were not updated accordingly. Therefore, the selected value of $\Delta_f H^0$ is edited according to Equation 3.10 for consistency. Subscript i denotes the constituent elements in their standard state.

$$\Delta_f G^0 = \Delta_f H^0 - TS^0 + (298.15 \text{ K}) \sum_i (S^0_{298})_i \tag{3.10}$$

Table 3.1: Standard Partial Molar Thermodynamic Data and Revised HKF EOS Parameters for Selected Aqueous Species

Species	$\Delta_f G^0$ (J mol^{-1})	$\Delta_f H^0$ (J mol^{-1})	S^0 (J mol^{-1} K^{-1})	a_1 (J mol^{-1} bar^{-1})	a_2 (J mol^{-1})	a_3 (J K mol^{-1} bar^{-1})	a_4 (J K mol^{-1})	c_1 (J mol^{-1} K^{-1})	c_2 (J K mol^{-1})	ω (J mol^{-1})
OH$^-$	-157297[a]	-230024[a]	-10.71[a]	0.52[a]	29[a]	7.70[a]	-116315[a]	5.07	-374390	694681
B(OH)$_3$	-968763[b]	-1072302	162.30[c]	3.35[c]	3138[c]	62.76[c]	-269450[c]	167.36[c]	-286604[c]	18828[c]
B(OH)$_4$$^-$	-1153152[c]	-1344026[c]	102.51[c]	2.31[c]	2648[c]	15.90[c]	-135980[c]	218.85	-991162	485517
B$_2$O(OH)$_5$$^-$	-1945529	-2129382	197.35	-4.43[d]	13227[d]	34.79[d]	0[d]	160.43	1644449	1115778
B$_3$O$_3$(OH)$_4$$^-$	-2573694	-2656607	168.69	0.34[d]	0[d]	107.2[d]	0[d]	116.67	955766	19748
B$_4$O$_5$(OH)$_4$$^{-2}$	-3378126	-3458056	44.71	1.19[d]	0[d]	0[d]	0[d]	-1366.81	15262857	-677431
LiOH	-451872[e]	-508356 [e]	7.95[e]	0.95[e]	-931[e]	27.69[e]	-112424[e]	-247.05[e]	4485708[e]	74558[e]
KOH	-437228[a]	-474300	108.37[a]	1.59[a]	621[a]	21.60[a]	-118834[a]	-25.62[a]	-301683[a]	-125520[a]

[a] Shock & Helgeson (1988) [59], [b] Shock et al. (1989) [60], [c] Pokrovski et al. (1995) [65], [d] Wang et al. (2013) [55], [e] Shock et al. (1997) [66]
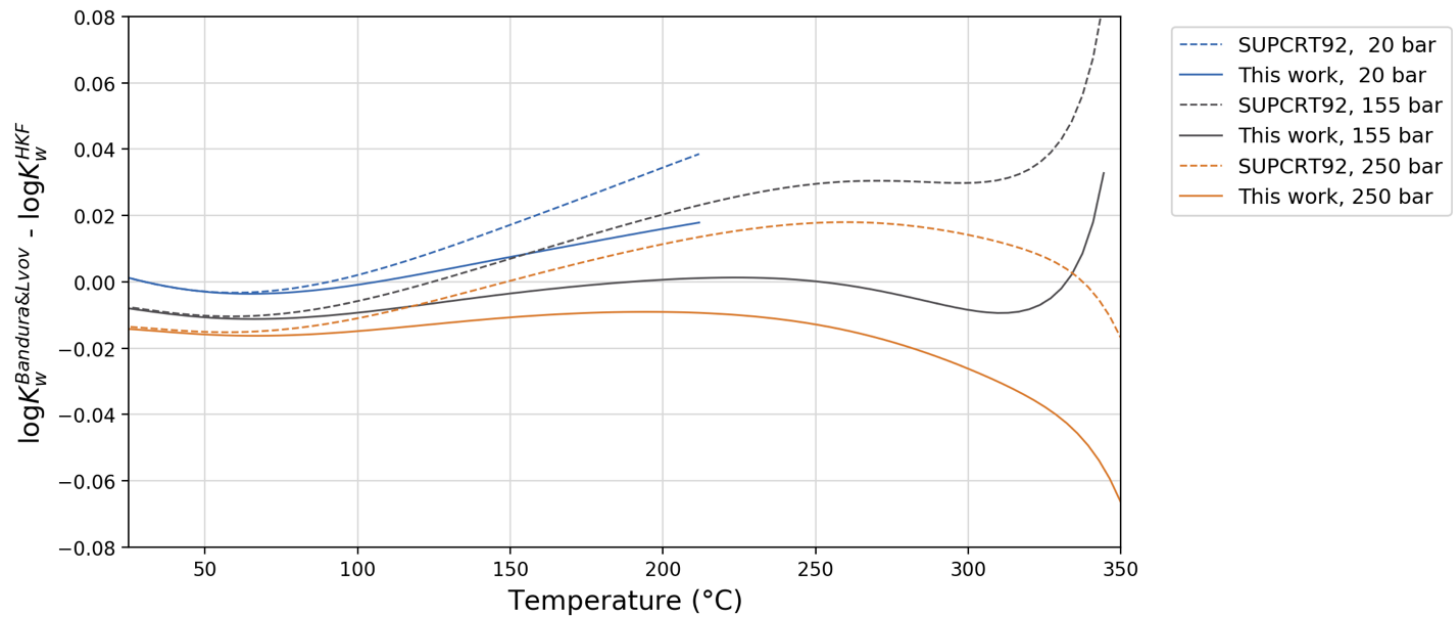
Figure 3.1: Deviation of logK$_w$ using the HKF parameters of SUPCRT92 [57] and reported in Table 3.1

For B(OH)$_4^-$, the volume constants a_1, a_2, a_3, a_4 in the HKF model are given by Pokrovski et al. [65] based on partial molar volume measurements [67]. Pokrovski et al. [65] fit the c_1, c_2, and ω parameters to the equilibrium constant for the association reaction reported by Mesmer et al. [24] based on measurements performed up to 290 °C. New c_1, c_2, and ω parameters are fit using the experimental ionization constants reported by Arcis et al. [56] based on AC conductivity measurements performed up to 350 °C. As was the case of the potentiometric titration data of Mesmer et al. [24], these measurements of the first ionization of boric acid were performed at low boron concentrations (less than 0.020 mol·kg^{-1}) to avoid the complexation of polyborate formation, yet differ by keeping the ionic strength sufficiently low to prevent short-range ion-ion interaction allowing Debye–Hückel theory to account for changes in activity. As recommended by Arcis et al. [56], the experimental data at 25, 100, and 250 °C were not included in the regression, as shown in Figure 3.2. Also included are the low temperature data from Owen and King [68] and Manov et al. [69] at zero ionic strength, in addition to the high temperature UV-visible spectroscopy data from Bulemela and Tremaine [70], and the lowest ionic strength data from Mesmer et al. [24], which were corrected to zero ionic strength. The equilibrium constant calculated using the HKF parameters by Wang et al. [55], also shown in Figure 3.2, show some deviation from the data at temperatures above 100 °C while the HKF parameters used in this work agree well with the data for temperatures up to 350°C.

3.6 Pitzer Parameters for Borate and Polyborate Species' Interactions with Alkali Metal Cations

Both Mesmer et al. [24] and Palmer et al. [48] provided expressions that give the ionic strength dependence of the first borate ion formation reaction. These expressions are both based on the low boron potentiometric titration data of Mesmer et al. [24] performed in a KCl solution where polyborate formation can be neglected. The scheme by Palmer et al. assumes the activity coefficient of the neutral boric acid species is unity ($\gamma_{B(OH)_3} = 1.0$), which gives the following relation between the equilibrium quotient Q, the equilibrium constant K, and the activity coefficients of the anions.

$$\log Q_{11} = \log K_{11} - \log \frac{\gamma_{B(OH)_4^-}}{\gamma_{OH^-}} \tag{3.11}$$
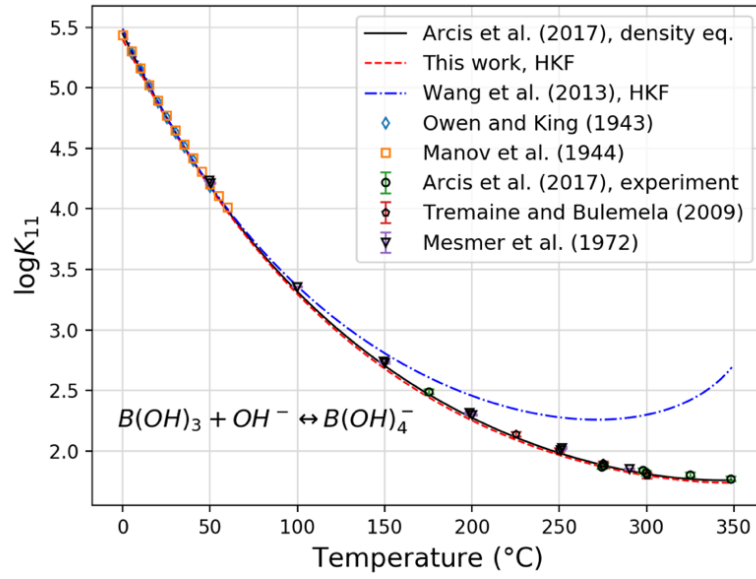
Figure 3.2: The equilibrium constant for the association reaction of the borate ion from different sources compared with values calculated using the fit HKF values

In fairly dilute solutions, the Debye-Hückel activity coefficients for charged ions are equal, yielding $\log\left(\frac{\gamma(B(OH)_4^-)}{\gamma(OH)^-}\right) = 0$. However, in solutions with greater concentrations, the activities can deviate due to short-range interactions with other ions. These short-range interactions can be accounted for through the use of Pitzer equations to describe the ($B(OH)_4^-$, K^+) binary interaction, which is considered analogous to any interaction with a univalent borate ion and an alkali metal cation (e.g. ($B(OH)_4^-$, Li^+), ($B_2O(OH)_5^-$, Li^+), ($B_3O_3(OH)_4^-$, Li^+)). The activity coefficient for OH$^-$ is given by the Debye-Hückel term for all ionic strengths.

Figure 3.3 shows the equilibrium quotient from Equation 3.11 as a function of ionic strength at various temperatures from 50 to 294 °C. The equilibrium quotient calculated using the HKF parameters in Table 3.1 and the Pitzer equation parameters in Table 3.2 shows good agreement with the experimental data and the corresponding fit from Mesmer et al. [24]. Figure 3.4 similarly shows the last term from Equation 3.11 as a function of ionic strength to compare the activity coefficient deviations from three models. The activity coefficient deviation given by the determined Pitzer model matches the data with slightly less error than the fits of Mesmer et al. [24] and Palmer et al. [48] and shows similar trends with temperature and ionic strength. The Palmer [48] fit shows greater variation with temperature at high ionic strength giving a broader range of values in Figure 3.4 at 1.0 mol·kg^{-1}. The Pitzer model values agree best with the Mesmer et al. [24] values at low temperatures, but differ slightly from the Mesmer et al. [24] values at high temperatures.

The ionic interaction behavior of the divalent tetraborate anion ($B_4O_5(OH)_4^{2-}$) differs from that of univalent anions and therefore requires different Pitzer parameters.

$$\log Q_{42} = \log K_{42} - \log\frac{\gamma_{B_4O_5(OH)_4^{2-}}}{\gamma_{OH^-}^2} \tag{3.12}$$

Palmer et al. [48] assumed the divalent species to be analogous with the divalent hydrogen phosphate ion (HPO_4^{2-}). Similar to the method of Palmer et al. [48], Pitzer parameters are fit to describe the (HPO_4^{2-} , K^+) binary interaction which are then be used to describe the ($B_4O_5(OH)_4^{2-}$, M^+) interaction.

Mesmer and Baes [71] performed potentiometric titrations to determine phosphoric acid dissociation equilibria up to 300 °C. At low concentrations of added base, the first ionization reaction is dominant and subsequent reactions can be neglected.

$$H_3PO_4 + OH^- \rightleftarrows H_2PO_4^- + H_2O \tag{3.13}$$
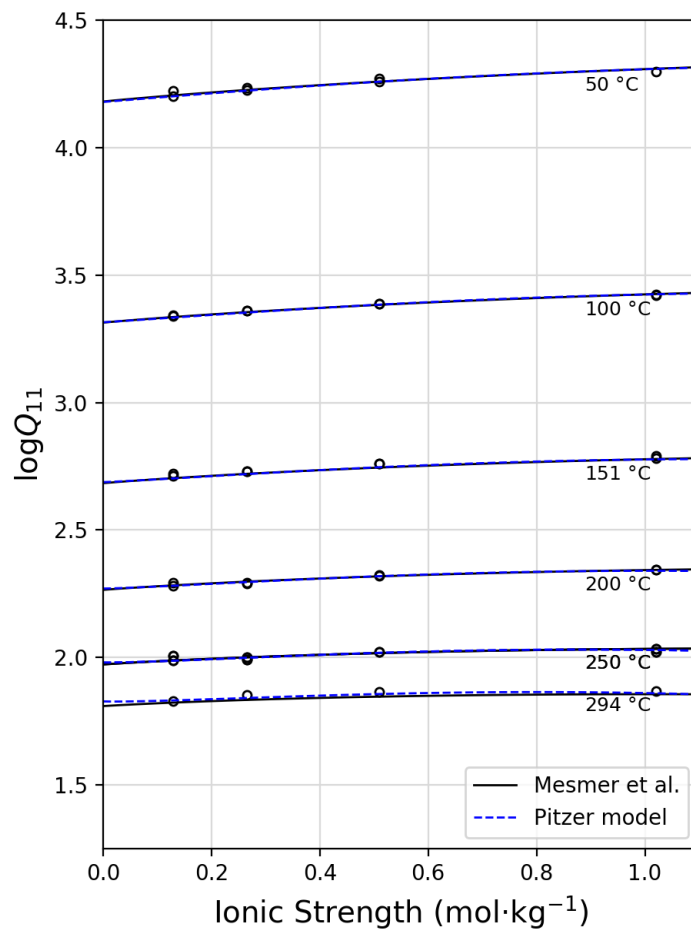
Figure 3.3: The dependence of $\log Q_{11}$ on ionic strength showing the experimental data and fit by Mesmer et al. [24] and the use of the Pitzer parameters in Table 3.2

Table 3.2: Pitzer Parameters for Binary Interactions with Alkali Metal Cations

Interaction	Pitzer Parameters	s(logQ)		
($B(OH)_4^-$, M^+)	$\beta_{ca}^{(0)}$ = –0.15950 – 2.5755E-4∗T	Pitzer eq. fit	Mesmer, Baes, Sweeton [24]	
	$\beta_{ca}^{(1)}$ = –0.39618 + 1.4053E-3∗T	0.0055	0.0057	
	C_{ca} = –3.2992E-3 + 5.8164E-4∗T			
($H_2PO_4^-$, M^+)	$\beta_{ca}^{(0)}$ = -3.9656 + 6.4795E-3∗T	Pitzer eq. fit	Mesmer & Baes [71]	
	$\beta_{ca}^{(1)}$ = 10.7874 – 1.6267E-2∗T	0.013	0.021	
	C_{ca} = 3.4183 – 6.1555E-3∗T			
(HPO_4^{2-} , M^+)	$\beta_{ca}^{(0)}$ = -3.4568 + 4.8743E-3∗T	Pitzer eq. fit	Mesmer & Baes [71]	
	$\beta_{ca}^{(1)}$ = 8.2720 – 8.6974E-3∗T	0.009	0.017	
	C_{ca} = 1.7406 – 2.9283E-3∗T			
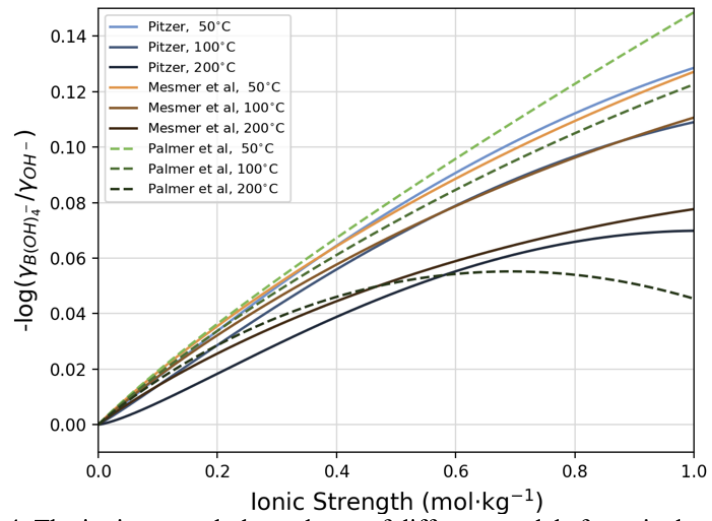
Figure 3.4: The ionic strength dependence of different models for univalent borate ions at 50, 100, and 200 °C

Here, the equilibrium quotient is described similarly to univalent borate reaction.

$$\log Q_1 = \log K_1 - \log \frac{\gamma_{H_2PO_4^-}}{\gamma_{OH^-}} \tag{3.14}$$

At higher concentrations of added base the second ionization reaction becomes prevalent.

$$H_2PO_4^- + OH^- \rightleftarrows HPO_4^{2-} + H_2O \tag{3.15}$$

$$\log Q_2 = \log K_2 - \log \frac{\gamma_{H_2PO_4^-}}{\gamma_{OH^-}\gamma_{H_2PO_4^-}} \tag{3.16}$$

Palmer et al. uses $-\log \frac{\gamma_{HPO_4^{2-}}}{\gamma_{OH^-}\gamma_{H_2PO_4^-}}$ as an estimate for $-\log \frac{\gamma_{B_4O_5(OH)_4^{2-}}}{\gamma_{OH^-}^2}$. In this study,

$-\log \frac{\gamma_{HPO_4^{2-}}}{\gamma_{OH^-}^2}$ is utilized instead, giving a greater deviation from an ideal solution. Pitzer

parameters are fit for the ($H_2PO_4^-$, K^+) and (HPO_4^{2-} , K^+) binary interactions along with new
equilibrium constants. The Pitzer model fits the data with less error than the original correlation
fit by Mesmer and Baes [71].
Rudolph [72] determined the equilibrium constant for Reaction 3.13 by way of Raman
spectroscopy. The equilibrium constants from this study compare well with the original fit by
Mesmer & Baes [71] and by Rudolph [72] with only slight deviations, as shown in Figure 3.5.
While the deviations are slight, $\log K_1$ from this study is lower at low temperatures, and $\log K_2$ is
greater at high temperatures. In addition, the ionic strength dependance calculated using the fit
Pitzer parameters deviates slightly from the original fit by Mesmer & Baes [71], especially at
lower temperature. Figure 3.6 shows the ionic strength dependance of the two equilibrium
quotients given by Equations 3.14 and 3.16. Altogether, the thermochemical properties
calculated using the HKF model and the Pitzer equations fit the phosphoric acid dissociation
equilibria data with little error.

Holmes et al. [73] reported a modified Pitzer equation model to describe aqueous
solutions of mono-hydrogenphosphate and di-hydrogenphosphate salts. The (HPO_4^{2-} , M^+)
binary interactions given by Holmes et al. [73] compare fairly well with the Pitzer equation
results calculated in this work, as shown in Figure 3.7. The results by Holmes et al. [73]
demonstrate only a slight difference between Na^+ and K^+ as the interacting metal cation, helping
to evaluate the assumption made here that the interaction with K^+ ions calculated from the
Mesmer and Baes [24] data can be used as an analogue for the interaction with any alkali metal
cation.
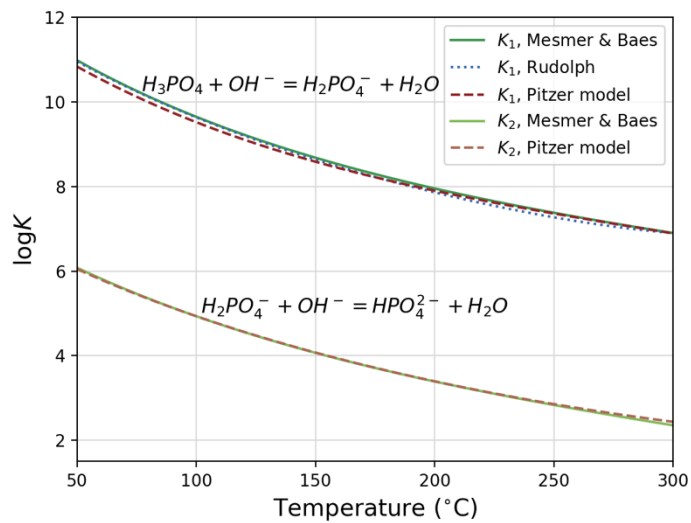
Figure 3.5: The equilibrium constants for the first and second ionization reactions of phosphoric acid, Reactions 3.13 and 3.15
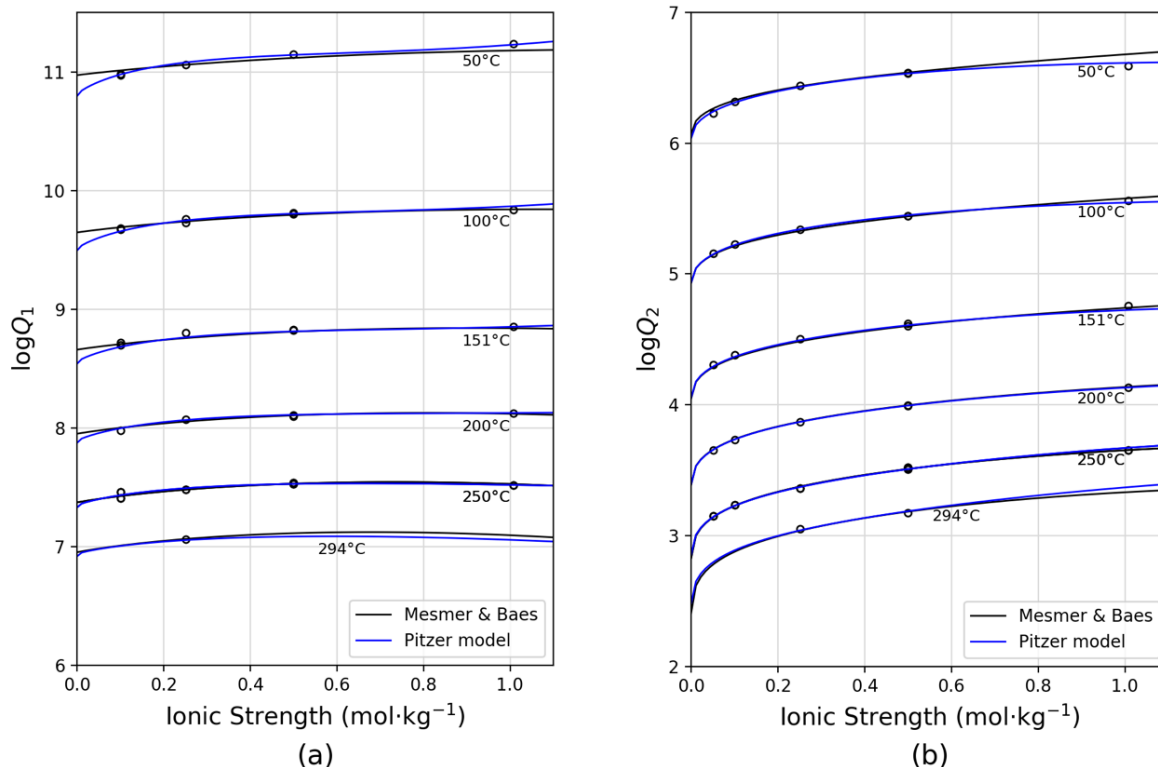
Figure 3.6: The dependence of $\log Q_1$ (a) and $\log Q_2$ (b) on ionic strength showing the experimental data and fit by Mesmer & Baes [71] and the use of the Pitzer parameters in Table 3.2 for hydrogen phosphate ions
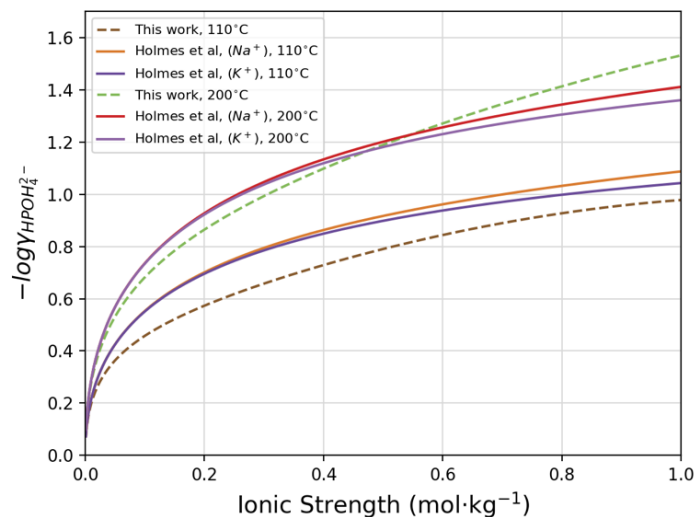
Figure 3.7: The dependence of the activity coefficient of HPO$_4^{2-}$ on ionic strength given by Holmes et al. [73] using the (HPO$_4^{2-}$, Na$^+$) and (HPO$_4^{2-}$, K$^+$) binary interactions, compared to the use of the Pitzer parameters in Table 3.2 for the generic (HPO$_4^{2-}$, M$^+$) interaction

3.7 Polyborate HKF Parameters

Equilibrium constant values for the polyborate formation reactions are determined by nonlinear least squares regression using the high boron concentration data (0.025-0.594 mol·kg^{-1}) of Mesmer et al. [24]. The HKF parameters reported in Table 3.1 provide a given equilibrium constant for Reaction 3.1, and the ion interactions are calculated using the Pitzer parameters given in Table 3.2. Best fit values for the equilibrium constants of Reactions 3.2-3.4 are determined at 50, 100, and 200 °C. Best fit HKF parameters are then determined for the three polyborate species, $B_2O(OH)_5^-$, $B_3O_3(OH)_4^-$, and $B_4O_5(OH)_4^-$, which are also reported in Table 3.1. The resulting equilibrium constants are plotted in Figure 3.8. The recommended value by Bassett [74] for the diborate $B_2O(OH)_5^-$ reaction at 25 °C is included. For the triborate $B_3O_3(OH)_4^-$ supplemental data is included from recent high temperature experiments [54, 75]. Sasidharanpillai et al. [54] measured the triborate formation constant up to 300 °C using Raman spectroscopy. In addition, Ferguson et al. [75] performed conductivity measurements up to 200 °C. Ferguson et al. [75] also reported values for the diborate species, which are not include in the fit due to the lack of agreement with the Mesmer et al. [24] data. The recommended value by Palmer et al. [48] for the tetraborate $B_4O_5(OH)_4^{2-}$ reaction at 25 °C is included. The HKF values in Table 3.1 provide a suitable fit to the available data that can be extrapolated up to the PWR CRUD temperature of 345 °C.

3.8 LiOH Association Constant

Ferguson et al. [76] report a density model for the association constant of LiOH intended to fit experimental data better at both low temperatures (T < 100 °C) and high temperatures (T > 250 °C, up to 410 °C). As shown in Figure 3.9, this model differs from other models, especially at low temperatures. Oddly, the change in entropy at 25 °C for this reaction appears to be large, as can be seen in the steep slope at that temperature in Figure 3.9. The MULTEQ thermodynamic software, developed by the Electrical Power Research Institute (EPRI), calculates a lower Gibbs of reaction at 25 °C, but a similar difference in entropy for the reaction at 25 °C. The equilibrium constant for this work is calculated using the HKF parameters for Li^+ by Shock and Helgeson (1988) [59], the parameters for LiOH by Shock et al. (1997) [66], and the selected parameters for OH^- reported in Table 3.1. The discrepancies from the various sources provide a notable uncertainty in the dissociation constant of LiOH. Nevertheless, because LiOH is a strong base
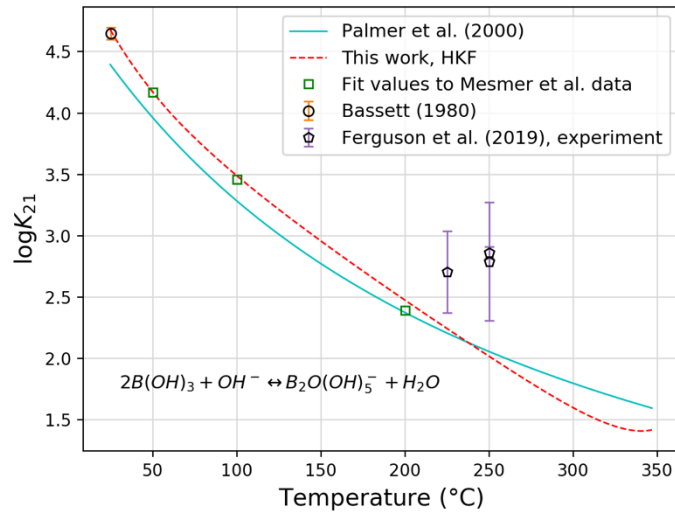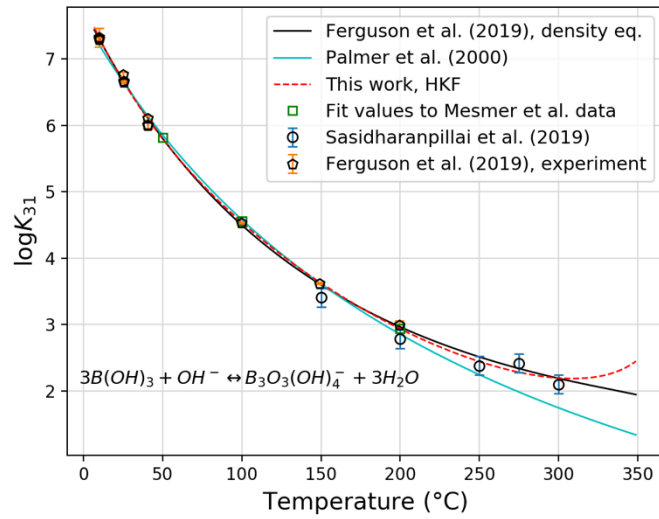
Figure 3.8: The equilibrium constants of the polyborate formation reactions (Reactions 3.2-3.4) as a function of temperature. The polyborate species are (a) the diborate $B_2O(OH)_5^-$, (b) the triborate $B_3O_3(OH)_4^-$, and (c) the tetraborate $B_4O_5(OH)_4^{2-}$

The graph shows $\log K_{41}$ on the y-axis (ranging from 0 to 12) versus Temperature (°C) on the x-axis (ranging from 50 to 350).

Legend:
- Palmer et al. (2000)
- This work, HKF
- Palmer et al. (2000)
- Fit values to Mesmer et al. data

$$4B(OH)_3 + 2OH^- \leftrightarrow B_4O_5(OH)_4^{2-} + 5H_2O$$

(c)

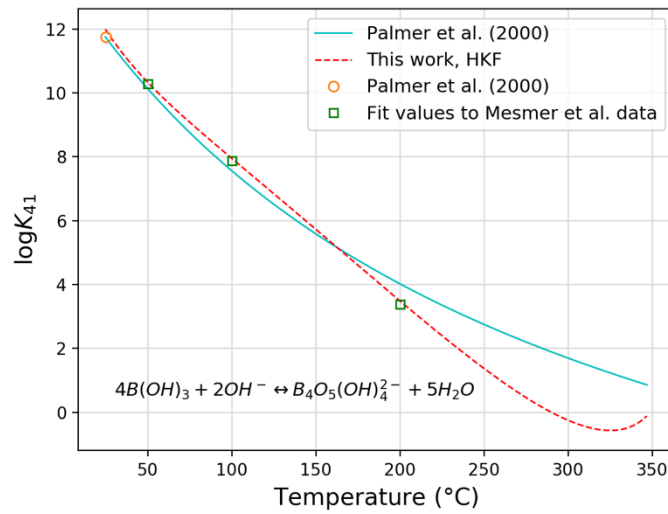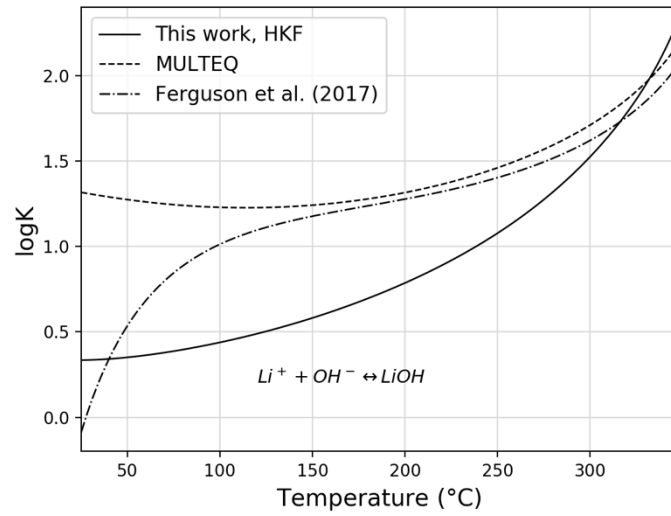**Figure 3.8 continued**: The equilibrium constants of the polyborate formation reactions (Reactions 3.2-3.4) as a function of temperature. The polyborate species are (a) the diborate $B_2O(OH)_5^-$, (b) the triborate $B_3O_3(OH)_4^-$, and (c) the tetraborate $B_4O_5(OH)_4^{2-}$

48

Figure 3.9: The equilibrium constant for the association reaction of lithium hydroxide from different sources

and has nearly total dissociation, this uncertainty has a negligible effect on the final calculated pH of solution and on the ionic strength.

3.9 Thermodynamic Data for Solids

Lithium borate solid precipitation is a likely cause of AOA, and therefore must be accurately predicted in CRUD modeling efforts. The Gibbs of formation for lithium metaborate ($LiBO_2$) and lithium tetraborate ($Li_2B_4O_7$) are plotted in Figure 3.10 from various sources. For both, the FactSage pubic database values agree with the NIST-JANAF table values [77] at 25 °C but predict more stable lithium borate solids at higher temperatures. A standard Gibbs of formation for $LiBO_2$ is calculated to be consistent with the equilibrium constant for Reaction 3.17 reported by Byers et al. [20] and the calculated standard Gibbs of formation for the other species using the selected HKF parameters from Table 3.1. This Gibbs agrees fairly well with the FactSage public database, with some disparity at the saturation temperature. The Gibbs of formation for $Li_2B_4O_7$ is also calculated using the equilibrium constant for Reaction 3.18 from MULTEQ. The MULTEQ equilibrium constant predicts $Li_2B_4O_7$ to be more stable than the other sources.

$$LiBO_2(s) + H_2O + H^+ \rightleftarrows Li^+ + B(OH)_3 \qquad (3.17)$$
$$Li_2B_4O_7(s) + 4H_2O + 2H^+ \rightleftarrows 2Li^+ + 4B(OH)_3 \qquad (3.18)$$
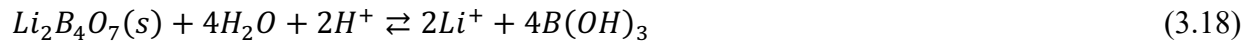
3.10 Equilibrium Calculations

Boron speciation depends largely on pH, total boron concentration, and temperature. At low pH, $B(OH)_3$ is the dominant species, shown in Figure 3.11. Increases in the pH are caused by adding more lithium to the solution, yielding an increase in the concentration of the borate ion $B(OH)_4^-$ to balance the charge of the Li^+ cations. Polyborate species tend to reach a peak concentration at elevated pH, and the location of the peak depends on the species, the total boron concentration, and the temperature. At 25 °C, the triborate $B_3O_3(OH)_4^-$ is the dominant polyborate, as noted by Graff et al. [79]. Differing from the results by Graff et al. [79], the model presented in this work calculates a higher peak concentration of the tetraborate species $B_4O_5(OH)_4^{2-}$ at 25 °C. Under typical PWR conditions with a pH of about 7.0, a startup boron concentration of about 0.1 mol·kg^{-1}, and a hot leg temperature of about 290 °C, the primary species present is $B(OH)_3$ with little $B(OH)_4^-$ and virtually no polyborates. At likely CRUD
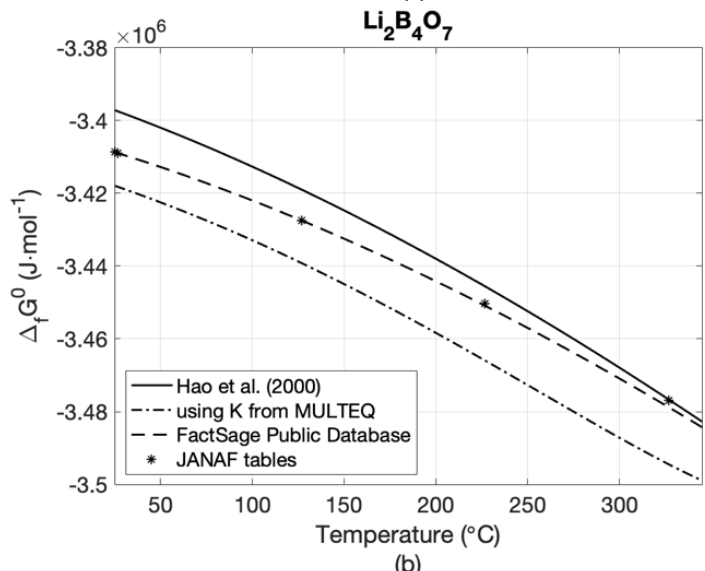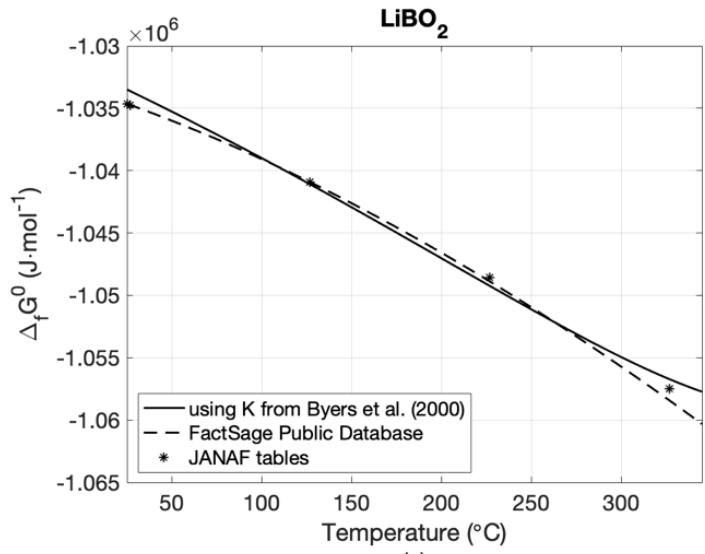
Figure 3.10: Standard Gibbs of formation for (a) lithium metaborate ($LiBO_2$) and (b) lithium tetraborate ($Li_2B_4O_7$), as obtained from various sources [20, 77, 78].
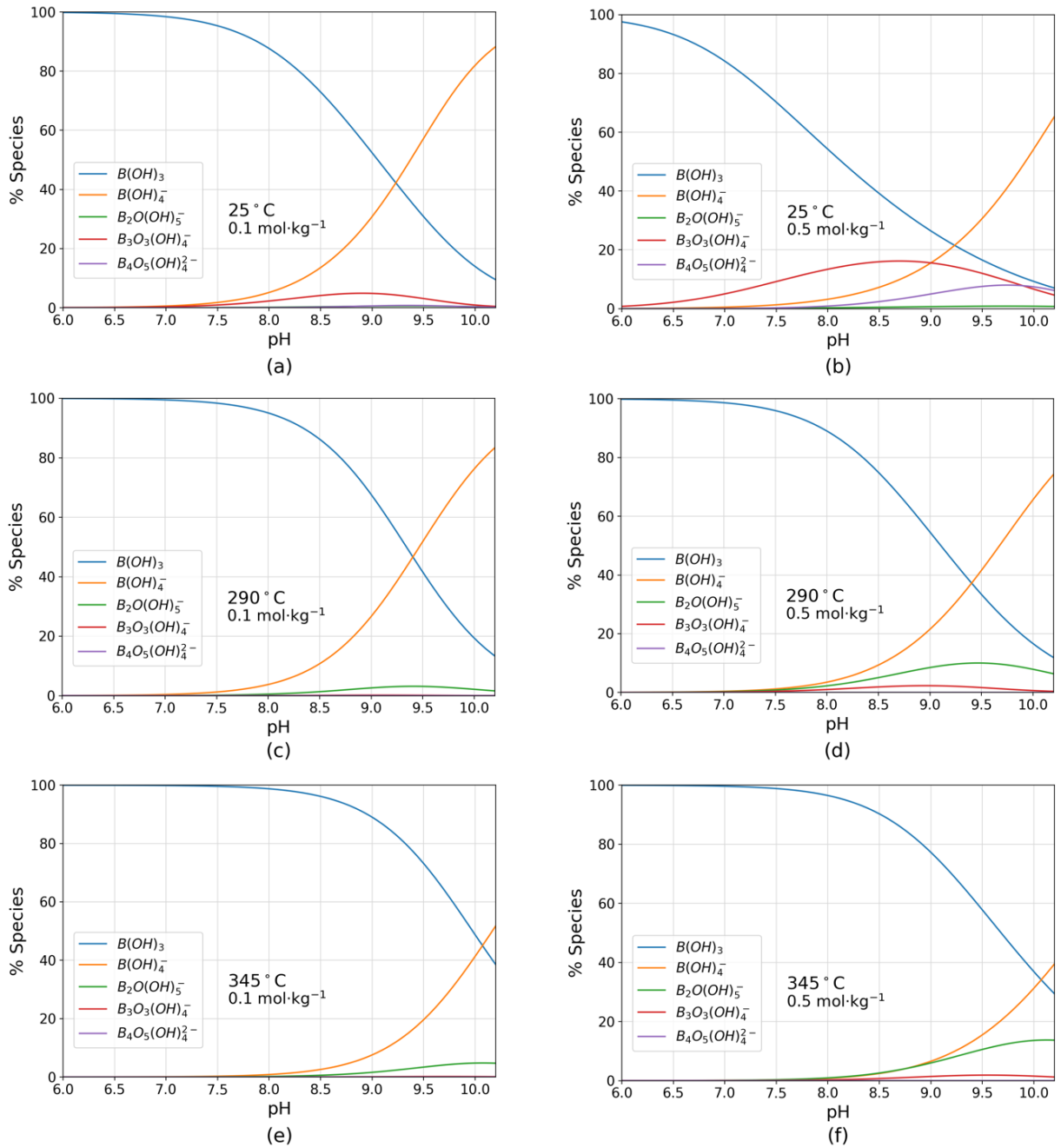
Figure 3.11: Boron speciation as a function of pH calculated at 25 °C (a & b), 290 °C (PWR hot leg coolant temperature) (c & d), and 345 °C (PWR CRUD internal temperature) (e & f), and at total boron concentrations of 0.1 mol·kg⁻¹ (typical bulk coolant concentration at reactor startup) (a, c, & e) and 0.5 mol·kg⁻¹ (likely CRUD internal concentration) (b, d, & f)

conditions of 345 °C and an elevated boron concentration of 0.5 mol·kg^{-1}, the diborate $B_2O(OH)_5^-$ is the significant polyborate species.

Equilibrium calculations were performed at 155 bar and 345 °C to determine the phase diagrams of solid precipitates as a function of the concentrations of elements in the aqueous phase. Lithium tetraborate ($Li_2B_4O_7$) precipitates at elevated pH (greater than 7.0) and when the concentration of boron is sufficiently high (greater than 0.7 mol·kg^{-1}). Boron and lithium can become concentrated within CRUD, crossing into the $Li_2B_4O_7$ stability region shown in Figure 3.12. Lithium metaborate ($LiBO_2$) precipitates at even greater pH, above 8.75, which is unlikely to occur in CRUD before lithium tetraborate precipitation occurs. The high boron concentration of lithium tetraborate ($Li_2B_4O_7$) precipitates within the CRUD are a likely cause of AOA. It should be noted that as boron and lithium coolant concentrations drop late in the reactor cycle [14] the conditions within the CRUD will exit the $Li_2B_4O_7$ stability region, causing the compound to reenter solution.

When performing similar calculations using KOH and NaOH instead of LiOH, it is found that no solids form within the concentration range likely to occur in CRUD. Concentrations of boric acid must exceed 7.3 mol kg^{-1} for solid metaborate (HBO_2) to precipitate. Such extreme concentrations are not currently predicted to occur in MAMBA simulations.

3.11 Conclusions

A detailed thermodynamic description of the H_2O-B-Li system relevant to CRUD is implemented with the HKF and Pitzer equations to describe the aqueous phases using the CALPHAD method. The solid phases are modeled as pure compounds. Included in the aqueous model are new HKF parameters for OH^-, $B(OH)_4^-$, $B_2O(OH)_5^-$, $B_3O_3(OH)_4^-$, and $B_4O_5(OH)_2^{-2}$ that can be used to describe the thermodynamics and phase equilibria in a PWR up to the saturation temperature. Pitzer parameters for the binary interaction between various borate anions with alkali metal cations are provided to describe the solution behavior with ionic strengths up to 1.0 mol·kg^{-1}.

Calculations using the models developed in this work indicate that lithium tetraborate ($Li_2B_4O_7$) precipitation occurs when boric acid concentrations are high and when pH is elevated. Lithium metaborate ($LiBO_2$) precipitation is only possible at extremely elevated pH values. Because boron and lithium become concentrated within CRUD, lithium tetraborate precipitation
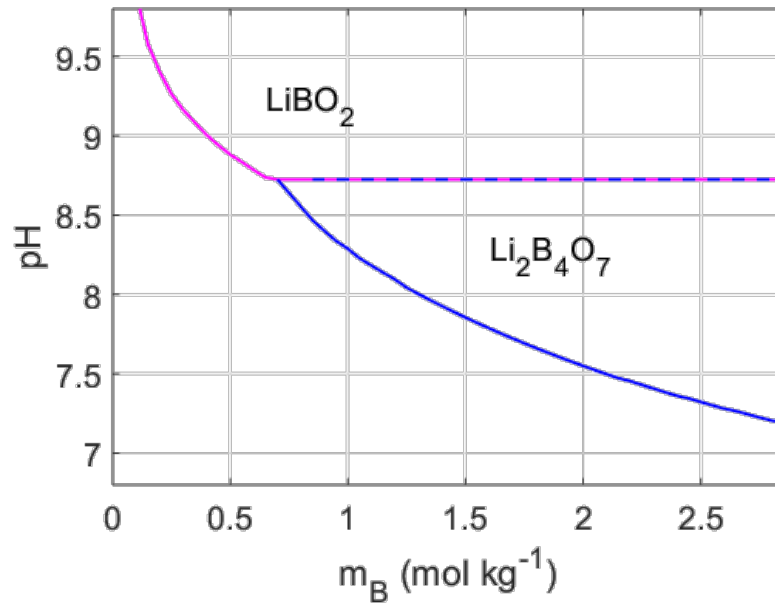
Figure 3.12: Phase diagram showing the stability regions of solid precipitates under PWR conditions

is predicted to occur, causing Axial Offset Anomaly (AOA). KOH should be investigated as an alternative to LiOH as an additive in PWRs due to the lack of potassium borate salt precipitation in CRUD.

CHAPTER 4. NICKEL AND IRON THERMOCHEMISTRY IN PWRS

4.1 Introduction

Aqueous nickel and iron enter PWR coolant by the dissolution of Cr-rich oxide and nickel ferrite spinel present on Alloy 600 and 690 steam generator tube surfaces [10]. The concentration of aqueous Fe tends to be about double that of aqueous Ni [12], corresponding to solution equilibrium with $NiFe_2O_4$. The Ni concentration is roughly estimated to be about $4.3 \cdot 10^{-9}$ mol·kg^{-1} (0.25 ppb) in the bulk coolant, and about $5.6 \cdot 10^{-8}$ mol·kg^{-1} (3.3 ppb) in the CRUD. This aqeuous nickel and iron cause precipitation reactions within the CRUD forming whatever phase is thermodynamically stable. Aqueous boron and lithium concentrations determine the stability of the phases. Therefore, the regions of stability of the phases that form CRUD based on boron and lithium concentration are calculated to inform the modeling of these precipitation reactions.

4.2 Nickel and Iron Speciation

Nickel metal oxidizes to form nickel oxide along Inconel surfaces according to the reaction:

$$Ni(s) + H_2O \leftrightarrows NiO(s) + H_2(g) \tag{4.1}$$

Nickel oxide dissolves forming Ni^{2+} ions according to:

$$NiO(s) + 2H^+ \leftrightarrows Ni^{2+} + H_2O \tag{4.2}$$

The Ni^{2+} ion forms species $Ni(OH)_x^{2-x}$, given by:

$$Ni^{2+} + OH^- \leftrightarrows Ni(OH)^+ \tag{4.3}$$

$$Ni^{2+} + 2OH^- \leftrightarrows Ni(OH)_2^0 \tag{4.4}$$

$$Ni^{2+} + 3OH^- \leftrightarrows Ni(OH)_3^- \tag{4.5}$$

Likewise for iron oxide compounds, magnetite (Fe_3O_4) dissolves forming Fe^{2+} ions according to:

$$\frac{1}{3}Fe_3O_4(s) + 2H^+ + \frac{1}{3}H_2(g) \leftrightarrows Fe^{2+} + \frac{4}{3}H_2O \tag{4.6}$$
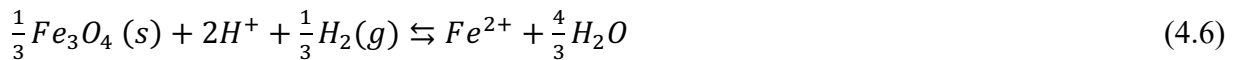
The Fe^{2+} ion forms species $Fe(OH)_x^{2-x}$, given by:

$$Fe^{2+} + OH^- \leftrightarrows Fe(OH)^+ \tag{4.7}$$

$$Fe^{2+} + 2OH^- \leftrightarrows Fe(OH)_2^0 \tag{4.8}$$

$$Fe^{2+} + 3OH^- \leftrightarrows Fe(OH)_3^- \tag{4.9}$$

Tremaine and LeBlanc [80] performed high temperature NiO solubility experiments. Likewise, Sweeton and Baes [81] performed high temperature Fe_3O_4 solubility experiments. In these experiments, an aqueous solution is prepared at a given pH at 25 °C (298.15 K) and is then heated to given temperature. The solution then flows through a bed of oxide particles until equilibrium is achieved, and the amount of dissolved nickel or iron is measured. Dickenson et al. [49] report thermodynamic parameters of each species involved to model this solubility data.

HKF parameters for Ni^{2+} and Fe^{2+} were calculated by Shock and Helgeson [59], and HKF parameters for $Ni(OH)^+$ and $Fe(OH)^+$ were calculated by Shock et al. [66]. These parameters are utilized in the SUPCRT92 database [57] for aqueous thermochemistry, which does not include the second and third hydroxide products given by Reactions 4.4, 4.5, 4.8, and 4.9 that are important at higher pH.

4.3 Aqueous Thermochemistry

The HKF parameters for the series of species $Ni(OH)_x^{2-x}$ and $Fe(OH)_x^{2-x}$ were calculated by nonlinear least squares regression using the solubility data of NiO solubility from Tremaine and LeBlanc [80] and Fe_3O_4 solubility data from Sweeton and Baes [81]. The enthalpy of formation ($\Delta_f H^0$) and entropy (S^0) of the species at 25°C from Dickinson et al. [49] are maintained. The HKF parameters for Ni^{2+} and Fe^{2+} are also maintained from the SUPCRT92 database [57]. The resulting HKF parameters are listed in Table 4.1 and the goodness of fit is compared to that from the expressions by Dickinson et al. [49] in Table 4.2. The newly obtained HKF parameters provide an improved fit for the NiO solubility data and an equivalent fit for the Fe_3O_4 data as that of Dickinson et al. [49].

The solubility data covers a range of temperatures up to 300 °C (573 K). The maximum temperature data is shown in Figure 4.1 and compared to calculations using the Dickinson et al. [49] and the HKF parameters in Table 4.1. The solubility reaches a minimum at moderately high pH values, which at 300 °C correspond to 7.5 for NiO and 6.7 for Fe_3O_4. Ni^{2+} and Fe^{2+} are the dominant species at low pH, as shown in Figure 4.2. As pH increases, the dominant species steps through the greater hydroxide species. The neutral $Ni(OH)_2$ and $Fe(OH)_2$ species are the predominant species under PWR coolant conditions.

Table 4.1: Standard Partial Molar Thermodynamic Data and Revised HKF EOS Parameters for Ni/Fe Aqueous Species

Species	$\Delta_f H^0$ (J mol^{-1})	S^0 (J mol^{-1} K^{-1})	c_1 (J mol^{-1} K^{-1})	c_2 (J K mol^{-1})	ω (J mol^{-1})
Ni^{2+}	-53974[a]	-128.87[a]	55.19[a]	-226685[a]	630403[a]
$Ni(OH)^+$	-270577[b]	-55.26[b]	57.60	-476969	-116931
$Ni(OH)_2$	-534605[b]	-73.08[b]	177.43	-704310	-18747
$Ni(OH)_3^-$	-767556[b]	-55.36[b]	-34.59	2318991	187621
Fe^{2+}	-92257[a]	-105.86[a]	61.86[a]	-194292[a]	601743[a]
$Fe(OH)^+$	-323240[b]	-30.17[b]	270.15	-2730161	147246
$Fe(OH)_2$	-540520[b]	54.90[b]	-19.66	488519	-230959
$Fe(OH)_3^-$	-773880[b]	102.00[b]	6.75	-39317	36488

[a] Shock and Helgeson [59] [b] Dickinson, et al. [49]

Table 4.2: Fit Error for NiO and Fe₃O₄ Solubility Data

Oxide	Data Source	Parameter Source	RSS Error
NiO	Tremaine and LeBlanc [80]	Dickinson et al. [49]	0.184
		HKF params in Table 4.1	0.165
Fe₃O₄	Sweeton and Baes [81]	Dickinson et al. [49]	2.80×10^{-5}
		HKF params in Table 4.1	2.80×10^{-5}
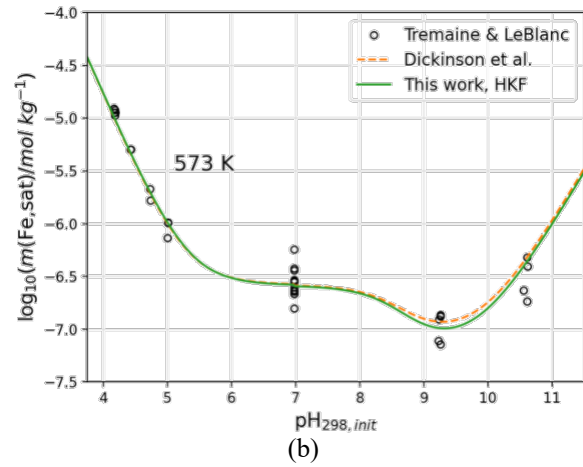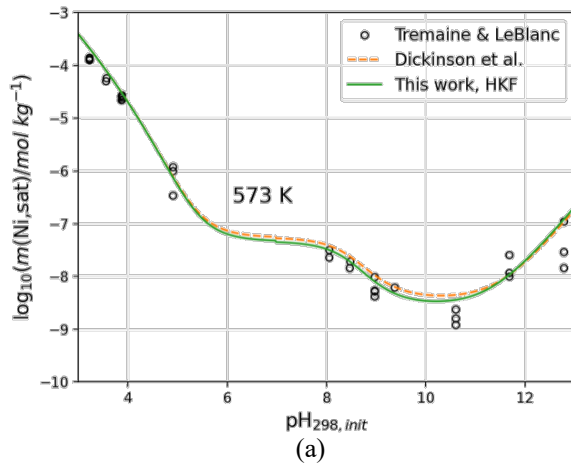
Figure 4.1: Equilibrium calculated and experimental total dissolved (a) Ni at 25 °C (298 K) and (b) Fe at 25 °C (298 K) as a function of initial solution pH
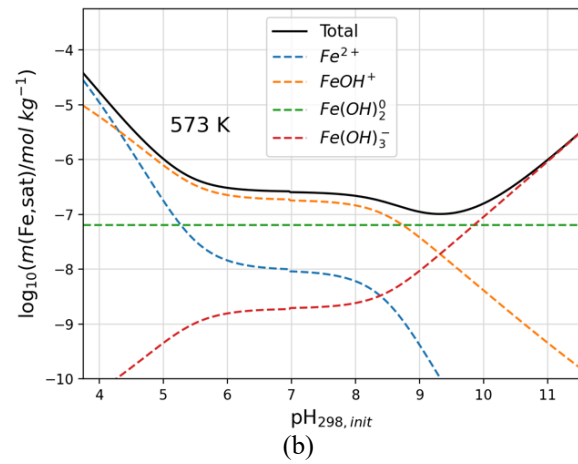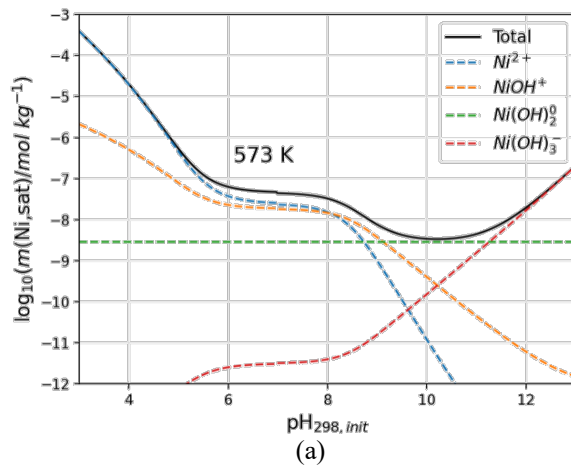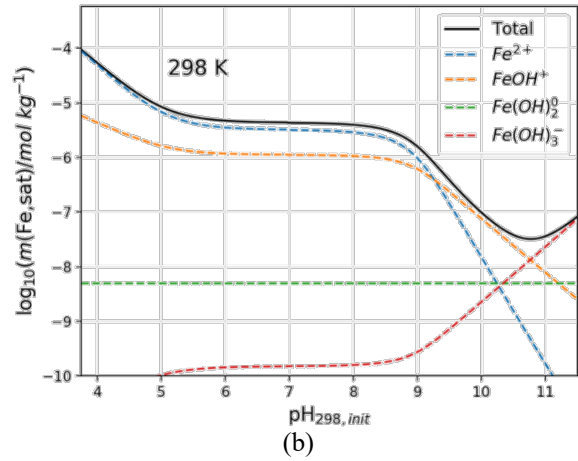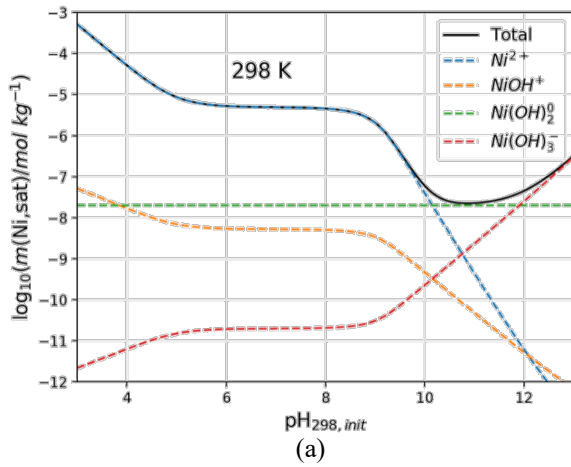
Figure 4.2: Equilibrium calculated speciation of aqueous (a) Ni at 25 °C (298 K), (b) Fe at 25 °C (298 K), (c) Ni at 300 °C (573 K), and (d) Fe at 300 °C (573 K), as a function of initial solution pH

As expected, the slope of the logarithmic concentrations of each species in Figure 4.2 is determined by the ionic charge. Positively charged ions decrease in concentration with pH, and negatively charged ions increase in concentration with pH. The concentrations of neutral species are constant with pH. The influence of the hydroxide reactions increases with temperature as well, with less Ni^{2+} and Fe^{2+} and more hydroxide product concentration at higher temperatures.

4.4 Estimating Thermophysical Properties for Unknown Solids

Two competing mechanisms for boron retention are the formation of bonaccordite (Ni_2FeBO_5) and the incorporation of boron defects in nickel ferrite ($NiFe_2O_4$) crystals. The formation energies of both of these complexes have not been measured experimentally. Therefore, reported density functional theory (DFT) results [29-31] paired with entropy and heat capacity estimation techniques [32, 82] are utilized. The enthalpy of formation for bonaccordite was calculated using DFT by Rák et al. [31]. The crystal structure of bonaccordite is shown in Figure 4.3. The heat capacity of bonaccordite was estimated by D. Shin [82] using the Neumann-Kopp Additivity Rule is applied to binary oxides, shown by Equation 4.11. D. Shin [82] also estimated the entropy of bonaccordite using the Latimer approach, as:

$$C_P(Ni_2FeBO_5) = 2C_P(NiO) + 0.5C_P(Fe_2O_3) + 0.5C_P(B_2O_3) \tag{4.11}$$

Zs. Rák et al. [29, 30] assessed the possibility of forming boron defects in nickel ferrite spinel as a mechanism for boron retention in the CRUD. Using DFT, Rak and co-authors calculated that a boron defect is favored in a tetrahedral interstitial site with two cation nearest neighbors, denoted by B_{T2} in Figure 4.4. The enthalpy of formation at 298.15 K of the boron interstitial is given by

$$\Delta H_f^0(B_T^q) = \Delta E(B_T^q) - \mu_B^0 + qE_F \tag{4.12}$$

where $\Delta E(B_T^q)$ is the difference in the total energies calculated by DFT of the defect-containing and the defect-free solids, q is the charge state of the boron interstitial, and E_F is the Fermi energy referenced to the energy of the valence band maximum. The reference chemical potential of boron, μ_B^0, in the calculations is reported to be -6.20 eV. Given $\Delta E(B_T^q)$ = -3.48 eV, and assuming a charge neutral defect ($q=0$), $\Delta H_f^0(B_T^q)$ = 2.72 eV/f.u. = 262.4 kJ/mol. The heat capacity of the defected nickel ferrite is estimated using the Neumann-Kopp Additivity Rule, and the entropy is estimated by the Latimer approach [32]. Using these thermophysical properties,
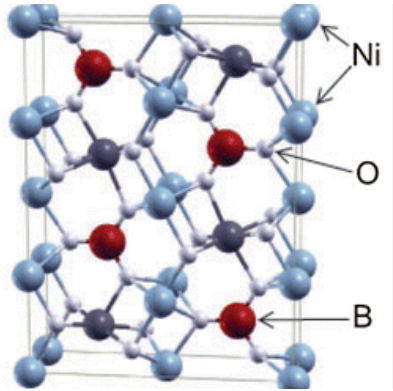
Figure 4.3: Ludwigite crystal structure of bonaccordite (Reproduced from [31])
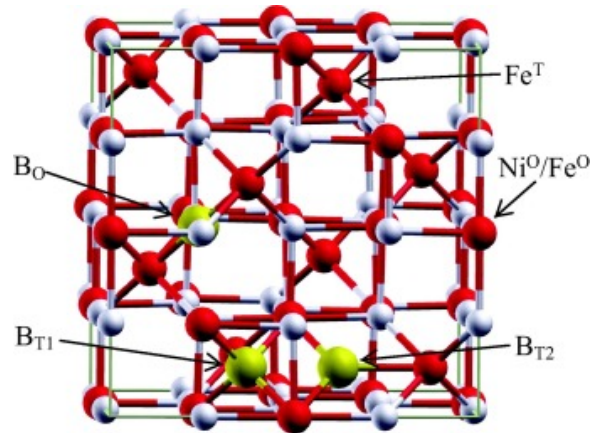
Figure 4.4: Nickel ferrite unit cell with interstitial sites occupied by B, tetrahedral cation sites, and octahedral cation sites. (Reproduced from [29])

the compound energy formalism [33] is utilized in FactSage to model the solution of pure $NiFe_2O_4$ with defected $NiFe_2O_4$, where the interstitial location is either a B or a vacancy (Va).

Nickel and iron containing solids make up the majority of CRUD. Figure 4.5 plots the Gibbs energy of formation for various Ni-Fe-containing solids as calculated using various sources [2, 83]. In particular, Figure 4.5a plots the Gibbs energy for elemental Ni, while Figure 4.5b plots that of NiO. Figures 4.5c and 4.5d plot the Gibbs energy of the iron oxide phases Fe_2O_3 and Fe_3O_4, respectively, in which each of the thermodynamic sources [2, 57, 77, 83] provide a consistent prediction of the monotonic decrease in Gibbs energy with increasing temperature. Figure 4.5e plots the Gibbs energy for the nickel ferrite spinel, for which the lower EPRI [2] values are selected over those of O'brien et al. [83]. While some discrepancies exisit for these solids, the differences are found to not significantly affect whether or not the solids could precipitate under typical CRUD conditions predicted by MAMBA.

Figure 4.6 shows the estimated Gibbs energy of formation for bonaccordite (Ni_2FeBO_5) estimated by Shin [82] based on calculations by Rák et al. [31]. The value used in this study is slighly higher, leading to slighly less favorable bonaccordite formation, which is dicussed in relation to Figures 4.8 and 4.9.

As expected, Figure 4.7 indicates that incorporation of a boron defect raises the Gibbs free energy relative to pure nickel ferrite. As well, for the temperature range from 300 to 1000 K, a comparison of Figures 4.6 and 4.7 indicates that the Gibbs free energy of formation for bonaccordite is more negative (energetically favored) relative to nickel ferrite. The shapes of the two curves in Figure 4.6 and 4.7 are nearly identical, showing that the entropy and heat capacity contributions of the B interstitial are estimated to be minor, while the enthalpy contribution is more significant.

4.5 Equilibrium Precipitation Calculations

Equilibrium calculations are performed at the saturation temperature to determine the phase diagram of Ni-Fe-containing solid precipitates within CRUD, and the results are plotted in Figure 4.8. Ni metal is dominant at elevated pH (above 7.0). Nickel ferrite ($NiFe_2O_4$) is the dominant phase at low pH and sufficiently low boron concentration. Formation of Ni_2FeBO_5 requires a sufficiently high concentration of B of 0.15 mol·kg^{-1} (1620 ppm). Stability of $NiFe_2O_4$ is greater at lower pH and at a greater concentration ratio of Fe/Ni. When nickel ferrite
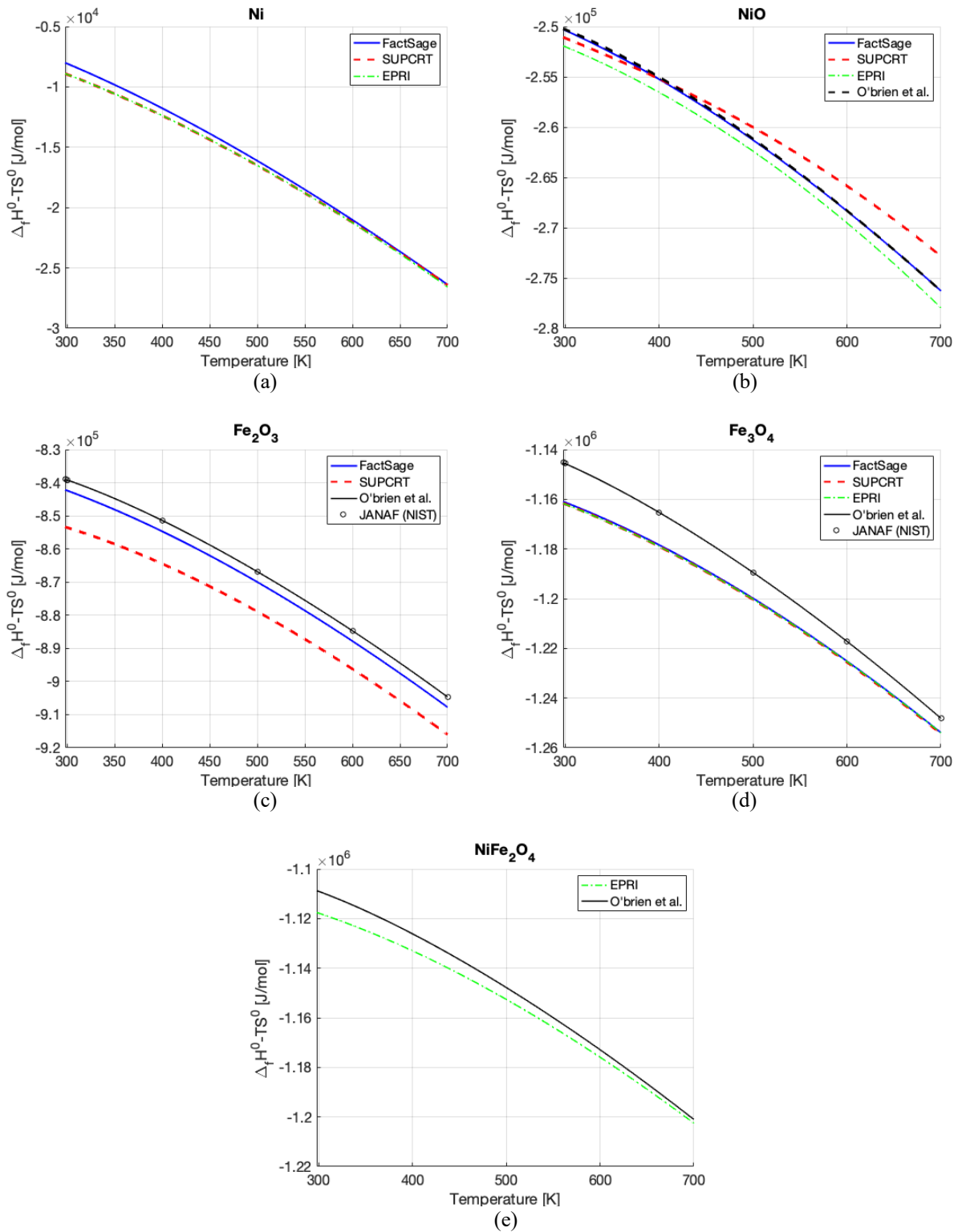
Figure 4.5: Standard partial molar Gibbs energy of formation for Ni and Fe containing solids from various sources [12, 57, 77, 83]
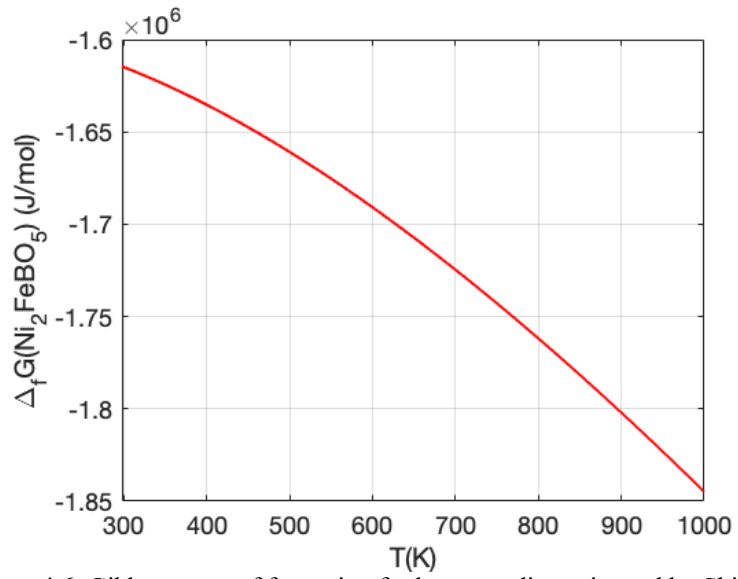
Figure 4.6: Gibbs energy of formation for bonaccordite estimated by Shin [82] based on calculations by Rák et al. [31]
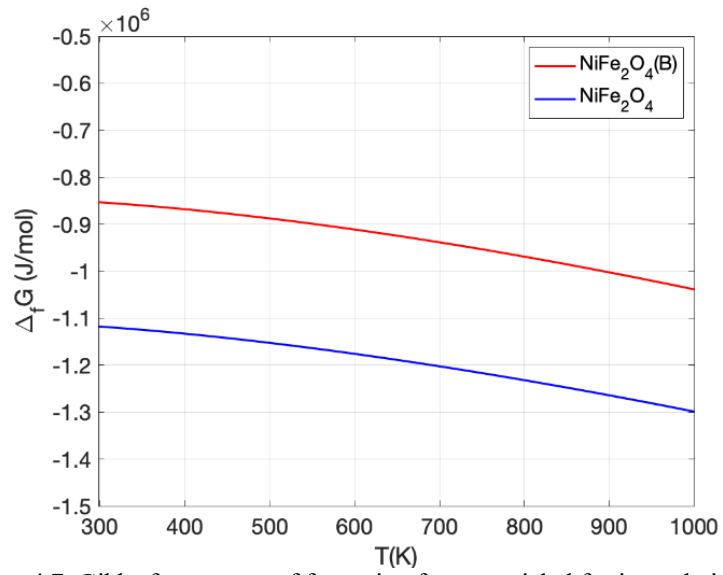
Figure 4.7: Gibbs free energy of formation for pure nickel ferrite and nickel ferrite with a tetrahedrally coordinated boron interstitial
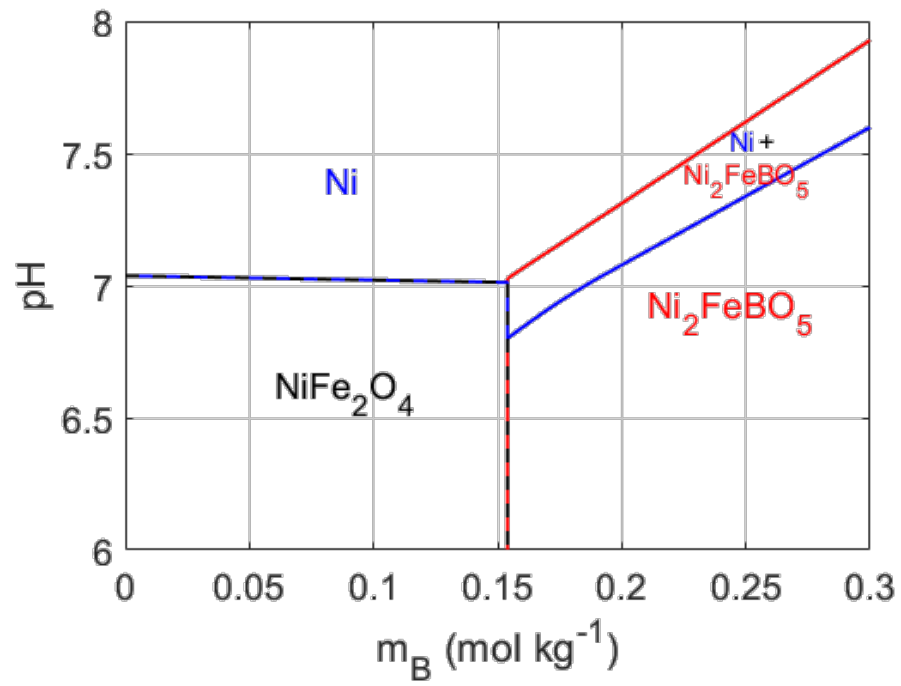
Figure 4.8: Ni-Fe-containing solid phase diagram at the saturation temperature 345°C to describe CRUD composition

precipitates, the fraction of interstitial sites predicted to contain B is always insignificant. As pH increases, the stability of either Ni or NiO increases, and the stability of Ni_2FeBO_5 increases. If the pH is less than 8.02 the formation of magnetite (Fe_3O_4) is possible at very high concentrations soluble Fe, 15 times greater than the soluble Ni concentration, which is unlikely to occur.

The stability of Ni metal versus NiO depends on temperature and the amount of dissolved hydrogen, which limits the aqueous oxygen content present in the coolant. A Hydrogen water chemistry (HWC) program is used in most operating pressurized water reactors to decrease the concentration of radiolytic oxygen dissolved in the coolant, and as such, it is assumed that 32 cm^3(STP)kg^{-1} of dissolved H_2 is present. At the saturation temperature of 345 ºC, the Ni/NiO transition occurs at a dissolved H_2 concentration of 17.1 cm^3(STP)kg^{-1}, based on the results by Attanasio and Morton [84]. As a result, Ni metal is more stable than NiO. However, after shutdown and during characterization, the Ni metal in the CRUD is likely oxidized. An oxygen concentration of 5.0 X 10^{-5} (mol O_2)(kg H_2O)$^{-1}$ is required for oxidation of Ni to form NiO. This result explains why CRUD sometimes contains NiO instead of Ni metal at the time of characterization [4, 5].

The phase diagram in Figure 4.8 shows a strong sensitivity on the formation energy of bonaccordite. The selected value of $\Delta \overline{H_f^0}(Ni_2FeBO_5)$ is 1% greater than that estimated by Rák et al. [31], but well within the range of uncertainty for DTF predicted values, because it provides calculations that are more representative of the actual chemistry observed from plants. Without this adjustment, the stability of Ni_2FeBO_5 is overpredicted, as demonstrated by the phase diagram depicted by Figure 4.9 where the expansive stability region of Ni_2FeBO_5 in CRUD reaches the extremely low boron concentration of 0.0078 mol·kg^{-1} (84 ppm).

Figure 4.10 provides a phase diagram over the same range of boron concentration and pH as Figure 4.8, delineating the stability of nickel metal versus nickel ferrite, and indicates that nickel metal is stable at the hot leg bulk coolant temperature of 328 °C and pH greater than 6.75, supporting the observation of nickel metal particulates in the coolant [5]. Nickel ferrite is stable in bulk coolant if the pH drops below 6.75. Boron concentrations in the coolant cannot reach the extremely large value of 0.34 mol·kg^{-1} (3675 ppm) required for bonaccordite to be stable.

Figure 4.9: Ni-Fe-containing solid phase diagram at the saturation temperature 345°C to describe CRUD composition using the lowest value of $\Delta\overline{H_f^0}(Ni_2FeBO_5)$ [31], showing an impossibly large Ni₂FeBO₅ stability region

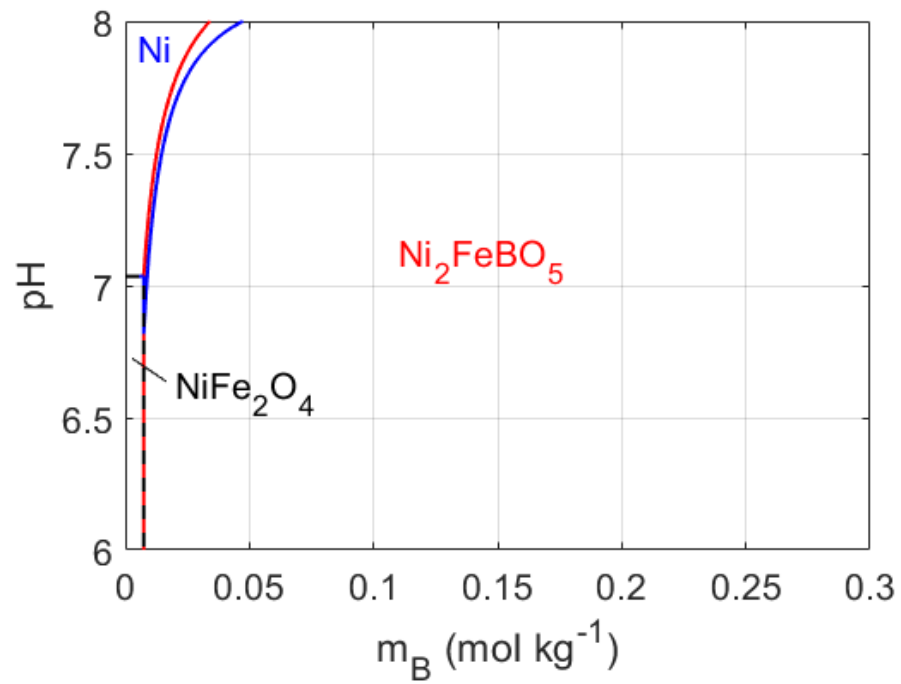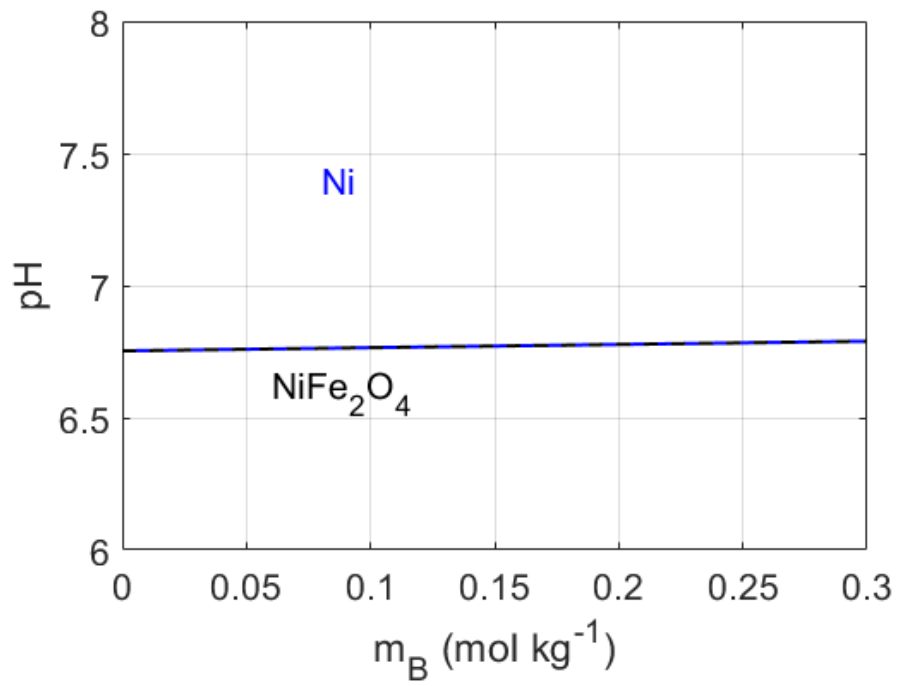**Figure 4.10**: Ni-Fe-containing solid phase diagram at the hot leg temperature of 328°C

These equilibrium calculations, coupled with the plant CRUD scrape observations presented in Chapter 1 [4, 5, 17, 18, 21], indicate a plausible scenario to describe CRUD formation. Figure 4.9 shows that nickel metal is stable in the coolant at typical PWR pH values in the range of 6.9 to 7.4, and nickel ferrite ($NiFe_2O_4$) is stable if the pH drops below 6.75. Therefore, nickel metal and/or nickel ferrite particles circulating in the coolant deposit on fuel rod surfaces growing CRUD. Once CRUD sustains internal boiling, it sustains the saturation temperature of 345 °C and concentrates soluble boron. Nickel metal in the CRUD reacts with aqueous Fe to form nickel ferrite if the pH is 7.0 or less. If the boron concentration exceeds 0.15 mol·kg^{-1} (1620 ppm) the nickel ferrite reacts with aqueous B and Ni to form bonaccordite (Ni_2FeBO_5).

CHAPTER 5. CALIBRATION OF THE KINETIC RATES

5.1 Simulation Setup

While thermodynamics describes which species should be present and which reactions should occur, the kinetic rates of these reactions require calibration using the chemical analysis of CRUD samples taken from spent fuel. Importantly, the chemistry of these samples is altered during reactor shutdown, which must be considered. As an example, solid lithium tetraborate is thought to dissolve out of the CRUD during shutdown [14] due to its retrograde solubility combined with the loss of the internal boiling that drives the saturation of soluble B and Li within the CRUD. Ni metal might also transform to NiO during shutdown and fuel storage due to oxygen exposure.

MAMBA is used to simulate the morphology of CRUD through the end-of-cycle, using the power history and the coolant chemistry of three different plant cycles, Callaway Cycle 9 [4], Callaway Cycle 10, and Seabrook Cycle 5 [5]. Figures 5.1-5.3 show the power level, AO, and coolant concentrations of boron and lithium for these three plant cycles. While the power histories of Seabrook Cycle 5 and Callaway Cycle 10 are mostly constant, the severe AOA of -14% at Callaway Cycle 9 caused a power downrating of 70% as shown in Figure 5.1. The Callaway plant operated with a pH at about 7.0, reaching a target maximum of 7.1 mid-cycle and a minimum of 6.9 by end-cycle. The Seabrook plant begins at a pH of about 7.0 and reaches a higher maximum pH of 7.4 by keeping lithium concentration constant for the majority of cycle as boron decreases. During Callaway Cycle 9, the sudden downrating of power caused the measured lithium concentrations to experience a relatively short duration spike around 300 days into the cycle. Callaway Cycle 10 experienced AOA that was believed to be residual associated with boron in CRUD deposits from Cycle 9, as the AOA at the start of Cycle 10 was -7% but reduced in magnitude as Cycle 10 progressed. As a result, the initial plant soluble boron concentration was decreased by about 200 ppm to compensate for the anticipated loss of reactivity. Typical coolant temperature boundary conditions are utilized in all plant sample simulations, given an average coolant temperature of 308.5°C. A typical PWR hydrogen water chemistry and default nickel/iron particulate and soluble concentrations are assumed. The hydrogen values are 40 cm^3(STP)kg^{-1} for the Callaway cycles and 32 cm^3(STP)kg^{-1} for Seabrook. At these conditions, Ni metal is stable over NiO, however for more oxidizing

74

(a)

(b)
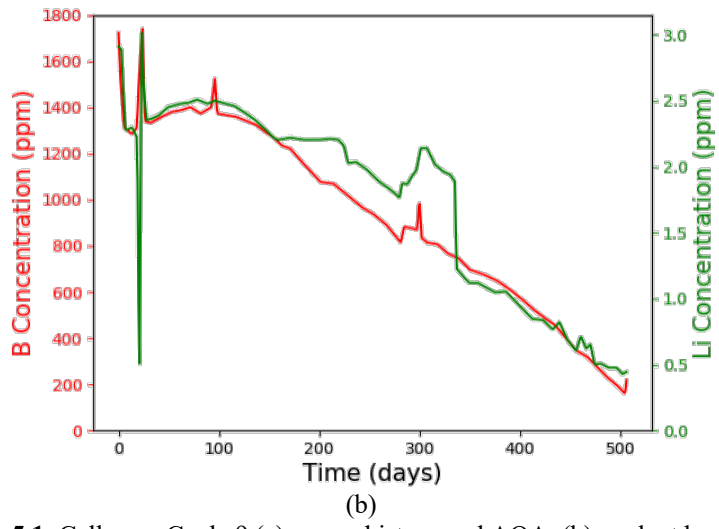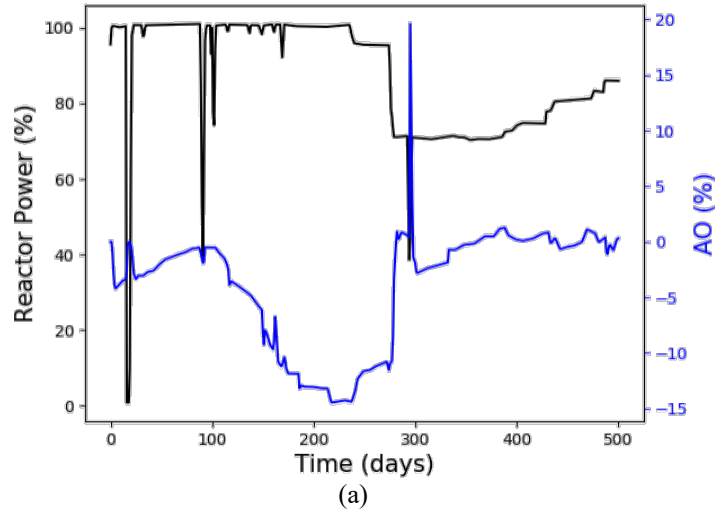
Figure 5.1: Callaway Cycle 9 (a) power history and AOA, (b) coolant boron and lithium concentration
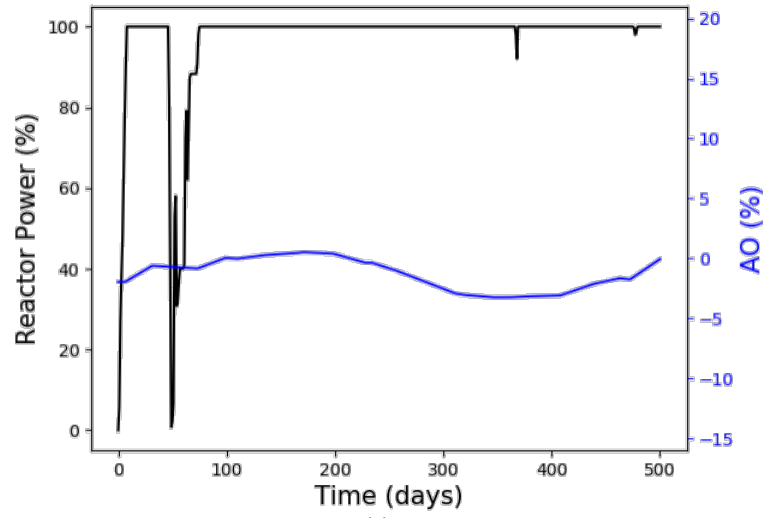
(a)
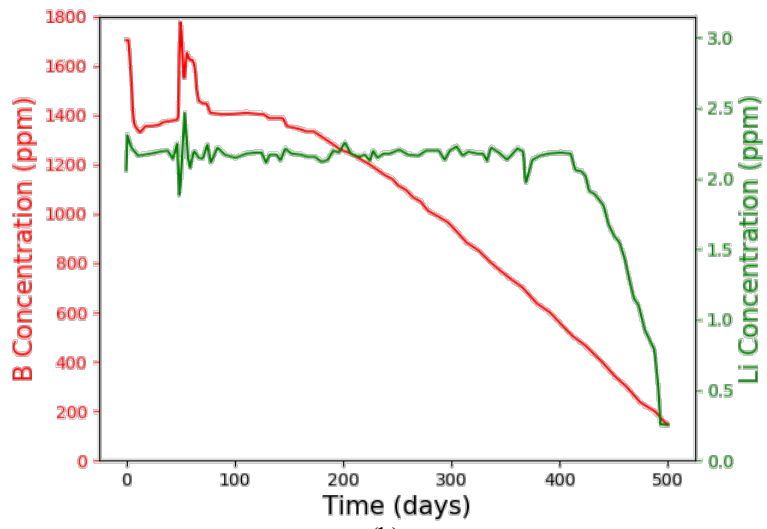
(b)

Figure 5.2: Seabrook Cycle 5 (a) power history and AOA, (b) coolant boron and lithium concentration
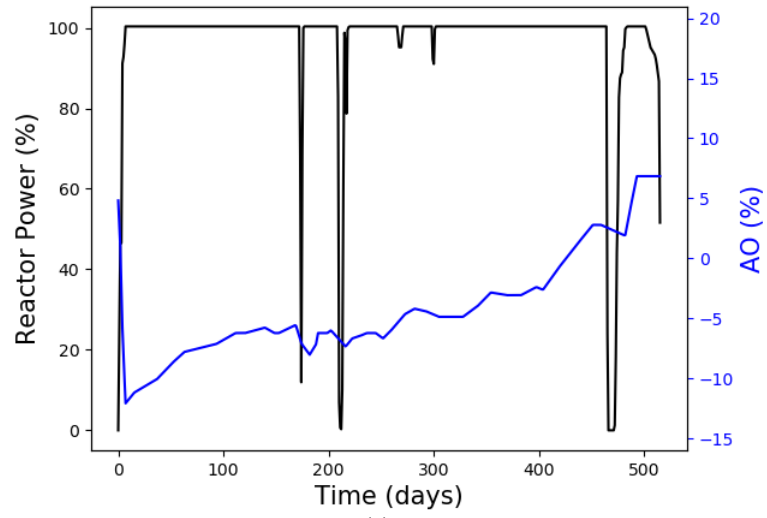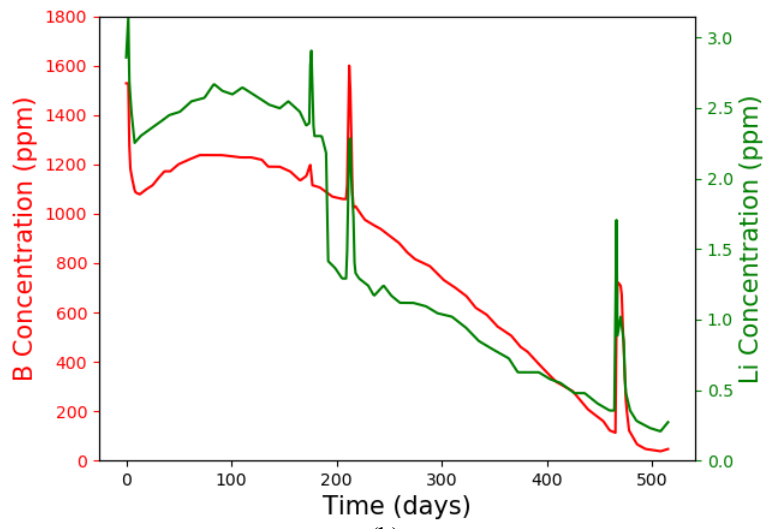
Figure 5.3: Callaway Cycle 10 (a) power history and AOA, (b) coolant boron and lithium concentration

conditions NiO would be preferred. The effects of shutdown and CRUD burst have not been modeled. The kinetics of the chemical reactions are calibrated using a Bayesian estimation algorithm to best match the chemical makeup of the CRUD samples that were analyzed.

The model assumes ~nm size particulate nickel metal (Ni) and particulate nickel ferrite ($NiFe_2O_4$) deposit at the surface of the CRUD. The kinetics of this deposition are enhanced with increasing boiling. Once deposited, solid Ni reacts with the soluble Fe concentrated in the CRUD to form nickel ferrite ($NiFe_2O_4$). Subsequently, $NiFe_2O_4$ reacts with the soluble B and Ni to become bonaccordite (Ni_2FeBO_5). The precipitation straight from aqueous reactants of nickel metal, nickel oxide, nickel ferrite, bonaccordite, and lithium tetraborate ($Li_2B_4O_7$) are also considered, the occurrence of which causes a decrease in the CRUD porosity. The kinetic rate of each of these reactions is scaled with the concentration of the soluble species involved, relative to the concentration in excess of the equilibrium concentration.

Sufficient characterization data exists to include four cases in the overall calibration, one from Callaway Cycle 9, one from Seabrook Cycle 5, and two from Callaway Cycle 10. Since the most complete and accurate characterization was performed for Callaway Cycle 9 [4, 5, 17] its data is first calibrated separately to determine the chemical reaction rates, which are universal properties. The deposition rates, however, are dependent on plant, cycle, and even location in the reactor due to differences in coolant chemistry, component age, and localized coolant turbulence [36]. Most importantly, the coolant concentrations of particulates circulating in the coolant are contained within the deposition rate values. Therefore, a subsequent calibration is performed for Seabrook Cycle 5 and Callaway Cycle 10 to determine each surface deposition rate, as well as evaluate the predictive power of the reaction rate results from the first calibration.

5.2 Description of the Variables and Search Parameters

There are five response parameters from MAMBA at the end of the simulated fuel cycle that can be compared to the characterized CRUD scrapes obtained from the fuel rods. The first is the final CRUD thickness. Three parameters are associated with the total phase fractions by weight percent of $NiFe_2O_4$, Ni, and Ni_2FeBO_5. The last parameter involves the Ni/Fe ratio by wt. % of the CRUD scrape. For Callaway Cycle 9, the Ni/Fe ratio across the radial dimension of the sample is also considered in the response parameters because data is available as a function of the radial position [4].

The CRUD phases modeled in the simulations are $NiFe_2O_4$, Ni, and Ni_2FeBO_5. Ni is selected over NiO due to its predicted thermodynamic stability during operation, as shown in Figure 4.9. The contribution of ZrO_2 is omitted from the modeling calibration, leaving greater fractions of $NiFe_2O_4$, Ni, and Ni_2FeBO_5, as reported in Table 5.1. The Ni/Fe ratios measured by Electron Dispersion Spectroscopy (EDS) along three different locations in the Callaway Cycle 9 flake are plotted in Figure 5.4 as a function of radial position. The B, Ni, and Fe concentrations of the samples from Callaway Cycle 10 and Seabrook 5 were measured by ICP, and the corresponding weight fractions of $NiFe_2O_4$, Ni, and Ni_2FeBO_5 are estimated and reported in Table 5.1.

There are also five uncertain kinetic rate parameters in MAMBA that affect the simulated composition of CRUD. These rate parameters describe the:

- Surface deposition of Ni
- Surface deposition of $NiFe_2O_4$
- **Ni(s)+ $2Fe^{2+}$ + $4H_2O$ $\Rightarrow$ $NiFe_2O_4$(s) + $4H^+$ + $2H_2$(g)**
- **$NiFe_2O_4$(s) + Ni^{2+} + $B(OH)_3$ + $0.5H_2$(g) $\Rightarrow$ Ni_2FeBO_5(s) + Fe^{2+} + $2H_2O$**
- Fe^{2+} + $2Ni^{2+}$ + $B(OH)_3$ + $2H_2O$ $\Rightarrow$ **Ni_2FeBO_5(s)** + $6H^+$ + $0.5H_2$(g)

The calibration is performed on these five search parameters to best match the observations of CRUD thickness and composition measured from plant samples. Dakota generates input parameters based on the probability density functions [45] and performs 10,000 chain sample iterations of the MAMBA simulations of each of the four CRUD samples. Weighting is applied to the residual errors based on the uncertainty of each measurement. The original first prior density functions are assumed constant within a given range of acceptable values. The final posterior density functions described in Table 5.2 are skewed distributions, meaning the mean value is different from the *maximum a posteriori* estimate (MAP), or best fit parameter value.

5.3 Sensitivity of the Variables on the Search Parameters

The calibration allows for the sensitivity of the response values based on the uncertain variables. Figure 5.5 shows the sensitivity of each response parameter on each search parameter from the Seabrook Cycle 5 simulation. The fuel rod heat flux was also included in this analysis to better understand the model response, in which the heat flux was varied from 121.5 to 148.5

Table 5.1 Measured and Simulated Properties of the Four CRUD Samples Used in the Calibration

	Callaway R9		Seabrook R5		Callaway R10 Sample 1		Callaway R10 Sample 2	
	Measured	MAMBA	Measured	MAMBA	Measured	MAMBA	Measured	MAMBA
Thickness (μm)	100	99.5	72	70.2	32.5	31.7	18.3	15.4
$NiFe_2O_4$ wt.%	7-21	16.8	23-24	20.8	60-62	12.1	47-48	16.2
Ni wt.%	9-20	12.4	7-9	10.9	12-16	0.7	4-6	0.3
Ni_2FeBO_5 wt.%	70	70.8	69	68.3	25	87.3	48	83.5
Ni/Fe wt. ratio	2.81	2.09	1.71	1.91	1.13	1.75	1.15	1.64
B conc. (mg·cm^{-2})		2.36		1.42		0.29		0.09
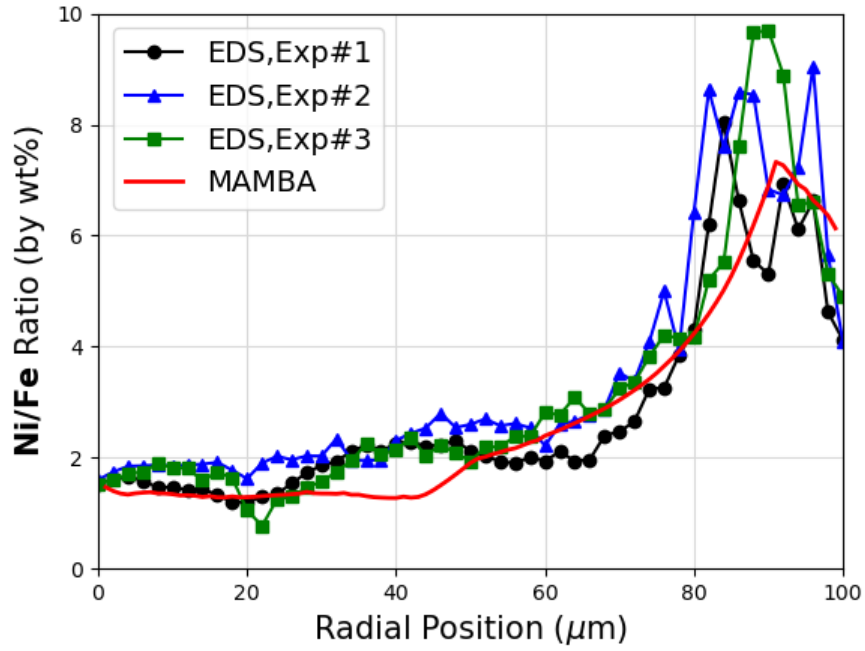
Figure 5.4: Elemental composition radial profile showing the Ni/Fe ration by wt% from EDS measurements [4] of a CRUD scrape from cycle 9 of the Callaway power plant and the simulation prediction at the end-of-cycle resulting from the calibration of the kinetic parameters in MAMBA

Table 5.2: Results from the Calibration of the Kinetic Rate Search Parameters

	Kinetic Prefactor	Mean	Std. Dev.	Skewness	Kurtosis	MAP
Chemical Reactions:						
	$Ni \Rightarrow NiFe_2O_4$	9.32E+16	1.03E+16	2.40E+00	1.86E+01	8.59E+16
	$NiFe_2O_4 \Rightarrow Ni_2FeBO_5$	1.62E+06	1.12E+05	-5.49E+00	5.44E+01	1.59E+06
	Ni_2FeBO_5 from soln.	4.56E+26	2.79E+25	4.82E+00	7.42E+01	4.55E+26
Callaway R9:						
	Surf. dep. $NiFe_2O_4$	5.01E+01	1.26E+01	2.78E+00	3.10E+01	4.91E+01
	Surf. dep. Ni	1.64E+02	7.51E+00	8.51E+00	8.59E+01	1.63E+02
Callaway R10 #1:						
	Surf. dep. $NiFe_2O_4$	5.60E+01	9.78E+00	1.03E+01	1.53E+02	5.61E+01
	Surf. dep. Ni	5.29E+00	6.66E+00	1.02E+01	1.20E+02	5.53E+00
Callaway R10 #2:						
	Surf. dep. $NiFe_2O_4$	2.63E+01	1.44E+01	7.99E+00	9.56E+01	1.86E+01
	Surf. dep. Ni	2.57E+00	9.24E+00	1.04E+01	1.17E+02	9.89E-02
Seabrook R5:						
	Surf. dep. $NiFe_2O_4$	5.25E+01	2.09E+01	1.71E+00	7.68E+00	3.48E+01
	Surf. dep. Ni	9.39E+01	2.66E+01	-9.52E-01	5.11E-01	1.11E+02
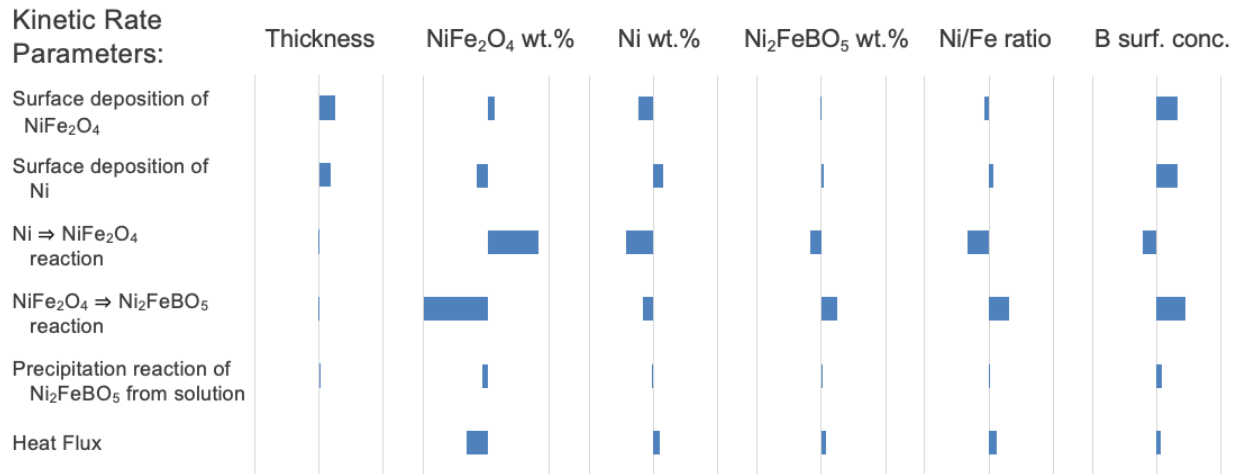
Figure 5.5: The sensitivity of the response variables on the search parameters

about a mean value of 135 Wcm^{-2}. As expected, the surface deposition rates have the largest influence on the CRUD thickness. The surface deposition rates of Ni metal and NiFe$_2$O$_4$ also affect CRUD composition by modifying the NiFe$_2$O$_4$ and Ni fractions as expected but have very little effect on Ni$_2$FeBO$_5$ fraction. The reactions of solids represented by Reactions 2.31 and 2.32 have the greatest effect on composition, especially the Ni$_2$FeBO$_5$ fraction and Ni/Fe ratio. The precipitation of solids from solution such as Reaction 2.29 have very small effects on composition and play a minimal role in the overall morphology of the CRUD. The NiFe$_2$O$_4$ fraction shows the greatest sensitivity to the input parameters, with the resulting wt% value exhibiting a delicate balance between the reactions of Ni to form NiFe$_2$O$_4$ and NiFe$_2$O$_4$ to form Ni$_2$FeBO$_5$. Increasing heat flux drives the CRUD composition to have less NiFe$_2$O$_4$ and more Ni and Ni$_2$FeBO$_5$ due to increased boric acid concentrations driving forward the reaction of NiFe$_2$O$_4$ to form Ni$_2$FeBO$_5$. Thus, increased heat flux leads to a slightly greater Ni/Fe ratio and boron concentration. The surface boron concentration shown in the last column of Figure 5.5 is positively affected by surface deposition rates by increasing overall CRUD mass. The boron concentration is negatively affected by the formation of NiFe$_2$O$_4$ which competes with the Ni$_2$FeBO$_5$ fraction. The kinetic rate of the reaction of NiFe$_2$O$_4$ to form Ni$_2$FeBO$_5$ has the greatest effect on the boron surface concentration.

5.4 Results of the Calibration

The calibration suggests that both Ni metal and NiFe$_2$O$_4$ surface deposition must occur. The concentration of NiFe$_2$O$_4$ particulates in the coolant available are allowed to vary as a function of the surface deposition rates of the CRUD. This accounts for the depletion of NiFe$_2$O$_4$ by trapping in the CRUD when growth rates are rapid [9]. NiFe$_2$O$_4$ formation and release rates become less than the deposition rates when the CRUD becomes sufficiently thick, causing more internal boiling. Ni metal particulates are assumed to remain abundant in the bulk coolant.

Table 5.2 shows the results of the calibration of the kinetic rate search parameters. The best fit parameters are given by the MAP values in the last column. The chemical reaction rates are universal for each cycle. The probability distribution functions of the chemical reaction rates and the Callaway R9 surface deposition rates have relatively and high kurtosis, suggesting they are fairly well-determined by the calibration. The Seabrook R5 deposition rates, however, have

lower kurtosis and may be less well-determined. All kinetic rates have highly skewed probability distribution functions.

A comparison between the experimental measurements and the calibrated MAMBA simulation results is shown in Table 5.1. The thicknesses are well matched, albeit the simulated value for Callaway R10 Sample 2 is a bit too low. The weight fractions for the Callaway Cycle 9 and Seabrook Cycle 5 samples are in excellent agreement. The amount of Ni_2FeBO_5 in the Callaway Cycle 10 simulations, however, is too great, which causes the weight fractions of Ni and $NiFe_2O_4$ to be too low and the overall Ni/Fe ratio to be too great. It follows that the calibrated MAMBA models provide better fit to thicker samples that are more likely to cause AOA than to thinner samples. In the last row of Table 5.1, the boron surface concentration of each simulated sample is given, showing that the Callaway Cycle 9 and Seabrook Cycle 5 samples are simulated to have significantly more boron than the Callaway Cycle 10 samples.

Figure 5.6 shows the simulated radial phase composition profile at three different times during Callaway Cycle 9. Ni and $NiFe_2O_4$ react with the soluble species inside the CRUD to form Ni_2FeBO_5, and by the end-of-cycle, Ni_2FeBO_5 exists in a high concentration and can cause significant AOA. Reaction of Ni metal to form $NiFe_2O_4$ and Ni_2FeBO_5 cause the porosity to decrease. $NiFe_2O_4$ concentration is highest near each edge of CRUD and lowest in the middle. $NiFe_2O_4$ particulates deposit at the surface and decrease in concentration approaching the middle of the sample due to its reaction to form Ni_2FeBO_5. In the lower portion of the CRUD near the cladding, $NiFe_2O_4$ concentration is high due to the reaction of Ni to form $NiFe_2O_4$. Ni concentration is highest near the coolant surface where Ni particulates deposit and decrease due its reaction to form $NiFe_2O_4$ and Ni_2FeBO_5. Ni_2FeBO_5 concentration increases moving inward toward the cladding. Very small amounts of $Li_2B_4O_7$ precipitation occur in the lower half near the cladding in areas of zero porosity, but still 99% of the total boron trapped within the simulated CRUD exists as Ni_2FeBO_5. By the end-of-cycle, there is a Ni_2FeBO_5-rich region in the lower two-thirds region of the CRUD near the cladding with a Ni/Fe ratio of ~2 shown in Figure 5.4, and a Ni-rich region near the interface with the coolant (outer radius of the CRUD), which matches observations from sample characterization [4, 17]. The small drop in Ni/Fe ratio seen on the far right-side of Figure 5.4 corresponds to concentration of $NiFe_2O_4$ particles at the surface that did not have sufficient time to react forming Ni_2FeBO_5.
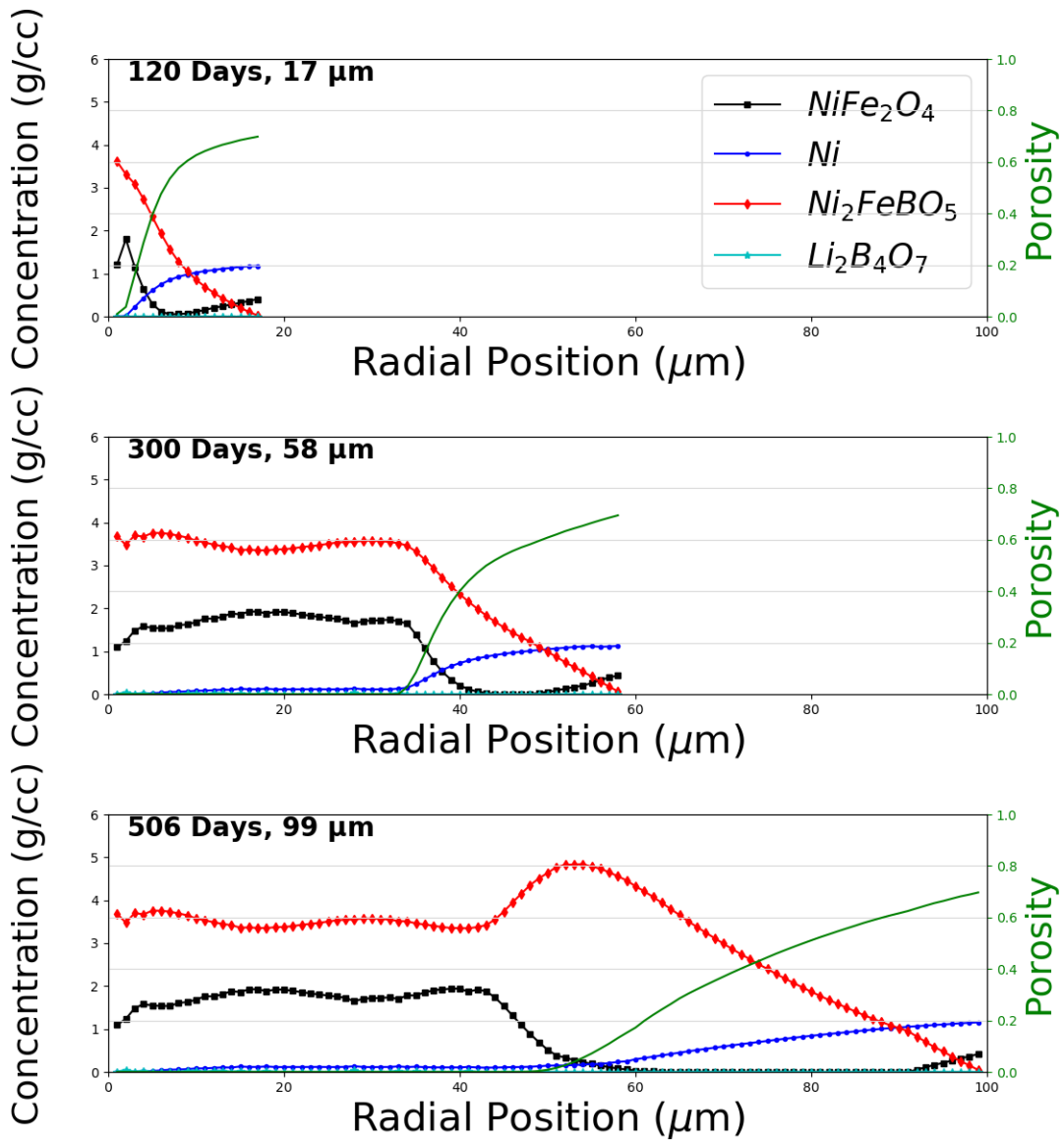
Figure 5.6: Simulated phase composition radial profile to match the sample from Callaway Cycle 9

The Seabrook Cycle 5 simulation was performed using the chemical reaction rates in Table 5.2 determined from the Callaway Cycle 9 calibration. The surface deposition rates of Ni and $NiFe_2O_4$ particles were still determined by a separate calibration, which are less than those from Callaway Cycle 9, resulting in thinner CRUD. The composition of the Seabrook Cycle 5 sample simulation, shown in Figure 5.7, is very similar to that of the Callaway Cycle 9 sample. The main difference is a greater fraction of Ni_2FeBO_5 is near the cladding in Seabrook Cycle 5, where the greater fraction of Ni_2FeBO_5 being in the middle region in Callaway Cycle 9.

The Callaway Cycle 10 simulations, depicted in Figure 5.8, show different behavior than the Callaway Cycle 9 and Seabrook Cycle 5 simulations. Callaway Cycle 10 had almost all $NiFe_2O_4$ surface deposition with virtually no Ni deposition. All inner $NiFe_2O_4$ near the cladding reacted to form Ni_2FeBO_5, causing the overconcentration of Ni_2FeBO_5 in the simulations of both samples.

5.5 Discussion

The calibration produced simulation results of Callaway Cycle 9 that match the sample characterization very well. The sample Ni/Fe ratio profile plotted in Figure 5.4 is matched with good accuracy and is predicted to consist of an Fe-rich inner region consisting of Ni_2FeBO_5 and $NiFe_2O_4$ and an outer region of increasing Ni concentration moving toward the coolant interface. The small region of increasing Fe concentration at the coolant interface is due to surface deposition of $NiFe_2O_4$ that did not have sufficient time to react to form Ni_2FeBO_5. There is a notable region around the 40 µm location of Figure 5.4 where the simulated $NiFe_2O_4$ concentration is too great, and produces a Ni/Fe ratio that is about 40% less than experimentally measured by EDS. The Ni/Fe ratio in the outer region is slightly below the mean of the EDS data of that region, but well within the uncertainty range of the three measurements. The overall phase fractions predicted by MAMBA in Table 5.1 match the Callaway Cycle 9 sample results measured by Mössbauer transmission spectroscopy extremely well, showing the majority Ni_2FeBO_5 concentration.

Providing some credence to the Callaway Cycle 9 calibration, the calculated chemical reaction kinetic rates produced good results in the simulation of a sample from Seabrook Cycle 5. This sample from a separate plant is slightly thinner, but still considered to be relatively thick,
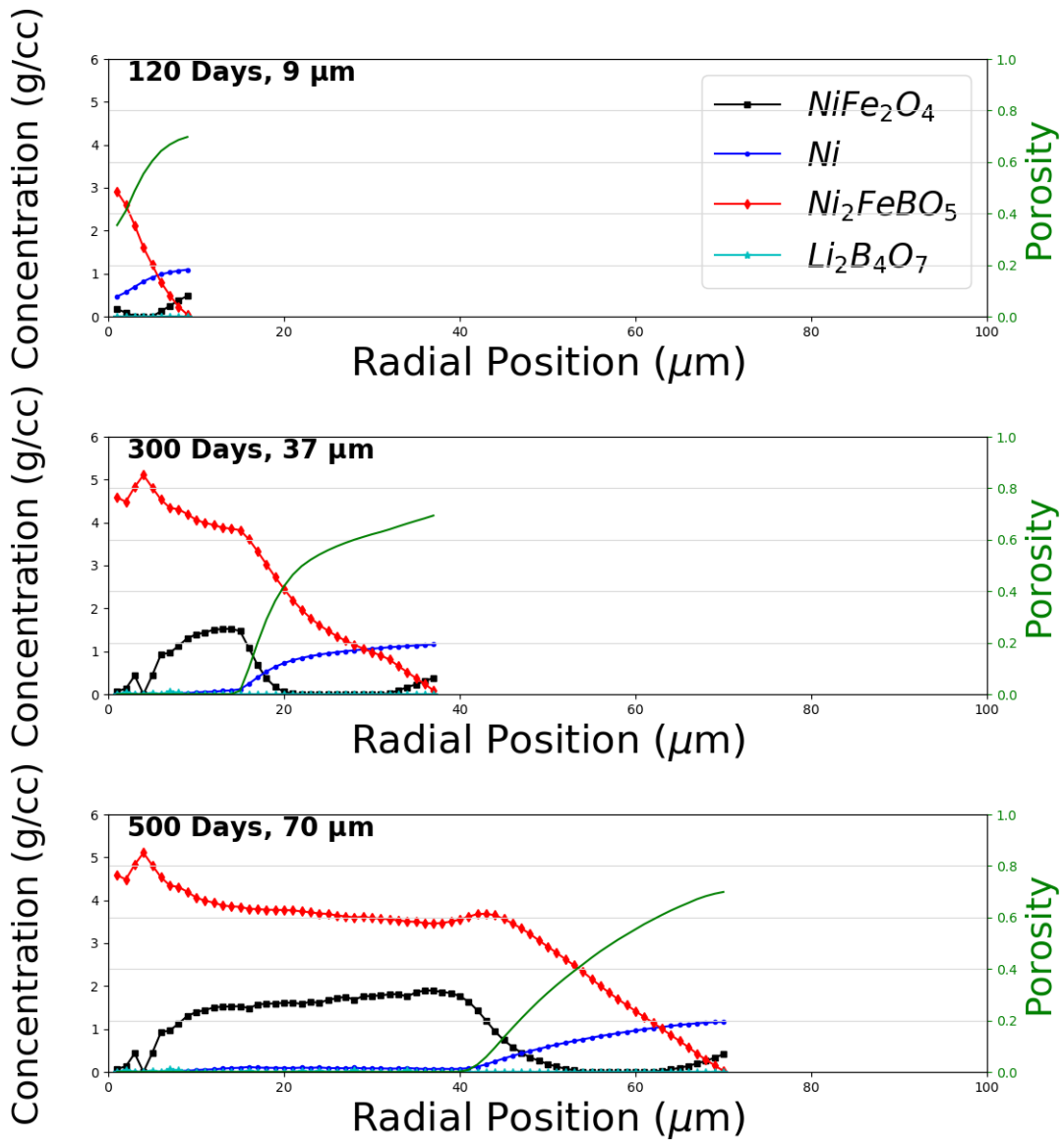
Figure 5.7: Simulated phase composition radial profile of the sample from Seabrook Cycle 5
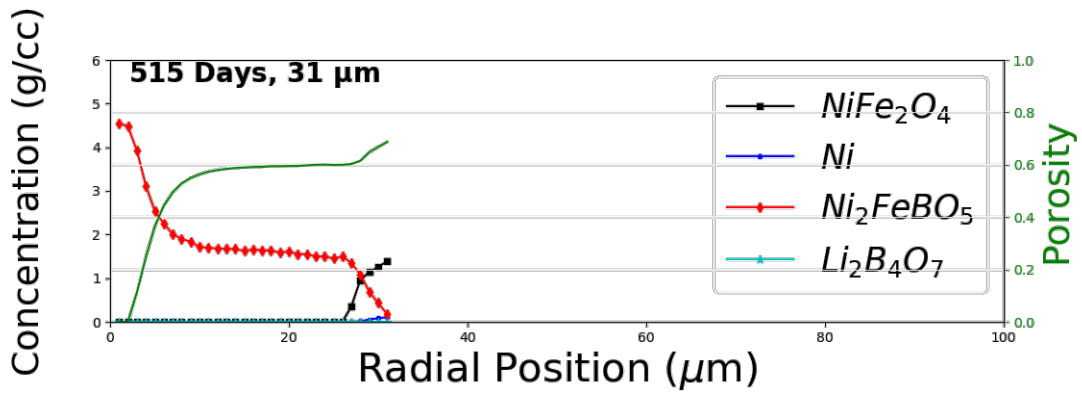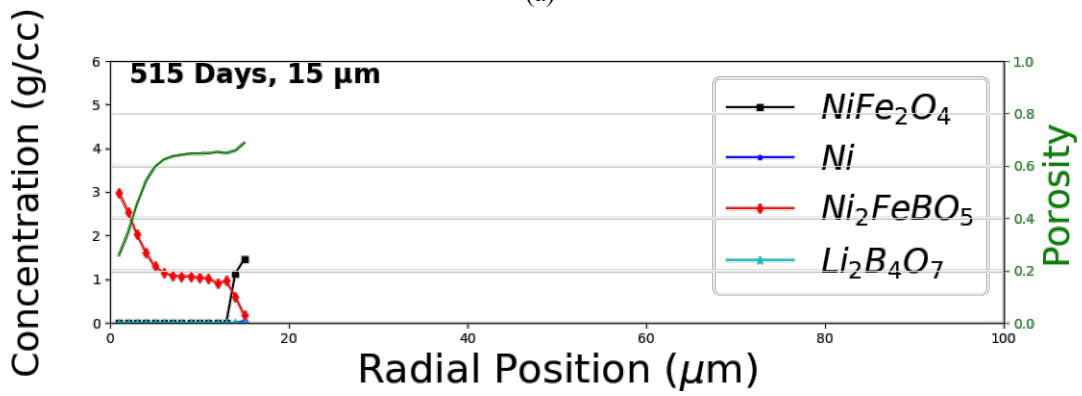
Figure 5.8: Simulated phase composition radial profile from samples 1 (a) and 2 (b) from Callaway Cycle 10

and is simulated to have a very similar morphology resulting in significant Ni_2FeBO_5 concentration.

In the simulations of Callaway Cycle 9 and Seabrook Cycle 5, porosity reaches zero near the cladding, preventing further precipitation reactions to occur. During characterization it was noted that porosity varied throughout the scale, and was especially low near the cladding interface [4]. The simulations show lithium tetraborate precipitation is possible near the cladding, but the region lacked the porosity to allow much precipitation. This is likely an underestimate of the amount of lithium tetraborate that is suggested to be truly present based on the lithium and boron release observed in the coolant [14] disscussed in Section 1.1.6.

The simulations of Callaway Cycle 10 do not match the characterization data as well as they did for Callaway Cycle 9 or Seabrook Cycle 5. This is primarily due to a much larger predicted Ni_2FeBO_5 concentration within the CRUD. The primary difference in the simulations is the time available for $NiFe_2O_4$ to react to form Ni_2FeBO_5 before the porosity is filled, cutting off the supply of aqueous species necessary for the reaction to occur. In addition, the calibration sets the surface deposition of Ni greater in Callaway Cycle 9 and Seabrook Cycle 5 and the deposition of $NiFe_2O_4$ greater in Callaway Cycle 10.

The concentration of Ni_2FeBO_5 produced by MAMBA simulations is fairly insensitive to small changes in the DFT-predicted thermodynamic properties of Ni_2FeBO_5 and is more sensitive to the aqueous boron concentration trapped within the CRUD which establishes the driving force for the chemical reaction rate. Figure 5.9 shows the boron surface concentration as a function of the increase (% change) of the enthalpy of formation of Ni_2FeBO_5. The enthalpy of formation must decrease beyond a threshold of 3 % before meaningfully altering the simulation by reducing the precipitation of Ni_2FeBO_5. Figure 5.9 indicates that two possible regimes for the amount of expected Ni_2FeBO_5 within the CRUD based on the value of the enthalpy of formation. The regime of greater Ni_2FeBO_5 stability is defined by the roughly constant amount of trapped boron for enthalpy values increased by less than 3 %. The second regime is defined by the roughly constant amount of boron for enthalpy values greater than 4 %. In order to simulate the observed abundance of Ni_2FeBO_5 in CRUD from Callaway Cycle 9 [17], the regime of greater stability given by small changes in enthalpy (below 3% increase) is preferred. Therefore, the result of too much Ni_2FeBO_5 in Callaway Cycle 10 is likely due to deficiencies in the chemical
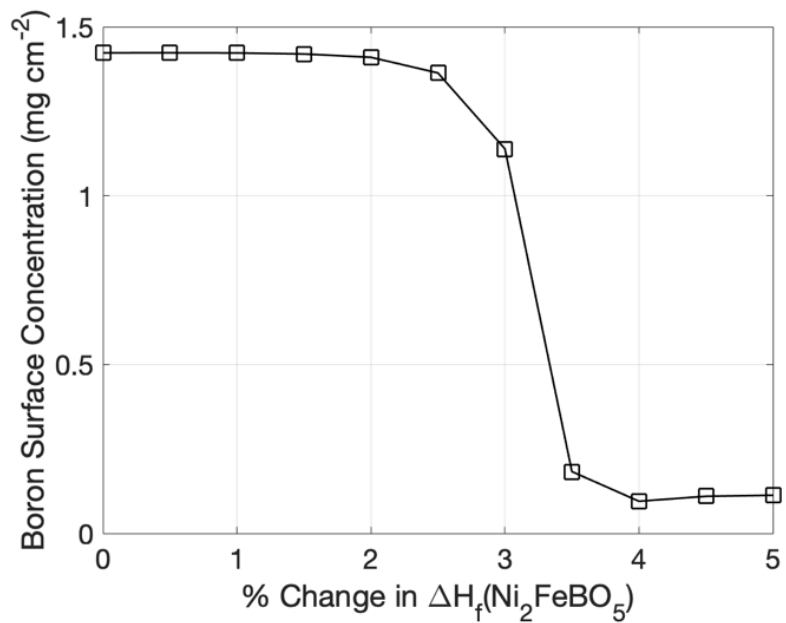
Figure 5.9: The effect of variation in the enthalpy of formation for Ni$_2$FeBO$_5$ on the simulated boron surface concentration trapped in Seabrook Cycle 5 CRUD using MAMBA

kinetic or transport models in MAMBA, and not due to uncertainties in the thermochemistry data.

5.6 Summary of the Calibration

A Bayesian calibration was performed to determine the kinetic rates of the surface deposition of particulates and of the thermodynamically predicted precipitation reactions. This calibration was performed using sample data from Callaway Cycle 9 to determine the chemical reaction rates, and these rates were tested in subsequent calibrations using data from Seabrook Cycle 5 and Callaway Cycle 10. Four samples were analyzed in total. It is found that the surface depositions of both Ni metal particulates and $NiFe_2O_4$ particulates are necessary to account for the experimental characterization of the CRUD scrapes. Ni metal reacts with soluble Fe to form $NiFe_2O_4$, and $NiFe_2O_4$ reacts with boric acid to form Ni_2FeBO_5, ultimately filling in the CRUD porosity near the cladding.

CHAPTER 6. CONCLUSIONS

6.1 Work Completed

The models presented in this dissertation provide a plausible explanation for the chemical composition of AOA-causing CRUD. Based on supporting thermodynamic calculations and a Bayesian calibration of the kinetic rates, CRUD simulations predict a multilayered structure, with a high concentration of bonaccordite (Ni_2FeBO_5) near the cladding and a Ni-rich region near the coolant interface. These results correspond well with plant observations [4, 5, 18].

A detailed thermodynamic description of CRUD is implemented in a CALPHAD model. Included in the model are new HKF parameters listed in Tables 3.1 and 4.1 that can be used to define the thermophysical properties of aqueous species in a PWR up to the saturation temperature of 345 °C. The HKF formalism [25, 26] provides a theoretically rigorous, yet flexible framework to calculate the thermodynamic properties of aqueous species at high temperatures. Much of the relevant aqueous data [24, 54, 56, 75, 80, 81] for PWRs only reaches 300 °C and therefore must be extrapolated using the HKF framework up to 345 °C. In addition, the Pitzer equations [27] are utilized to describe the excess Gibbs energy resulting from the electrostatic interaction between aqueous species and the solvent as well as shorter-range interactions between the borate anions with the alkali metal cations, with parameters listed in Table 3.2.

A thermodynamic database of possible solid precipitates is constructed by combining experimental [12, 20, 57, 77, 78, 83] and DFT [29-31] data, and using various estimation techniques [32, 82]. Implementing this database using CALPHAD, it is predicted that nickel ferrite ($NiFe_2O_4$), nickel metal (Ni), and bonaccordite (Ni_2FeBO_5) are the stable components of CRUD, with the overall phase diagram presented in Figure 4.8. $NiFe_2O_4$ is stable at pH values of 7.0 or lower and boron concentrations below 0.15 $mol \cdot kg^{-1}$. Ni metal is stable at elevated pH above 7.0 and high H_2 concentrations above 17.1 $cm^3(STP)kg^{-1}$ that limit dissolved oxygen. Ni_2FeBO_5 is stable at high B concentrations above 0.15 $mol \cdot kg^{-1}$. Boron incorporation in the defected nickel ferrite crystal structure is ruled out as a significant boron retention mechanism. Also, precipitation of $Li_2B_4O_7$ is predicted to occur when pH is elevated, greater than 7.0, and boric acid concentration reaches extremely high concentrations shown by the phase diagram in Figure 3.12. It is noted that the CALPHAD model does not predict precipitation of either $K_2B_4O_7$

or any borate salt over the same range of conditions if KOH replaces LiOH. The use of KOH does not rule out HBO_2 or borate precipitation, which is predicted to occur at high boron concentrations above 7.3 mol kg^{-1}.

The thermodynamic calculations inform the overall model developed in MAMBA. Nickel metal is stable in the coolant at typical PWR pH values in the range of 6.9 to 7.4, and nickel ferrite ($NiFe_2O_4$) is stable if the pH drops below 6.75. It is deduced that nickel metal and/or nickel ferrite particles circulating in the coolant deposit on fuel rod surfaces growing CRUD. Once CRUD sustains internal boiling, it maintains a saturation temperature of 345 °C and concentrates soluble boron. Nickel metal in the CRUD reacts with aqueous Fe to form nickel ferrite if the pH is 7.0 or less. If the boron concentration exceeds 0.15 mol·kg^{-1} (1620 ppm) the nickel ferrite reacts with aqueous B and Ni to form bonaccordite (Ni_2FeBO_5).

MAMBA is used to simulate CRUD growth and composition. The growth is driven by the deposition of nickel metal and nickel ferrite particulates from the coolant. The heat and species transport within the CRUD scale is tracked, and internal precipitation reactions are modeled to fill the CRUD pores. The set of reactions detailed by 2.25-2.32 are informed by the thermochemistry models described in Chapters 3 and 4.

A Bayesian calibration of the kinetic rates in the MAMBA model was performed to match an available CRUD sample characterization [4, 17]. The calibration of MAMBA was successful in matching and explaining the observed characterization of Callaway Cycle 9 CRUD. Subsequently, the chemical reaction rates from this calibration were applied to Seabrook Cycle 5 and Callaway Cycle 10 CRUD. The simulations of the Seabrook Cycle 5 sample showed excellent agreement with the characterization data [5], although the simulations of Callaway Cycle 10 CRUD predict too much bonaccordite as shown in Table 5.1. Nevertheless, the calibration exercise provides insight into the CRUD morphology throughout the length of a reactor cycle. It is determined that the surface deposition of both Ni metal particulates and $NiFe_2O_4$ particulates occur. As well, the synthesis of Ni_2FeBO_5 from solid Ni or $NiFe_2O_4$ reacting with soluble boron accounts for the observed abundance of Ni_2FeBO_5 [17], which contributes significantly to AOA.

The simulations of Callaway Cycle 9 and Seabrook Cycle 5 demonstrate the layered development of AOA-causing CRUD as it grows. Ni metal particulates present due to their deposition at the surface react to form $NiFe_2O_4$ and/or Ni_2FeBO_5 which decreases the porosity.

NiFe$_2$O$_4$ concentration in CRUD is highest near the cladding interface and lowest in the middle. NiFe$_2$O$_4$ particulates deposit at the CRUD-coolant interface and decrease in concentration with increasing CRUD thickness due to its reaction to form Ni$_2$FeBO$_5$. In the inner portion of the CRUD near the cladding, the NiFe$_2$O$_4$ concentration is high due to the reaction of Ni to form NiFe$_2$O$_4$. Ni concentration is highest near the coolant surface where Ni particulates deposit and decrease due its reaction to form NiFe$_2$O$_4$ and Ni$_2$FeBO$_5$. Ni$_2$FeBO$_5$ concentration increases moving inward toward the cladding. Very small amounts of Li$_2$B$_4$O$_7$ precipitation occur in CRUD near the cladding in areas of near-zero porosity, ultimately contributing little to the total boron contained in the CRUD as compared to Ni$_2$FeBO$_5$ formation. By the end-of-cycle, there is a Ni$_2$FeBO$_5$-rich region in the inner two-thirds region of the CRUD near the cladding with a Ni/Fe ratio of ~2 shown in Figure 5.4, and a Ni-rich region near the interface with the coolant (outer radius of the CRUD), which matches observations from sample characterization [4, 17].

The simulated CRUD composition including the total amount of boron retention shows strong sensitivity on the surface deposition rates and the solid-to-solid internal precipitation reaction rates. In comparison, the reaction rate of bonaccordite straight from aqueous species has less effect on the total boron retention in CRUD. In the simulations, rod heat flux variation also has little effect within the range from 121.5 to 148.5 Wcm^{-2}. Small changes in the thermochemical property values of bonaccordite have no effect on total boron retention, as demonstrated by Figure 5.9.

This work drives MAMBA closer to the goal of simulating the solid chemical composition and morphology of CRUD throughout fuel cycles across a range of PWR plant conditions, although further addition of lithium and boron containing precipitation products may be warranted in the future as discussed in the next section.

6.2 Limitations and Future Work

The completion of this dissertation addresses key areas of doubt when it comes to predicting the composition of CRUD and the associated reactor performance concerns. Nevertheless, the models presented have a number of deficiencies that limit their ability to explain the chemical composition of CRUD. The principal deficiencies are present in the multi-physics continuum modeling using MAMBA; however, the thermochemistry models have uncertainties as well. Several of the aqueous chemistry models are extrapolations based on

measurements at lower temperatures, albeit using a rigorous thermodynamic framework. Also, the thermophysical properties of bonaccordite are estimated computationally, but have not been measured through synthesis, and therefore have greater uncertainty. While the simulated CRUD results are shown to be stable for small perturbations in these values, if the true property values are outside certain thresholds, the models and conclusions presented here could change drastically.

Due to the complex multiphysics nature of CRUD, the deposition and transport models in MAMBA contain many dificiencies, and the predicted CRUD conditions are fairly uncertain. For instance, the wick boiling model decribed in Section 2.2.2 does not fully consider two-phase mixture fluid flow [85]. Furthermore, MAMBA does not consider the effects of radiolysis [21], which could cause more oxidizing conditions that could possibly account for the presence of NiO instead of Ni in some cases [5].

A fundamental microstructural detail of CRUD that plays a key role in these MAMBA simulations is the porosity. It is known that porosity impacts the effective thermal conductivity of CRUD [13], which impacts boiling chimney spacing and fill characteristics. In the simulations of Callaway Cycle 9 and Seabrook Cycle 5, porosity reaches zero near the cladding, preventing further precipitation reactions to occur. During characterization it was noted that porosity varied throughout the scale, and was especially low near the cladding interface [4]. The simulations show lithium tetraborate precipitation is possible near the cladding, but the region lacked the porosity to allow much precipitation. Likewise, improvements in modeling boiling and two-phase flow in the boiling chimneys may lead to predictions of boric acid concentration sufficient to enable HBO_2 or borate phase to precipitate. Moreover, the amount of lithium tetraborate in the simulations is significantly less than suggested based on the lithium and boron release observed in the coolant during shutdown [14], as disscussed in Section 1.1.6. However, the mass balance of Li vs B release hints that lithium tetraborate precipitation alone cannot fully explain this observation. For these reasons, improved modeling of porosity and boiling chimeny behavior across the CRUD scale would be a valuable addition to MAMBA modeling fidelity, and could provide a calibration response parameter for future work if adequate experimental data can be obtained.

One major limitation for the models presented is that they do not consider Zr thermochemistry or transport throughout the CRUD layer. Without this information, MAMBA is

not able to completely explain the middle ZrO_2-rich region observed in AOA-rich CRUD that may be explained as a result of the variation in pH with spatial position throughout the deposit [21, 22]. As well, CRUD likely undergoes chemical changes during reactor shutdown [14]. The thermochemistry changes that occur at shutdown have not been considered in this work. Also, the kinetics of dissolution at shutdown and the effects of the CRUD bursting are not modeled.

Lastly, these simulations were performed using MAMBA in isolation. It would be beneficial to extend them to full VERA simulations to get an idea of the local conditions and the AOA.

LIST OF REFERENCES

[1]   M. P. Short, "The particulate nature of the crud source term in light water reactors," *Journal of Nuclear Materials,* vol. 509, pp. 478-481, 2018, doi: 10.1016/j.jnucmat.2018.07.008.

[2]   Electric Power Research Institute (EPRI), "Modeling PWR Fuel Corrosion Product Deposition and Growth Processes," Palo Alto, CA, 2004.

[3]   Electric Power Research Institute (EPRI), "Modeling PWR Fuel Corrosion Product Deposition and Growth Process: Final Report," Palo Alto, CA, 2005.

[4]   Electric Power Research Institute (EPRI), "Characterization of Corrosion Products on the Callaway Cycle 9 PWR Core," Palo Alto, CA, 2001.

[5]   J. S. W. A. Byers, G. P. Sabol, J. M. Partezanna, "Evaluation of Fuel Clad Corrosion Product Deposits and Circulating Corrosion Products in PWRs," 1009951, 2004.

[6]   B. K. Kendrick, "MAMBA Theory Manual," ed: Los Alamos National Laboratory, 2016.

[7]   D. J. Walter, B. K. Kendrick, V. Petrov, A. Manera, B. Collins, and T. Downar, "Proof-of-principle of high-fidelity coupled CRUD deposition and cycle depletion simulation," *Annals of Nuclear Energy,* vol. 85, no. C, pp. 1152-1166, 2015, doi: 10.1016/j.anucene.2015.07.034.

[8]   J. Deshon, Dennis Hussey, John Westacott, Mike Young, Jeff Secker, Kenny Epperson, John McGurk, Jim Henshaw, "Recent Development of BOA Version 3," presented at the NPC 2010, 2010.

[9]   J. M. Henshaw, J. C.; Sims, Howard E.; Tuson, Ann; Dickinson, Shirley; Deshon, Jeff, "The Chemistry of Fuel Crud Deposits and Its Effect on AOA in PWR Plants," 2006.

[10]   Z. Rák and D. W. Brenner, "Effect of water chemistry on the composition of oxides formed on stainless steel surfaces in light water reactors," *Journal of nuclear materials,* vol. 526, no. C, p. 151773, 2019, doi: 10.1016/j.jnucmat.2019.151773.

[11]   C. J. O'Brien, Z. Rák, E. W. Bucholz, and D. W. Brenner, "First principles calculations predict stable 50 nm nickel ferrite particles in PWR coolant," *Journal of nuclear materials,* vol. 454, no. 1-3, pp. 77-80, 2014, doi: 10.1016/j.jnucmat.2014.07.049.

[12]   Electric Power Research Institute (EPRI), "Modeling PWR Fuel Corrosion Product Deposition and Growth Processes," Palo Alto, CA, 2004.

[13]   A. B. G. Wang, M. Young, "Simulated Fuel Crud Thermal Conductivity Measurements Under Pressurized Water Reactor Conditions," Westinghouse Electric Company LLC, Palo Alto, CA, 2011.

[14]   Electric Power Research Institute (EPRI), "PWR Axial Offset Anomaly (AOA) Guidelines, Revision 1," Palo Alto, CA, 2004.

[15]   J.-W. Yeon, I.-K. Choi, K.-K. Park, H.-M. Kwon, and K. Song, "Chemical analysis of fuel crud obtained from Korean nuclear power plants," *Journal of Nuclear Materials,* vol. 404, no. 2, pp. 160-164, 2010, doi: 10.1016/j.jnucmat.2010.07.024.

[16]   Y. Solomon and J. Roesmer, "Measurement of Fuel Element Crud Deposits in Pressurized Water Reactors," *Nuclear Technology,* vol. 29, no. 2, pp. 166-173, 1976, doi: 10.13182/NT76-A31576.

[17]   J. A. Sawicki, "Evidence of Ni2FeBO5 and m-ZrO2 precipitates in fuel rod deposits in AOA-affected high boiling duty PWR core," *Journal of Nuclear Materials,* vol. 374, no. 1, pp. 248-269, 2008, doi: 10.1016/j.jnucmat.2007.08.014.

[18]   J. D. W. Byers, "Structure and Chemistry of PWR Crud," in *Water Chem. in Nucl. Reactors Systems*, October 11-14 2004, San Francisco, USA.

[19]   Electric Power Research Institute (EPRI), "Experimental Verification of the Root Cause Mechanism for Axial Offset Anomaly," Palo Alto, CA, 2002.

[20]   W. Byers, W. Lindsay, and R. Kunig, "Solubility of Lithium Monoborate in High-Temperature Water," *Journal of Solution Chemistry,* vol. 29, no. 6, pp. 541-559, 2000, doi: 10.1023/A:1005194129783.

[21]   W. A. Byers, "EPRI AOA Science Workshop," ed, 2000.

[22]   Electric Power Research Institute (EPRI), "Modeling PWR Fuel Corrosion Product Deposition and Growth Process: Final Report," Palo Alto, CA, 2005.

[23]   J. Chen, F. Lindberg, D. Wells, and B. Bengtsson, "EELS and electron diffraction studies on possible bonaccordite crystals in pressurized water reactor fuel CRUD and in oxide films of alloy 600 material," *Nuclear Engineering and Technology,* vol. 49, no. 4, pp. 668-674, 2017, doi: 10.1016/j.net.2017.04.001.

[24]   R. E. Mesmer, C. F. Baes, and F. H. Sweeton, "Acidity measurements at elevated temperatures. VI. Boric acid equilibriums," *Inorganic Chemistry,* vol. 11, no. 3, pp. 537-543, 1972, doi: 10.1021/ic50109a023.

[25]   H. C. Helgeson, D. H. Kirkham, and G. C. Flowers, "Theoretical prediction of the thermodynamic behavior of aqueous electrolytes by high pressures and temperatures; IV, Calculation of activity coefficients, osmotic coefficients, and apparent molal and standard and relative partial molal properties to 600 degrees C and 5kb," *American Journal of Science,* vol. 281, no. 10, pp. 1249-1516, 1981.

[26]   J. C. Tanger and H. C. Helgeson, "Calculation of the thermodynamic and transport properties of aqueous species at high pressures and temperatures; revised equations of state for the standard partial molal properties of ions and electrolytes," *American Journal of Science,* vol. 288, no. 1, pp. 19-98, 1988, doi: 10.2475/ajs.288.1.19.

[27]   K. S. Pitzer, "Ion Interaction Approach: Theory and Data Correlation," in *Activity coefficients in electrolyte solutions*, K. S. Pitzer Ed., Second edition. ed. Boca Raton: CRC Press, 2018, ch. 3, pp. 75-147.

[28]   G. Scatchard, "Concentrated Solutions of Strong Electrolytes," *Chemical reviews,* vol. 19, no. 3, pp. 309-327, 1936, doi: 10.1021/cr60064a008.

[29]   Z. Rák, C. J. O'brien, and D. W. Brenner, "First-principles investigation of boron defects in nickel ferrite spinel," *Journal of Nuclear Materials,* vol. 452, no. 1-3, pp. 446-452, 2014, doi: 10.1016/j.jnucmat.2014.05.031.

[30]   Z. Rák, E. W. Bucholz, and D. W. Brenner, "Defect formation in aqueous environment: Theoretical assessment of boron incorporation in nickel ferrite under conditions of an operating pressurized-water nuclear reactor (PWR)," *Journal of Nuclear Materials,* vol. 461, no. C, pp. 350-356, 2015, doi: 10.1016/j.jnucmat.2015.03.038.

[31]   Z. Rak, C. J. O'Brien, D. Shin, A. D. Andersson, C. R. Stanek, and D. W. Brenner, "Theoretical assessment of bonaccordite formation in pressurized water reactors," *Journal of Nuclear Materials,* vol. 474, pp. 62-64, 2016, doi: 10.1016/j.jnucmat.2016.02.016.

[32]   P. J. Spencer, "Estimation of thermodynamic data for metallurgical applications," *Thermochimica Acta,* vol. 314, no. 1-2, pp. 1-21, 1998, doi: 10.1016/S0040-6031(97)00469-3.

[33]   G. Cacciamani, "AN INTRODUCTION TO THE CALPHAD METHOD AND THE COMPOUND ENERGY FORMALISM (CEF)," *Tecnologia em Metalurgia, Materiais e Mineração,* vol. 13, no. 1, pp. 16-24, 2016, doi: 10.4322/2176-1523.1048.

[34]   C. W. Bale *et al.*, "FactSage thermochemical software and databases," *Calphad,* vol. 26, no. 2, pp. 189-228, 2002.

[35]   J. Deshon, D. Hussey, B. Kendrick, J. McGurk, J. Secker, and M. Short, "Pressurized water reactor fuel crud and corrosion modeling," *JOM,* vol. 63, no. 8, pp. 64-72, 2011, doi: 10.1007/s11837-011-0141-z.

[36]   V. Petrov, B. K. Kendrick, D. Walter, A. Manera, and J. Secker, "Prediction of CRUD deposition on PWR fuel using a state-of-the-art CFD-based multi-physics computational tool," *Nuclear Engineering and Design,* vol. 299, no. C, pp. 95-104, 2016, doi: 10.1016/j.nucengdes.2015.10.010.

[37]   D. J. Walter and A. Manera, "CRUD, boron, and burnable absorber layer 2-D modeling requirements using MOC neutron transport," *Annals of Nuclear Energy,* vol. 87, no. P2, pp. 388-399, 2016, doi: 10.1016/j.anucene.2015.09.021.

[38]   W. G. B. Collins, L. Gilkey, A. Eliott, B. Adams, D. Kropazek, "Calibration of Whole Core PWR Crud Simulations," presented at the Proc. Global/Top Fuel 2019, Seattle, Washington, September 22-26, 2019.

[39]   J. G. B. Collins, R. Salko, K. Clarno, A. Wysocki, B. Okhuysen, D. Anderson, "Whole Core Crud-Induced Power Shift Simulations Using VERA," in *Proc. PHYSOR 2018*, Cancun, Mexico, April 22-25, 2018.

[40]   W. G. B. Collins, R. Salko, "Crud Induced Power Shift Simulations using VERA," *Trans. Am. Nucl. Soc.,* 2020.

[41]   A. M. Elliot, Benjamin Collins, David Andersson, Michael Short, "CRUD Source Term Assessment and Development for VERA," CASL, 2019.

[42]   B. Collins W. Gurecky, A. Elliott, D. Andersson, J. Galloway, B. Kendrick, B. Okhuysen, "MAMBA v.2.0 Manual," CASL, 2019.

[43]   M. C. Kennedy and A. O' Hagan, "Bayesian calibration of computer models," *Journal of the Royal Statistical Society: Series B (Statistical Methodology),* vol. 63, no. 3, pp. 425-464, 2001.

[44]   J. P. Kaipio and E. Somersalo, *Statistical and Computational Inverse Problems* (Applied Mathematical Sciences, 160). New York, NY: Springer Science+Business Media, Inc., 2005.

[45]   B. M. Adams, et al., "Dakota, A Multilevel Parallel Object-Oriented Framework for Design Optimization, Parameter Estimation, Uncertainty Quantification, and Sensitivity Analysis: Version 6.10 User's Manual," Albuquerque, New Mexico, 2019.

[46]   S. Chib and E. Greenberg, "Understanding the Metropolis-Hastings Algorithm," *The American statistician,* vol. 49, no. 4, pp. 327-335, 1995, doi: 10.1080/00031305.1995.10476177.

[47]   P. Aaltonen, & Hanninen, H., "Water chemistry and behavior of materials in PWRs and BWRs (IAEA-TECDOC--965)," ed: International Atomic Energy Agency (IAEA), 1997.

[48]   D. A. Palmer, David J. Wesolowski, "Boric Acid Hydrolysis: A New Look at the Available Data," *PowerPlant Chemistry,* vol. 2, no. 5, pp. 261-264, 2000.

[49]   H. Dickinson, K. Garbett, "Thermodynamic Modeling of PWR Coolant," ed: AEAT/R/NT/0325, 2001.

[50]   L. Maya, "Identification of polyborate and fluoropolyborate ions in solution by Raman spectroscopy," *Inorganic Chemistry,* vol. 15, no. 9, pp. 2179-2184, 1976, doi: 10.1021/ic50163a036.

[51]   T. Hirao, M. Kotaka, and H. Kakihana, "Raman spectra of polyborate ions in aqueous solution," *Journal of Inorganic and Nuclear Chemistry,* vol. 41, no. 8, pp. 1217-1220, 1979, doi: 10.1016/0022-1902(79)80490-X.

[52]   Y. Zhou, C. Fang, Y. Fang, and F. Zhu, "Polyborates in aqueous borate solution: A Raman and DFT theory investigation," *Spectrochimica Acta Part A: Molecular and Biomolecular Spectroscopy,* vol. 83, no. 1, pp. 82-87, 2011, doi: 10.1016/j.saa.2011.07.081.

[53]   L. Applegarth, C. Pye, J. Cox, and P. Tremaine, "Raman Spectroscopic and ab Initio Investigation of Aqueous Boric Acid, Borate, and Polyborate Speciation from 25 to 80 degrees C," *Industrial & Engineering Chemistry Research,* vol. 56, no. 47, pp. 13983-13996, 2017, doi: 10.1021/acs.iecr.7b03316.

[54]   S. Sasidharanpillai, H. Arcis, L. Trevani, and P. R. Tremaine, "Triborate Formation Constants and Polyborate Speciation under Hydrothermal Conditions by Raman Spectroscopy using a Titanium/Sapphire Flow Cell," *The journal of physical chemistry. B,* vol. 123, no. 24, pp. 5147-5159, 2019, doi: 10.1021/acs.jpcb.9b03062.

[55]   P. Wang, J. Kosinski, M. Lencka, A. Anderko, and R. Springer, "Thermodynamic modeling of boric acid and selected metal borate systems," *Pure and Applied Chemistry. Chimie Pure et Appliquee,* vol. 85, no. 11, pp. 2117-2144, 2013, doi: 10.1351/pac-con-12-07-09.

[56]   H. Arcis, J. P. Ferguson, L. M. S. G. A. Applegarth, G. H. Zimmerman, and P. R. Tremaine, "Ionization of boric acid in water from 298K to 623K by AC conductivity and Raman spectroscopy," *The Journal of Chemical Thermodynamics,* vol. 106, pp. 187-198, 2017, doi: 10.1016/j.jct.2016.11.007.

[57]   J. W. Johnson, E. H. Oelkers, and H. C. Helgeson, "SUPCRT92: A software package for calculating the standard molal thermodynamic properties of minerals, gases, aqueous species, and reactions from 1 to 5000 bar and 0 to 1000°C," *Computers and Geosciences,* vol. 18, no. 7, pp. 899-947, 1992, doi: 10.1016/0098-3004(92)90029-Q.

[58]   J. Johnson and D. Norton, "Critical phenomena in hydrothermal systems: State, thermodynamic, electrostatic, and transport properties of H(2)O in the critical region," *American Journal of Science,* vol. 291, no. 6, p. 541, 1991, doi: 10.2475/ajs.291.6.541.

[59]   E. L. Shock and H. C. Helgeson, "Calculation of the thermodynamic and transport properties of aqueous species at high pressures and temperatures: Correlation algorithms for ionic species and equation of state predictions to 5 kb and 1000°C," *Geochimica et Cosmochimica Acta,* vol. 52, no. 8, pp. 2009-2036, 1988, doi: 10.1016/0016-7037(88)90181-0.

[60]   E. L. Shock, H. C. Helgeson, and D. A. Sverjensky, "Calculation of the thermodynamic and transport properties of aqueous species at high pressures and temperatures: Standard partial molal properties of inorganic neutral species," *Geochimica et Cosmochimica Acta,* vol. 53, no. 9, pp. 2157-2183, 1989, doi: 10.1016/0016-7037(89)90341-4.

[61]   W. Wagner and A. Pruß, "The IAPWS Formulation 1995 for the Thermodynamic Properties of Ordinary Water Substance for General and Scientific Use," *Journal of physical and chemical reference data,* vol. 31, no. 2, pp. 387-535, 2002, doi: 10.1063/1.1461829.

[62]   W. L. Marshall and E. U. Franck, "Ion product of water substance, 0–1000 °C, 1–10,000 bars New International Formulation and its background," *Journal of Physical and Chemical Reference Data,* vol. 10, no. 2, pp. 295-304, 1981, doi: 10.1063/1.555643.

[63] IAPWS, "Revised Release on the Ionization Constant of H2O," Banff, Canada, 2019.

[64] A. V. Bandura and S. N. Lvov, "The Ionization Constant of Water over Wide Ranges of Temperature and Density," *Journal of Physical and Chemical Reference Data,* vol. 35, no. 1, pp. 15-30, 2006, doi: 10.1063/1.1928231.

[65] G. S. Pokrovski, J. Schott, and A. S. Sergeyev, "Experimental determination of the stability constants of NaSO 4− and NaB (OH) 40 in hydrothermal solutions using a new high-temperature sodium-selective glass electrode — Implications for boron isotopic fractionation," *Chemical Geology,* vol. 124, no. 3, pp. 253-265, 1995, doi: 10.1016/0009-2541(95)00057-S.

[66] E. L. Shock, D. C. Sassani, M. Willis, and D. A. Sverjensky, "Inorganic species in geologic fluids: Correlations among standard molal thermodynamic properties of aqueous ions and hydroxide complexes," *Geochimica et Cosmochimica Acta,* vol. 61, no. 5, pp. 907-950, 1997.

[67] L. R. Hnědkovsky, V. R. Majer, and R. H. Wood, "Volumes and heat capacities of H 3BO 3(aq) at temperatures from 298.15 K to 705 K and at pressures to 35 MPa," *The Journal of Chemical Thermodynamics,* vol. 27, no. 7, pp. 801-814, 1995, doi: 10.1006/jcht.1995.0083.

[68] B. B. Owen and E. J. King, "The Effect of Sodium Chloride upon the Ionization of Boric Acid at Various Temperatures1," *Journal of the American Chemical Society,* vol. 65, no. 8, pp. 1612-1620, 1943, doi: 10.1021/ja01248a046.

[69] D. Manov, Acree, "Ionization Constant of Boric Acid and the pH of Certain Borax-Chloride Buffer Solutions From 0 to 60 C," *Journal of the National Bureau of Standards,* vol. 33, pp. 287-306, 1944, Art no. 1609.

[70] E. Bulemela and P. R. Tremaine, "D2O Isotope Effects on the Ionization of β-Naphthol and Boric Acid at Temperatures from 225 to 300 °C using UV-Visible Spectroscopy," *Journal of Solution Chemistry,* vol. 38, no. 7, pp. 805-826, 2009, doi: 10.1007/s10953-009-9411-6.

[71] R. E. Mesmer and C. F. Baes, "Phosphoric acid dissociation equilibria in aqueous solutions to 300°C," *Journal of solution chemistry,* vol. 3, no. 4, pp. 307-322, 1974.

[72] W. W. Rudolph, "Raman-Spectroscopic Measurements of the First Dissociation Constant of Aqueous Phosphoric Acid Solution from 5 to 301 °C," *Journal of Solution Chemistry,* vol. 41, no. 4, pp. 630-645, 2012, doi: 10.1007/s10953-012-9825-4.

[73] H. F. Holmes, J. M. Simonson, and R. E. Mesmer, "Aqueous solutions of the mono- and di-hydrogenphosphate salts of sodium and potassium at elevated temperatures. Isopiestic results," *The Journal of chemical thermodynamics,* vol. 32, no. 1, pp. 77-96, 2000, doi: 10.1006/jcht.1999.0571.

[74] R. L. Bassett, "A critical evaluation of the thermodynamic data for boron ions, ion pairs, complexes, and polyanions in aqueous solution at 298.15 K and 1 bar," *Geochimica et cosmochimica acta,* vol. 44, no. 8, pp. 1151-1160, 1980, doi: 10.1016/0016-7037(80)90069-1.

[75] J. P. Ferguson, H. Arcis, and P. R. Tremaine, "Thermodynamics of Polyborates under Hydrothermal Conditions: Formation Constants and Limiting Conductivities of Triborate and Diborate," *Journal of chemical and engineering data,* vol. 64, no. 10, pp. 4430-4443, 2019, doi: 10.1021/acs.jced.9b00496.

[76] J. P. Ferguson, H. Arcis, G. H. Zimmerman, and P. R. Tremaine, "Ion-Pair Formation Constants of Lithium Borate and Lithium Hydroxide under Pressurized Water Nuclear

Reactor Coolant Conditions," *Industrial & Engineering Chemistry Research,* vol. 56, no. 28, pp. 8121-8132, 2017, doi: 10.1021/acs.iecr.7b01015.

[77] *NIST-JANAF thermochemical tables*, 4th ed. ed. Washington, DC: American Chemical Society, 1998.

[78] H. Yu, Z. Jin, Q. Chen, and M. Hillert, "Thermodynamic Assessment of the Lithium-Borate System," *Journal of the American Ceramic Society,* vol. 83, no. 12, pp. 3082-3088, 2000, doi: 10.1111/j.1151-2916.2000.tb01686.x.

[79] A. Graff, E. Barrez, P. Baranek, M. Bachet, and P. Bénézeth, "Complexation of Nickel Ions by Boric Acid or (Poly)borates," *Journal of solution chemistry,* vol. 46, no. 1, pp. 25-43, 2016, doi: 10.1007/s10953-016-0555-x.

[80] P. R. Tremaine and J. C. Leblanc, "The solubility of nickel oxide and hydrolysis of Ni2+ in water to 573 K," *The Journal of chemical thermodynamics,* vol. 12, no. 6, pp. 521-538, 1980.

[81] F. H. Sweeton and C. F. Baes, "The solubility of magnetite and hydrolysis of ferrous ion in aqueous solutions at elevated temperatures," *The Journal of chemical thermodynamics,* vol. 2, no. 4, pp. 479-500, 1970.

[82] D. Shin, "Computational Thermodynamic Approach to Predict CRUD Formation," in "CASL," 2016.

[83] C. J. O'Brien, Z. Rák, and D. W. Brenner, "Free energies of (co, fe, ni, zn)fe 2 o 4 spinels and oxides in water at high temperatures and pressure from density functional theory: results for stoichiometric nio and nife 2 o 4 surfaces," *Journal of Physics: Condensed Matter,* vol. 25, no. 44, p. 445008, 2013.

[84] S. A. Attanasio, and David S. Morton, "Measurement of the Nickel/Nickel Oxide Transition in Ni-Cr-Fe Alloys and Updated Data and Correlations to Quantify the Effect of Aqueous Hydrogen on Primary Water SCC," presented at the 11th Int. Conf. Environmental Degradation of Materials in Nuclear Systems, Stevenson, WA, Aug. 10-14, 2003, 2003.

[85] M. Jin and M. Short, "Multiphysics modeling of two-phase film boiling within porous corrosion deposits," *Journal of computational physics,* vol. 316, pp. 504-518, 2016, doi: 10.1016/j.jcp.2016.03.013.

VITA

Jason Rizk grew up in Oak Ridge, Tennessee. After high school, he attended the University of Tennessee, Knoxville and received a Bachelor of Science in Nuclear Engineering and Mathematics, graduating summa cum laude. He then attended graduate school at the University of Tennessee, Knoxville, pursuing a Doctor of Philosophy degree in Nuclear Engineering. His research includes the thermochemistry and multi-physics modeling of the corrosion aspects of nuclear fuel. Soon, he will begin a postdoctoral position at Los Alamos National Laboratory where he will perform computational materials science research relating to nuclear fuel systems. He is grateful to his many mentors, his supportive friends, and his loving family.